Simulation of Void Nucleation in Single-Phase Copper Polycrystals

Submitted in partial fulfillment of the

requirements for the degree of

Doctor of Philosophy

in

Materials Science and Engineering

Evan Lieberman

B.S., Materials Science and Engineering, Georgia Institute of Technology
M.S., Materials Science and Engineering, Carnegie Mellon University

Carnegie Mellon University
Pittsburgh, PA

August 2016

Acknowledgements

First and foremost I want to thank my PhD advisor Prof. Anthony Rollett for all of his assistance and teachings. From him I learned how to be a scientist, how to apply my knowledge in new and constructive ways and how to compose myself within my chosen profession. I also want to thank the mentors I have had at Los Alamos National Laboratory, Dr. Ricardo Lebensohn and Dr. Edward Kober, for helping with their insight, guidance and knowledge. I owe a special thanks to Dr. Saryu Fensin of LANL, both for all she has taught me about material science and for all the advice she has given me as I pursue my career. From LANL I also want to thank Dr. Ellen Cerreta, Dr. John Bingert and Dr. Curt Bronkhorst, for without their past efforts my work could of never been accomplished and also for Dr. Bronkhorst's infinite patience in teaching the fundamental ideas behind his works. I also want to acknowledge Dr. Kober's significant contribution to my work by helping me create our grain boundary normal method and similarly to Prof. Marc DeGraef and Prof. Shlomo Ta'asan for helping me work out the finer points. I would also like to thank Prof. Robert Suter and his group, namely Dr. Chris Hefferan and David Menasche, for letting me use some of the data they generated in my work and for teaching me so much about their own works. For the members of my thesis committee, Prof. Gregory Rohrer, Prof. Elizabeth Holm and Dr. Ricardo Lebensohn, I can't thank you enough for all the discussion we have had about my work and how it could be improved upon.

I would never of reached this point without the knowledge and instruction I gained from the generosity of my upperclassmen. I must thank Dr. Benjamin Anglin and Dr. Sean Donegan for their patience in teaching my about various modeling and

programming knowhow and also a thanks to Dr. Stephanie Bojarski for helping me out with understanding Prof. Rohrer's work in grain boundaries. I also wouldn't of made it through my first summer at LANL without the help and friendship of Prof. Anand Kanjarla and Prof. Stephen Niezgoda who encouraged me on the significance of my work whose efforts eventually bore fruit with my comprehension of the mechanical model we were all using.

I would also like to show my gratitude to the students I entered, worked and studied at CMU with these many years. Special thanks to Dr. Brian Lin, Dr. William Frazier Jr. and Philip Goins for joining me in exploring the mysteries of computational material science. Addition thanks to Dr. Lily Nguyen, Dr. Clare Mahoney, Dr. Miaolei Yan, Dr. Vincent DeGeorge, Ellen Reifler, and Meredith Muskovich for all of us join together to make a ragtag bunch of graduate students into a community, along with the occasional scientific assistance.

To my family, without whom I'd have gotten nowhere and would of quickly gone insane under all the work, I give my everlasting thanks and love. Thanks and love to my mother, Cindy Kush, who always gave a ready ear and who kept me cheered for all these years; to my father, Robert Lieberman, who always encouraged my to follow my scientific ambitions; to my step-father, Thomas Kush, who always worked so hard to make sure I could focus on my studies. I would also like to show appreciation to my friends from undergraduate school, David Akhigbe Jr. and Anna Alexander, whose long distance friendship and support kept me happy even in the worst of times.

This work is supported by Los Alamos National Laboratory's Directed Research and Development (LDRD-DR Project 20140114DR) and the Joint DoD/DOE Munitions Technology Programs. Data was collected at the Advanced Photon Source (beamline 1-ID), supported by the US Department of Energy, Office of Science, Office of Basic Energy Sciences under contract number DE-AC02-06CH11357.

Abstract

A systematic investigation is presented into the microstructural and micromechanical influences on ductile damage nucleation with an emphasis on grain boundaries in polycrystals. Microstructures obtained from experiments on copper polycrystals are characterized using Electron Backscatter Diffraction (EBSD) and near-field High-Energy Diffraction Microscopy (nf-HEDM) and the occurrence of damage is compared with micromechanical values obtained using an elasto-viscoplastic model based on the Fast-Fourier Transform (EVPFFT). The model produces full-field solutions for the stress and strain in voxelized polycrystalline microstructures. In order to resolve the fields onto interfaces, local Cartesian moments of the polycrystalline grain structure are used to extract the normals of grain boundaries and the tangents of triple junctions directly from the voxelized microstructure. Thus projecting the stress yields a parameter with potential significance, i.e. the grain boundary surface tractions. We identify "traction hotspots", i.e. regions with tractions that are significantly above the mean, for the case of uniaxial tension. These show correlations with the angle between the grain boundary normal and the loading axis, a trend that some experiments also show when boundaries that nucleated voids are analyzed using EBSD, though differences present between the simulation and experiment hint that further criteria are needed. Nf-HEDM was used to record microstructure images of a polycrystalline sample before and after it undergoes damage. The damage locations in the post-shocked image are mapped onto the pre-shocked image, allowing stress and strain values from the EVPFFT model in the regions that eventually nucleated damage to be correlated with the locations of the void. The unexpected result was that differences in plastic work across boundaries correlated with voids, whereas

quantities such as triaxiality and normal forces across boundaries did not.

Table of Contents

List of Tables (by page number)

List of Figures (by page number)

List of Notations

$\mathbf{A}_{ij}$: Second rank tensor with indices *i* and *j*

$\dot{\mathbf{A}}$: Scalar or tensor differentiated with respect to time

$A_{ij,j}$: Tensor differentiated with respect to spatial index *j*

$\hat{\mathbf{A}}$: Scalar or tensor represented in Fourier space

$\boldsymbol{g}$: Orientation matrix for a single crystal/grain

$\boldsymbol{O}^{i}_{c}$: Rotation matrix for the *i*th crystal symmetry operator for crystal structure *c*

C_{ijkl} : Elastic stiffness tensor (fourth rank)

$\boldsymbol{m}^{\alpha}$: Schmid tensor for slip system α

σ_{ij} : Cauchy stress tensor

ε_{ij} : Strain tensor

$\dot{\gamma}^{\alpha}$: Shear rate on slip system α

τ^{α} : Critical resolved shear stress on slip system α

$\boldsymbol{G}$: Green's function operator

M_{opq}, μ_{opq} : Cartesian moment of order $o+p+q$

o p q : Indices representing the order of Cartesian moment

r : Position defined within Cartesian space as translated from discrete space

$f(\mathbf{r})$: Indicator function with respect to Cartesian point **r**

$w(\mathbf{r})$: Weighting function with respect to Cartesian point **r**

S : Limit of Cartesian space within which Cartesian moments are calculated

$\vec{T}$: Surface traction vector

$\vec{T}^{n}$: Normal component of traction vector

$\vec{T}^{s}$: Shear component of traction vector

σ_{VM} : von Mises equivalent stress

ε_{VM} : von Mises equivalent strain

σ_{Hyd} : Hydrostatic or mean stress

σ_{Triax} : Stress triaxiality, the ratio between hydrostatic and von Mises stress

M : Taylor factor

$\dot{W}^{P}$: Rate of plastic work

d_{H} : Hellinger distance

Chapter 1: Introduction

Predicting the conditions determining material failure is one of the most fundamental challenges in Materials Science. One important failure mechanism for ductile materials undergoing dynamic loading conditions is void nucleation, growth and coalescence[1, 2]. In the first stage, under appropriate driving forces, void nuclei reach a size large enough to become stable and eventually sustain growth. At this nucleation phase of damage the influence of the material's microstructure can be very strong. Growth occurs when the volume of stable voids increases driven by stress triaxiality[2], which reaches high values under the dynamic loading conditions considered in this work. Coalescence occurs when voids grow enough such that stress and strain concentrations in the surrounding material start overlapping and further increasing, promoting neighboring voids to join together[1]. It is at this stage in the process where ultimate failure of the material is initiated. The ability to predict how much a given microstructure is more or less vulnerable to damage nucleation and growth constitutes an important contribution to the emerging field of computational materials design that would enable the discovery and development of new processes and/or materials with higher resistance to damage.

The determination of whether or not voids will nucleate and grow in specific locations requires identifying what microstructural features are conducive or unfavorable to damage initiation. Damage nucleation is a local event so in order to make accurate predictions the microstructural features considered must be resolved to as close to the scale of the damage as possible. To do so, this work uses an elasto-viscoplastic Fast Fourier Transform-based (EVPFFT) model[3] to associate parameters calculated from the model with void nucleation in single-phase copper polycrystals. The more common way

of modeling the mechanical response of meso-scale materials is through Finite Element Methods (FEM)[4-7] but we use the EVPFFT model due to its faster runtime[8] and because it can be applied directly to microstructure images without any meshing beforehand.

The main focus of this work is on grain boundary surface traction, which is defined as the projection of the local Cauchy stress tensor onto the grain boundary surface and is equivalent to the load experienced on a grain boundary interface. Furthermore, the grain boundary surface traction can be separated into two components, a normal component of traction and a shear component of traction. These components represent tractions perpendicular and tangent to the grain boundary surface, respectively. The hypothesis is as follows: "Void nucleation in shock-loaded copper polycrystals is dependent on extreme values of grain boundary surface tractions." We investigate this by comparing trends in the boundary information, in particular the grain boundary plane in relation to the loading axis though other parameters are considered, between boundaries that experience extreme surface tractions in the model and boundaries on which voids nucleated in an experimental study on the shock-loading of copper polycrystals. What we show is that, while the kinds of grain boundaries that experience the extreme values of surface tractions have qualitative correlations the with kinds of boundaries that actually void in experiments, there are enough differences to suggest that further parameters are needed to predict void nucleation. To validate these qualitative correlations and explore the influence of other parameters, we perform a direct comparison between simulation results and experimentally measured voids using new data acquired from near-field High-Energy Diffraction Microscopy (nf-HEDM), which can measure three-dimensional data

non-destructively. The comparison reveals that surface tractions do not correlate with where voids occur but instead that parameters describing the contrasts in plasticity across the grain boundary do correlate. These results are presented in Lieberman *et al*[9].

In order to properly characterize the mechanical responses of metals, plastic deformation of the metal must be considered. Plastic deformation in metals occurs primarily through the movement of dislocations, which are defects in the crystal lattice, through said lattice. This movement is dictated by slip systems, which are particular combinations of slip plane and slip direction (i.e. Burgers vector) in the crystal structure that offer the easiest (i.e. least work done) route[10]. Copper has a Face-Centered Cubic (FCC) crystal structure and the slip systems are well understood for this structure. However, to complicate matters, most metals we would consider for these analyses are polycrystalline in nature; thus they have many grains each with a particular orientation, as well as differing neighbor grains, that lead to heterogeneous distributions of mechanical responses throughout the material. To understand the origin of failure, which is a highly local event, the internal response of a material must be studied[11, 12]. In this work we use the EVPFFT model to quantify this internal response in voxelized microstructure images, in particular to calculate the local Cauchy stress tensors in the vicinity of grain boundaries so that the grain boundary surface tractions can be calculated.

The various backgrounds on void nucleation, crystallography, near-field High-Energy Diffraction Microscopy and shock loading are covered in Chapter 2. A description of the history and derivations of the EVPFFT model is covered in Chapter 3. To calculate the grain boundary surface tractions, we need not only the stress tensor but also the grain boundary surface normal. Because the EVPFFT model works on voxelized images, a

special algorithm, developed by Lieberman *et al.*[13], was used to calculate the surface normals directly and it is covered in Chapter 4. In Chapter 5, based on the ability to calculate the surface tractions, we next analyze the microstructural effects that relate the surface traction hot spots and compare the results to experiments to identify correlations with grain boundary damage. In Chapter 6 we perform a comparison between the EVPFFT simulation results and grain boundary voids generated by a shock loading experiment and imaged using nf-HEDM. The conclusions from this work as well as suggestions for future work are discussed in Chapter 7.

Chapter 2: Background

2.1: Background on Voids

There are two primary reasons why understanding void formation and growth is important[14]. The end result of voids growing and coalescing to failure of the material through accumulative damage but also as the amount and size of voids increase in the material is that the load-carrying capacity is decreased. This modifies the macroscopic stress-strain behavior, which, for example, is known as the tertiary stage of creep. Voids are known to play a role in the failure of a wide variety of materials, ranging from many polymers[15] to various types of metals such as steel[16, 17] and copper[18]. Void nucleation can occur through a number of different mechanisms depending on both the nature of the materials microstructure (i.e. presence of secondary phases, texturing of the polycrystal) and the nature of the imposed conditions (i.e. loading type and rate, temperature). One such example is that under high temperature creep conditions, the primary mechanism by which voids nucleate and growth is diffusion of vacancies to grain boundaries[19, 20] as well as the effects of grain boundary sliding[20-22], which also cause movement of vacancies and dislocations at the interface. Another extensively studied example, which is investigated here, is the nucleation of voids at grain boundaries caused by shock loading of the material[23-28]. An example of voids nucleated at grain boundaries induced by shock loading is shown in Fig. 2-1.

There are many different material characteristics that one could to investigate for a microstructural influence on void nucleation in polycrystals, so we review the available literature to provide a starting point. There are many cases of experiments that show that

the interfaces in a material have a significant connection to the nucleation of damage. Damage around inclusions in ductile materials[29] are a good example.

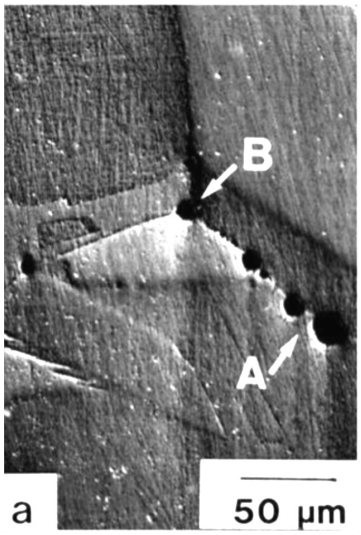

Figure 2-1. Example of voids nucleated at grain boundary and triple point due to shock loading; taken from Christy *et al.*[27]

Such particulates can lead to damage in two different ways, which are particle cracking and interface fracture/decohesion as shown in Fig. 2-2. Note that even in a simple explanatory diagram of these effects, the morphology of the two voids depends on the alignment of the particles with the stress system.

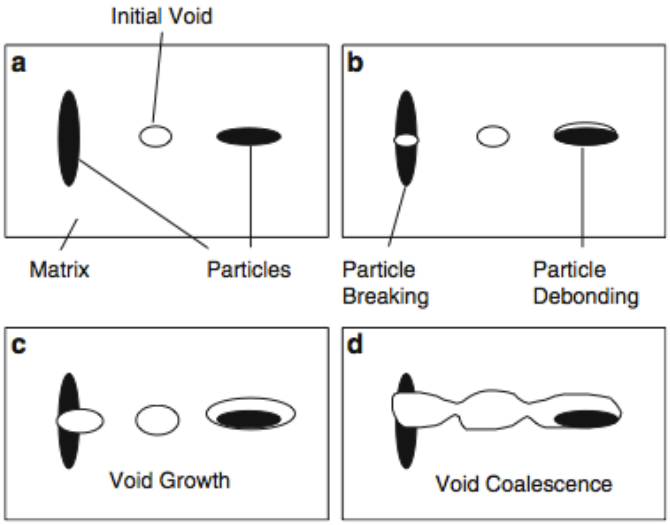

Figure 2-2. Void evolution in material with particulates; (a) initial state, (b) void nucleation, (c) void growth, (d) void coalescence; taken from Chen *et al.*[29]

Gurland[17] showed that for the case of uniaxial loading of spheroidized 1.05% C steel, a common characteristic of the cementite particles that cracked was that their longest axis was parallel to the loading direction, confirming the relevance of the shape shown on the left in Fig. 2-2. Another interesting feature observed in Gurland's work is the angle of the cracks in the sample relative to the different loading directions but this will be covered in more detail in Section 5. Beremin[30] studied ductile fracture of A508 Steel at elongated MnS inclusions. The results of this work showed that any particle fractures only occurred when the loading direction was aligned with the long direction of the inclusion but when the load was along the transverse it was interface decohesion that was most common. Both these experiments show that the relationship between loading conditions and interface inclination plays a role in damage nucleation. With respect to void nucleation in the absence of particulates, however, cracking is eliminated as a void nucleation mechanism since that is specifically related to the failure of brittle particulates and we must seek other mechanisms.

When voids nucleate in the absence of particulates, the primary location is at grain boundaries. Work by Hull and Rimmer[31] shows a morphological significance for grain boundary damage, more specifically that grain boundaries transverse (perpendicular) to the loading direction fail more frequently, which relates to tension across the boundary. Works by Field *et al*.[32], Diard *et al*.[33], Fensin *et al*.[34], and Yang *et al*.[35] utilized multiple two-dimensional micrographs of damaged materials to show that damage preferentially occurs on interfaces with specific relationships to the principal loading directions. The nature of the relationship depends, however, on the type of loading (e.g.

fatigue versus shock). The relative plastic response of the crystals surrounding voids is another feature that has been associated with damage initiation by Wright *et al*.[36], Bieler *et al*.[37, 38], Semiatin *et al*.[39], Escobedo *et al*.[25, 26] and Yang *et al*.[35], although this response was linked to several different parameters such as Schmid factor, Taylor factor, and qualitative hardness; also the number of void sites studied was limited. Work has also been done on the relationship between Σ3 boundaries, which are associated with twinning in many metals, and damage initiation. Escobedo *et al.*[25], Fensin *et al.*[40, 41] and Yang *et al.*[35] have shown that the Σ3 boundary tends to be resistant to void formation under shock loading conditions. In contrast, works by Boettner[42] and Knorr[43] have shown that Σ3 boundaries tend to be the most vulnerable to crack initiation and growth under fatigue loading conditions. The latter, however, appears to be linked to the tendency for slip to accumulate on slip systems that run parallel to the twin boundary[44].

2.2: Crystal Orientation and Heterogeneity

Polycrystalline materials such as those that are considered in this work are known for their anisotropic and heterogeneous behavior. Such behavior is due to the many different crystal orientations. To characterize such materials, it is important to understand how these crystal orientations are differentiated, how they relate to each other and how they affect the micromechanical behavior of the material. A single crystal orientation is quantified using three independent values that describe the rotation between two physical frames of reference, the crystal reference frame and the sample reference frame[45]. These three values are commonly represented by Euler angles, which are angles that describe three rotations about three axes that bring the sample frame coordinate system into coincidence with the crystal frame coordinate system. All crystal orientation information

in this work is described using the Bunge convention of Euler angles. In this convention, the first angle (ϕ_1) is a rotation about the sample *Z*-axis, the second angle (Φ) is a rotation about the new *X*-axis generated by the first rotation and the third angle (ϕ_2) is a rotation about the new *Z*-axis generated by the second rotation. While Euler angles are a useful and concise descriptor of crystal orientations, it is often convenient to convert the information into other forms more suitable for mathematical manipulation. The most common form Euler angles are converted to is that of the orientation matrix and the conversion equation for Bunge Euler angles is described by:

$$g = \begin{bmatrix} \cos\phi_1 \cos\phi_2 - \sin\phi_1 \sin\phi_2 \cos\Phi & \sin\phi_1 \cos\phi_2 + \cos\phi_1 \sin\phi_2 \cos\Phi & \sin\phi_2 \sin\Phi \\ -\cos\phi_1 \sin\phi_2 - \sin\phi_1 \cos\phi_2 \cos\Phi & -\sin\phi_1 \sin\phi_2 + \cos\phi_1 \cos\phi_2 \cos\Phi & \cos\phi_2 \sin\Phi \\ \sin\phi_1 \sin\Phi & -\cos\phi_1 \sin\Phi & \cos\Phi \end{bmatrix} \tag{2.1}$$

One use for the orientation matrix is in determining the misorientation between two grains and is defined as the rotation to bring one grain's crystal coordinate system into coincidence with another grain. Simple misorientation between two crystals is calculated by applying a rotation from one crystal to the sample reference frame followed by a rotation from that sample reference frame to the other crystal, which is represented by the orientation of matrix from one grain being multiplied by the inverse of the other grains orientation matrix. However, the presence crystal symmetry means that there are many equivalent misorientations that can be determined between two crystals. To choose amongst these equivalent rotations, the pair of crystal symmetry operators is chosen that, when applied to each crystal, produces the smallest misorientation angle. The misorientation and subsequent angle are calculated as follows:

$$\begin{aligned} \Delta g^{ij} &= O_c^i g_a (O_c^j g_b)^{-1} \\ \theta_{mis} &= \min_{\forall i,j} arccos\left(0.5[\Delta g_{11}^{ij} + \Delta g_{22}^{ij} + \Delta g_{33}^{ij} - 1]\right) \end{aligned} \tag{2.2}$$

The orientation matrices for the two grains are represented by g_a and g_b while the symmetry operators applied to both crystals are represented by O_c^i and O_c^j. For the cubic crystal structure of copper there are 24 unique symmetry operators for the proper rotations.

Crystal orientation and symmetry also has a significant effect on the elastic and plastic micromechanical properties of polycrystals. Crystal symmetry influences the anisotropy of each individual crystal while the differences in crystal orientation within a sample lead to heterogeneity of mechanical responses. The elastic properties of a material are represented by the stiffness tensor, which relative to the crystal reference frame takes the following form in cubic crystals[10]:

$$\boldsymbol{C} = \begin{bmatrix} C_{11} & C_{12} & C_{12} & 0.0 & 0.0 & 0.0 \\ C_{12} & C_{11} & C_{12} & 0.0 & 0.0 & 0.0 \\ C_{12} & C_{12} & C_{11} & 0.0 & 0.0 & 0.0 \\ 0.0 & 0.0 & 0.0 & C_{44} & 0.0 & 0.0 \\ 0.0 & 0.0 & 0.0 & 0.0 & C_{44} & 0.0 \\ 0.0 & 0.0 & 0.0 & 0.0 & 0.0 & C_{44} \end{bmatrix} \tag{2.3}$$

This form is known as the Voigt representation of the stiffness tensor, which may also be represented by a 4th rank tensor. The reduction of this matrix to 3 independent variables from 36 results from the application of crystal symmetry operators. The plastic properties of a material are controlled by much more complicated processes but relate to crystal orientation through the symmetric Schmid tensors[10], of which there are one of each for each slip system in a given crystal structure and are calculated by

$$m_{ij}^{\alpha} = \frac{1}{2}(s^{\alpha} \otimes n^{\alpha} + n^{\alpha} \otimes s^{\alpha}) \tag{2.4}$$

where *s* and *n* are the slip direction and slip plane normal for slip system α, both of which are represented in the crystal reference frame.

However, stress and strain fields are represented in the sample reference frame and thus the elastic and plastic tensors must be (axis-)transformed in order for calculations involving them to be performed. The transformation (*a.k.a.* passive rotation) utilizes the inverse of the orientation matrix, to pass from crystal to sample frame, as follows:

$$m'_{ij} = a_{ik}a_{jl}m_{kl}$$
$$C'_{ijkl} = a_{im}a_{jn}a_{kp}a_{lq}C_{mnpq} \tag{2.5}$$

where *a* is the inverse of the orientation matrix. Thus the heterogeneity of the crystal orientations within a polycrystalline structure is translated to heterogeneity in the micromechanical responses.

2.3: Near-field High-Energy Diffraction Microscopy

A way of measuring three-dimensional microstructures is necessary to perform a proper comparison between experimental and simulated meso-scale data. The most common method of obtaining three-dimensional orientation maps is through the use of electron backscatter diffraction surface measurements combined with serial sectioning of the sample so that multiple surface measurements can be made through the thickness of the sample and then stacked to create a three-dimensional image[46, 47]. However, this method is destructive to the sample because it requires material to be removed to prepare a polished surface for measurement. Therefore it cannot be used to compare volumes of the same sample at multiple states. Thus for this work we use a technique developed by Suter *et al*.[48, 49] called near-field High-Energy Diffraction Microscopy (nf-HEDM), which can measure three-dimensional crystallographic orientation maps non-destructively. This technique has been used to study a variety of phenomena, from micromechanical trends in polycrystals[50, 51] to the evolution of grain boundaries during

annealing[52]. Within this work, aside from using data collected via this technique to perform direct comparisons between simulation and experiments, we also use the three-dimensional nature of the data to validate new techniques in the analysis of grain boundaries.

Nf-HEDM relies on the measurement and analysis of high-energy synchrotron X-rays that are diffracted through the sample. The data presented in this work were collected at Advanced Photon Source (APS) beam line 1-ID-B at Argonne National Laboratory. The X-ray beam is tailored to reach the sample as a monochromatic planar beam that is about 1.2 mm wide and thus encompasses the full width of a 1 mm wide sample. The vertical position of the sample means that the illuminated layer is effectively a cross-section of the material. The energy of the beam must be sufficient to penetrate the sample and have measurable intensity on the detector. For copper, a beam energy of ~64 keV is sufficient and commonly used. While the beam is referred to as planar, it does have a finite thickness associated with it, which is about 2 μm. However, both to avoid overlapping scans of the same region as well as for time efficiency, the sections scanned along the height of the sample are 2 to 4 μm apart. A drawback to this beam height and section spacing is that the resolution in this direction is limited compared to other techniques such as focused ion beam instruments with EBSD[46, 47] and it has resulted in difficulties with performing in depth analyses of grain boundary characteristics[53-55]. These planar X-rays scatter by interacting with the atoms composing the crystal structure of the sample, thus diffracting at angles dictated by Bragg's Law. Of order 100 diffraction peaks are collected and indexed for each location in a given section measurement in the sample, which provides high accuracy of order 0.1° in the orientation determination. The sample

is rotated around an axis perpendicular to the beam plane in at most 1° intervals up to a total of 180° and at each angle, the detector screen is placed at two different offsets from the sample along the beam direction. The translation of the detector screen, which ranges from 5 to 15 mm from the sample, allows for the path of each diffracted beam to be traced back to its spatial location within the sample. The spatial tracking of the diffraction peaks leads to an in-plane pixel resolution that is of order 1.5 to 5 microns. Both the rotation of the sample and the use of two detector distances are necessary for determining the spatial point-of-origin of the diffraction peaks as well as the crystal orientation at that point. The rotation generates multiple signals from a given point-of-origin by inducing diffraction from multiple crystallographic planes as the crystal is rotate. The two detector distances are needed to generate uniquely identifiable diffraction peaks from a single point-of-origin. Fig. 2-3 demonstrates the necessity of multiple detector distances. Multiple points-of-origin could generate diffraction peaks at the same spot on a single detector, but as the distance is changed this intersection would not be maintained. Once these processes are complete for a single section, the sample is translated along the rotation axis so that the process can be repeated on another section of the sample. The resulting data is then processed to remove background and random scattering signals so that the diffraction signals from the sample can be focused on and orientation reconstruction can begin.

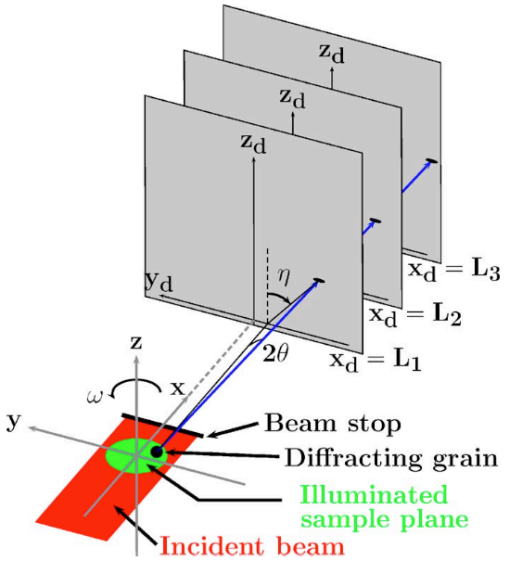

Figure 2-3. Image of the planar radiation beam diffraction from the sample onto the detector set at multiple distances[48].

To perform the reconstruction of the crystal orientations from the diffracted signal information, the experimental parameters such as the distance between the sample and detector have to be established. These parameters are found using a calibration sample that has as few grains as possible. For each set of parameters the orientations are reconstructed, hence fewer orientations is preferred, and the set that produces the greatest confidence is selected via a Monte Carlo optimization of the parameters. Each illuminated section is represented as triangular elements on a regular grid within the scanned section; they are effectively voxels because each section represents a slice through the volume of the sample. Orientation reconstruction is achieved by performing a forward modeling method on the diffraction signal data at each voxel. The forward modeling method works by simulating the diffraction response for every orientation that is unique with respect to crystal symmetry. A requirement to do this is that experimental parameters must be calculated by optimizing them for a sample with known results

before working with the intended sample. The measured diffraction peaks are compared to the set of simulated ones for each orientation and the ratio between the number of matched peaks and the total number of usable peaks for that orientation is used as a measure of the confidence of the result. A diffraction peak, whether measured or simulated, is considered usable if it appears at multiple detector distances. The measured and simulated peaks observed over all the rotations and detector distances, are matched based on their location on the detector. The peaks are treated as binary in nature, either present or not; the intensities of the peaks are not currently used as part of the confidence measurement. The orientation that has the highest confidence is assigned to the particular voxel and this process is repeated at each voxel. The forward modeling method can be done independently for each voxel for best accuracy or can utilize nearest neighbor information to accelerate the registration process. The orientation resolution from the forward modeling method output is 0.1° or lower depending on the exact method used. Once the forward modeling method is complete for each section, these layers are stacked together to make a three-dimensional orientation map of the sample[49].

2.4: Shock Loading and Spallation

Gas-driven plate impact experiments are one of many kinds of shock loading conditions. A gas-driven gun launches a plate at a sample such that the surfaces of the impact plate and sample are parallel. To ensure that the impact plate does not warp from the force of the launch, a polymer foam block with high compressive stiffness but very low density is attached to the back face of the plate. This experiment is used to produce a planar shock wave in a material under conditions in which the impact plate velocity and angle are more controlled as compared to explosive-driven shock experiments. By

applying a shock wave to a polycrystalline metal, elasto-plastic near-uniaxial strain occurs at high rates[56]. A material undergoing shock loading experiences varying strain rates over the duration of the wave propagation. The highest strain rate occurs on the arrival of the initial compressive wave and is usually in the range of 10^6 per second but can go up to 10^9 per second depending on the loading conditions. It is at this range of strain rates that the effects of micro-inertia within the material begin to have significant effects. The nature of the uniaxial strain, which is a combination of deformation in a single direction while the lateral directions do not deform and causes the hydrostatic stress to reach very high levels. However, the deformation is not purely hydrostatic; deviatoric stress and strains are generated that result in plastic deformation and, at high enough shock levels, defect generation within the material[56]. The heterogeneity of a polycrystalline material, via elastic and plastic anisotropy, results in significant local variance in the levels of deviatoric stress. The high hydrostatic stress combined with the still present but smaller deviatoric stress results in very high stress triaxiality under this loading condition.

When the hydrostatic stress is sufficiently large then the wave may be approximated as passing through the material as it would a fluid. This approximation is the basis for the equations developed by Rankine and Hugoniot to describe the behavior of shock waves in a material[56, 57]. Additional assumptions of this approximation are that the wave propagation is one-dimensional and that the wave front is perfectly sharp such that it represents a discontinuity in pressure, density and temperature. These equations can further be applied to the case of impact between two materials where one is at rest (i.e. the sample) and the other has a set velocity (i.e. the impact plate). When this situation

occurs, compressive waves are generated heading out from the impact plane in both the plate and the sample. These waves generate the same initial pressure but have different velocities depending on the equations of state for the two materials. All these parameters can be generated from the impact velocity if the equations of state are known. For copper, of course, well-established equations of state are available. If the impact plate and the sample are of the same material, then the impact velocity is split evenly between the waves in the impact plate and sample.

Damage events in shock loading conditions take the form of void nucleation, growth and coalescence to the point at which the sample separates perpendicular to the shock direction at which point spallation[57] has occurred. Spallation occurs at a specific "plane" within the material that is dictated by the shock properties and geometry of the sample and impact plate, though in practice damage occurs over a range of the thickness around the "plane". The compressive waves generated at the impact plane propagate outward towards the far sides of the sample and impact plate. When the waves reach these free surfaces (or if a polymer foam is present behind the impact plate, its density is so low that it is approximate to a free surface), a release wave is reflected back towards the impact plane. The release, or rarefaction, waves are tensile in nature and work to unload the compression induced by the initial shock wave. When the release waves from the free surfaces reach each other, they have released the compressive state of the material and thus create a net tensile effect. It is this tensile pulse that causes spallation of the material and the plane where this tensile pulse is generated is known as the spallation plane. When the tensile pulse is great enough to initiate damage but is not sufficient to develop

coalescence and separation of the sample it is called “incipient” spallation, a state that is useful for analyzing damage nucleation events[57].

The location of the spallation “plane” can be closely approximated before performing the experiment by controlling the thickness of the impact plate and sample in the shock direction[56, 57]. If the impact plate and sample are of the same material and the thickness of the impact plate is half that of the sample then the tensile peak will be generated halfway through the thickness of the sample. If the impact plate and sample are different materials then the spallation “plane” may still be estimated by calculating the approximate shock wave velocities in each material to determine where the release waves will intersect for given impact plate and sample thicknesses. Plots of the shock wave front positions vs. time are used to illustrate how this planning is done. The velocities of the shock waves are known through the equations of state for the materials of the impact plate and sample. Thus this plot can be generated by using the velocity to find the position of the wave front at a given time relative to the impact plane while also taking into account the geometry of the experimental setup as shown in Fig. 2-4 for a case where the sample and impact plate are the same material. If the materials are different, the interaction of the wave with the impact surface must also be taken into account.

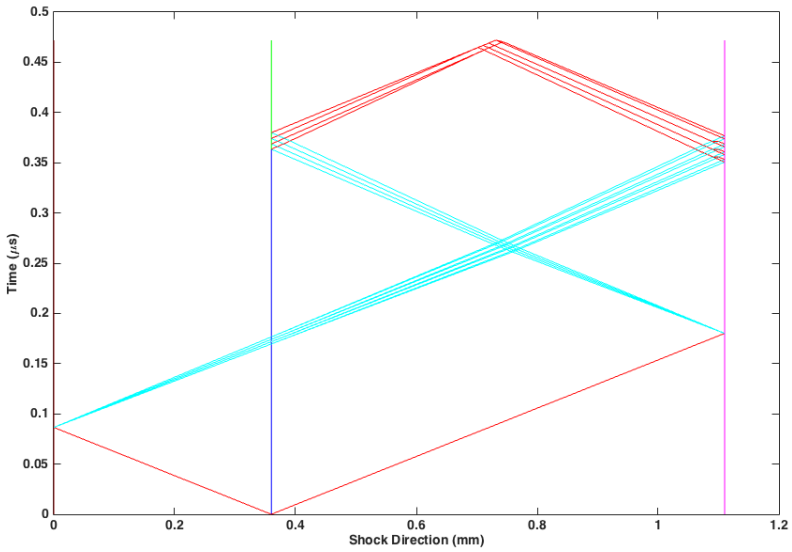

Figure 2-4. Plot of shockwave front position over time for Cu-Cu experiment. At time 0 the impact generates compressive waves that move outward toward the free surfaces (red). Rarefaction waves (light blue) reflect off of those surfaces and intersect in the sample to produce a tensile pulse and possibly cause void nucleation.

Within Fig. 2-4 the position axis begins at the free surface of the impact plate, with the vertical blue line (at 0.36 mm) representing the impact surface and the vertical purple line (at 1.085 mm) representing the free surface of the sample. The red lines represent compressive waves while the light blue lines represent release waves, which intersect to produce the tensile pulse near the midpoint of the sample as predicted. From this we see that the tensile pulse and initial spall will all occur within half of a microsecond of impact for these sample sizes and impact velocity. For this setup the predicted strain rate will also be on the order of 10^5 per second as determined by the known equations of state for copper. Also of note is that Fig. 2-4 shows a representation of the rarefaction fan. In actual experiments, a fan of release waves is generated when a compressive wave hits a free surface due to the heterogeneity of the material and the surfaces. These fans interact

to produce a tensile pulse that is a distribution in space and as well as time around the tensile peak; this will be shown in more detail in Chapter 6.

The description of plate impact behavior assumes that the shock wave is one-dimensional but in actual experiments this is not truly the case due to the impact plate and sample having finite sizes perpendicular to the shock direction and these sizes possibly not matching. To prevent radial release waves from influencing the mechanical state of the sample, the sample is encased in rings of material with similar shock impedances referred to as momentum trap rings. The purpose of these rings is that any radial waves generated by the impact spend the duration of the shock wave propagating through the rings and thus do not reach the sample itself until after the shock wave has reached its full effect, allowing for a recovered sample to only show the effects of the shock wave[58]. The diameter of these rings is determined based on the diameter and thickness of the sample, i.e. the diameter of the rings must be sufficiently large to keep the radial waves in them for the time it takes for the shock wave interactions to propagate through the sample thickness.

Chapter 3: Elasto-Viscoplastic Fast Fourier Transform Formalism

In this work we use an elasto-viscoplastic model that utilizes Fast Fourier Transforms (FFT) to solve for the local results of stress and strain within the volume being simulated. This kind of 'full-field' modeling is most commonly run with a Finite Element Method (FEM) formalism. One such example is in this case by Bronkhorst *et al*[6], who used a FEM model to analyze the local deformation behavior of tantalum. The reason that we do not use the FEM formalism is to avoid potential difficulties with meshing large and complicated structures. The issue of meshing is completely avoided with the FFT formalism because it operates directly on an image. Images of microstructure data obtained from a variety of means (i.e. EBSD, nf-HEDM, etc.) can be input directly into the model. An added benefit is that the FFT model is that it has been shown to be at least an order of magnitude faster than commercial FEM codes on microstructures of similar resolution[8, 59], especially when using crystal plasticity as the material model.

The FFT formalism began with the works of Suquet and Moulinec[60], who developed the model to solve for the local linear elastic mechanical responses of a heterogeneous material, in particular a two material composite. To begin, they establish what is known as a 'Fourier Grid' for their microstructure information, which represents a regularly spaced sampling of the materials properties on a regular grid of points in two or three dimensions. At each of these points a constitutive equation that relates stress and strain is solved. The local responses of the heterogeneous medium are found using Green's function method; the key result of this path is that the resulting Green's equation solution is a convolution integral which would be time consuming to solve numerically. A convolution integral in real space is, however, a point-wise product in Fourier space, thus Fourier transforms are used to speed up the algorithm. The Green's function method is

used with periodic boundary conditions and iteratively solves for stress equilibrium while maintaining strain compatibility conditions. In particular, a mathematical path developed by Mura[61] is used to solve for the Green's operator in Fourier space.

However, the model in that original form had a particular weakness: the number of iterations until convergence scaled linearly with the ratio between the Young's moduli of the two phases. Thus convergence is not guaranteed in some cases where the ratio is infinite such as where one part is a void or a rigid inclusion and more complex systems are difficult to run. To circumvent this limitation, Michel *et al*[62] developed an augmented Lagrangian method for the iteration scheme, where the key difference is that it adjusts both the stress and strain fields in each iteration. With this procedure, material structures that have high contrast in properties through the volume can be completed in more reasonable times. The next step in this method came when Lebensohn[63, 64] adapted this formalism to be run on polycrystalline structures for the cases of pure elasticity and pure viscoplasticity, connecting to the original concept by considering individual grains to be separate components of a composite whose effective modulus is compute from the average plastic response. Later an elasto-viscoplastic model was developed using infinitesimal strain theory to capture the elastic to plastic transition[3].

The elasto-viscoplastic FFT model uses a combined elastic and viscoplastic constitutive equation that incorporates Hooke's Law and an Euler implicit time discretization as shown by

$$\boldsymbol{\varepsilon}^{total}(x) = \boldsymbol{\varepsilon}^{e}(x) + \boldsymbol{\varepsilon}^{p}(x) = \boldsymbol{C}^{-1}(x) : \boldsymbol{\sigma}(x) + \boldsymbol{\varepsilon}^{p,t}(x) + \dot{\boldsymbol{\varepsilon}}^{p}(x, \boldsymbol{\sigma})\Delta t \qquad (3.1)$$

where $\boldsymbol{\varepsilon}^{\text{total}}$ is the total strain tensor split into the elastic strain tensor $\boldsymbol{\varepsilon}^{\text{e}}$ and the plastic strain tensor $\boldsymbol{\varepsilon}^{\text{p}}$, $\mathbf{C}^{-1}$ is the compliance tensor, $\boldsymbol{\sigma}$ is the full Cauchy stress tensor, $\boldsymbol{\varepsilon}^{\text{p,t}}$ is the

total plastic strain tensor up to time t and $\dot{\boldsymbol{\varepsilon}}^p$ is the plastic strain rate tensor. The last is defined by the viscoplastic constitutive equation

$$\dot{\boldsymbol{\varepsilon}}^p(x) = \sum_{\alpha=1}^{N_\alpha} \boldsymbol{m}^\alpha(x)\dot{\gamma}^\alpha(x)$$
$$\dot{\boldsymbol{\varepsilon}}^p(x) = \dot{\gamma}_o \sum_{\alpha=1}^{N_\alpha} \boldsymbol{m}^\alpha(x) \left(\frac{|\boldsymbol{m}^\alpha(x) : \boldsymbol{\sigma'}(x)|}{\tau^\alpha(x)} \right)^n \times sgn(\boldsymbol{m}^\alpha(x) : \boldsymbol{\sigma'}(x)) \qquad (3.2)$$

where $\dot{\gamma}_o$ is a reference shear rate, N_α is the total number of slip systems, $\mathbf{m}^\alpha$ is the symmetrized sample-frame Schmid tensor for slip system α, **σ'** is the deviatoric stress tensor, τ^α is the critical resolved shear stress for slip system α, and n is the rate sensitive exponent. This equation is solved at each grid point by adjusting the stress state until the sum of the strain rates become equal to that required to satisfy the global system. As indicated by the presence of the Δt component in (3.1), this model operates off of incremental applications of boundary conditions with subsequent incremental calculations of local response, which conforms to infinitesimal strain theory.

The model works by solving for local responses to a macroscopically applied condition. One begins by expressing inhomogeneous local values as a deviation from the response of a homogeneous reference material as shown by

$$\sigma_{ij}(x) = C^o_{ijkl} u_{k,l}(x) + \phi_{ij}(x)$$
$$\phi_{ij}(x) = \sigma_{ij}(x) - C^o_{ijkl} u_{k,l} \qquad (3.3)$$

where $\mathbf{C}^0$ is the stiffness tensor of the homogeneous reference material (in this works' case just the volume average of the local stiffness tensors), ϕ_{ij} is the polarization field, which describes the local deviation from the average stress, and $u_{k,l}$ is the displacement gradient tensor, from which the strain tensor is calculated from infinitesimal strain theory as:

$$\varepsilon_{kl}(x) = (u_{k,l}(x) - u_{l,k}(x))/2 \tag{3.4}$$

The condition of stress equilibrium is maintained in this model in the form of $\sigma_{ij,j}(x)=0$ and when that condition is applied to the second line of (3.3) then the result is

$$\phi_{ij,j}(x) + C^o_{ijkl} u_{k,lj} = 0 \tag{3.5}$$

which is an inhomogeneous differential equation that can be solved using Green's function method for a periodic volume with an applied global strain $E_{ij} = \langle \varepsilon_{ij}(x) \rangle$. The result is the following auxiliary problem given by

$$C^o_{ijkl} G_{km,lj}(x - x') + \delta_{im}\delta(x - x') = 0 \tag{3.6}$$

where $G_{km}(x)$ is the Green's function operator associated with the displacement field $u_k(x)$, δ is either the unit impulse function associated with the polarization field ϕ_{ij} or the Dirac delta function. According to the Green's function method, the solution to the auxiliary problem in (3.6) is given by the convolution integral

$$u_{k,l}(x) = \int_{R^3} G_{ki,jl}(x - x')\phi_{ij}(x')dx' \tag{3.7}$$

In Fourier space the convolution integral becomes just a product of the transformed functions, resulting in

$$\varepsilon_{ij}(x) = E_{ij} + FT^{-1}[\mathrm{sym}(\hat{\Gamma}^o_{ijkl}(k))\hat{\phi}_{kl}(k)] \tag{3.8}$$

where k is a point in frequency space, $\hat{\boldsymbol{\Gamma}}^0$ is the Green's operator in Fourier space and ^ indicates the Fourier transformed version of the variable. The Green's operator in Fourier space is given by

$$\hat{\Gamma}^o_{ijkl}(k) = -k_j k_l \hat{G}_{ik}(k) \tag{3.9}$$

where $\widehat{G}_{ik}(k)$ is solved using a method from Mura[61] where there is a relationship between $\widehat{\mathbf{G}}(k)$ and an acoustic tensor **A'** defined as

$$\hat{G}_{ik} = [A'_{ik}]^{-1} = [k_l k_j C^o_{ijkl}]^{-1} \tag{3.10}$$

where $\mathbf{C}^0$ is the homogeneous reference material stiffness tensor. This holds true except in the case of the origin point in Fourier space; in this special case the value of $\hat{\mathbf{\Gamma}}^0$ is set to be just the inverse of $\mathbf{C}^0$.

So at this point we have a way to resolve the local strain tensors based on some applied global strain and a guess for the local stress states. The next step is to iterate this process to connect the local stress states to the local strain states using the constitutive equations and the augmented Lagrangian method. For the elasto-viscoplastic formalism, a modified form of (3.8) is used as shown

$$e^{(i+1)}_{ij}(x) = \mathrm{E}_{ij} + FT^{-1}[\hat{\hat{e}}^{(i)}_{ij} + \mathrm{sym}(\hat{\Gamma}^o_{ijkl}(k))\hat{\lambda}^{(i)}_{kl}(k)] \tag{3.11}$$

where $\boldsymbol{\lambda}^{\mathbf{i}}(\mathrm{x})$ is the guess for the local stress tensor at step i, $\tilde{\boldsymbol{e}}^{\boldsymbol{i}}(\mathrm{x})$ is the fluctuation of the local strain tensor from the global average at step i and $\mathbf{e}^{\mathrm{i+1}}$ is the total local strain tensor at step i +1. Note that from here on strain as the symbol **e** refers to strain derived from the Green's function method while **ε** will refer to strain derived from the constitutive equations (3.1 and 3.2). The augmented Lagrangian method seeks the nullification of a residual term at each material point in the volume. For this section, contracted Voigt notation for symmetric tensors is used; for example the stress goes from σ_{ij} to σ_k and stiffness goes from C_{ijkl} to C_{kl} where $k,l \in 1{:}6$. The resulting residual equation now appears as

$$R_k(\boldsymbol{\sigma}^{(i+1)}) = \sigma^{(i+1)}_k + C^o_{kl}\varepsilon^{(i+1)}_l(\boldsymbol{\sigma}^{(i+1)}) - \lambda^{(i)}_k - C^o_{kl}e^{(i+1)}_l = 0 \tag{3.12}$$

where R_k is the residual and **ε** is calculated from **σ** and the initial **σ** is guessed to be the same as **λ**. For each subsequent iteration, the new **σ** is calculated from (3.12) using a Newton-Raphson (NR) solution scheme as shown

$$\sigma_k^{(i+1,j+1)} = \sigma_k^{(i+1,j)} - \left(\frac{\delta R_k}{\delta \sigma_l} \bigg|_{\sigma_k^{(i+1,j)}} \right)^{-1} R_l(\boldsymbol{\sigma}^{(i+1,j)}) \tag{3.13}$$

where the index *j* tracks the NR iteration. The Jacobian in (3.13) is calculated from (3.12), taking into account the constitutive equation (1), shown as

$$\frac{\delta R_k}{\delta \sigma_l} \bigg|_{\sigma_k^{(i+1,j)}} = \delta_{kl} + C_{kq}^o C_{ql}^{-1} + \Delta t \; C_{kq}^o \frac{\dot{\epsilon}_q^p}{\sigma_l} \bigg|_{\sigma_k^{(i+1,j)}} \tag{3.14}$$

where δ_{kl} is the Kronecker delta, $\mathbf{C}^0$ is the volume average stiffness tensor, C_{ql}^{-1} is the local compliance tensor and the derivative is the tangent compliance tensor derived from the constitutive relation (3.2). An approximation of the tangent compliance can be calculated if the dependence of the critical resolved shear stress τ when taking the derivative is neglected, primarily because that dependence depends on the hardening law being used at the time. The resulting approximation is shown as

$$\frac{\dot{\epsilon}_q^p}{\sigma_l} \bigg|_{\sigma_k^{(i+1,j)}} \approx n\dot{\gamma}_o \sum_{s=1}^{N_s} \frac{m_q^s m_l^s}{\tau_o^s(\boldsymbol{\sigma}^{(i,j+1)})} \left(\frac{\boldsymbol{m}^s : \boldsymbol{\sigma}}{\tau_o^s(\boldsymbol{\sigma}^{(i,j+1)})} \right)^{n-1} \tag{3.15}$$

Once the NR calculation is completed, the new stress obtained is used as the new input for the Green's function method $\boldsymbol{\lambda}^{(i+1)}$. There is an optional step that allows the application of mixed boundary conditions, with the addition of stress to the already present strain boundary conditions. This additional step occurs in between iteration steps and the calculation takes the form of a correction to the strain based on a difference in stress as shown

$$e_{ij}^{(i+1)} = e_{ij}^{(i)} + {C_{ijkl}^o}^{-1} a_{kl} \left(\Sigma_{kl} - \left\langle \lambda_{kl}^{(i+1)}(x) \right\rangle \right) \tag{3.16}$$

where $\boldsymbol{\Sigma}$ is the stress boundary condition tensor, the inverse $\mathbf{C}^0$ is the volume average compliance tensor and **a** is a tensor indicating which components of stress conditions need to be followed by having a value of 1 for those components and 0 for the rest.

These iterations are continued until the average l^2-norm of the difference between previous stress and strain and new stress and strain tensors is below some threshold that in this work is held to be 10^{-6}. Once this condition is achieved the calculation of the local responses derived from the applied boundary conditions is complete. From here there are two updates to the microstructure that the applied deformation induces. The first update is for the lattice reorientation associated with each material point, which is dictated by the equation shown

$$\omega_{ij}(x) = [\dot{\omega}_{ij}(x) - \dot{\omega}^p_{ij}(x)]\Delta t \tag{3.17}$$

where $\boldsymbol{\omega}(x)$ is the local lattice reorientation, $\dot{\boldsymbol{\omega}}(x)$ is the local rigid body rotation rate and $\dot{\boldsymbol{\omega}}^{\boldsymbol{p}}(x)$ is the local plastic rotation. The local rigid body rotation is defined by

$$\dot{\omega}_{ij}(x) = \frac{1}{2}(v_{i,j}(x) - v_{j,i}(x)) \tag{3.18}$$

where $v_{i,j}$ is the local velocity gradient (the time derivative of the displacement gradient). The local plastic rotation is defined by

$$\dot{\omega}^p_{ij}(x) = \sum_{\alpha=1}^{N_\alpha} \beta^\alpha(x)\dot{\gamma}^\alpha(x) \tag{3.19}$$

where $\dot{\gamma}^\alpha(x)$ is the local shear rate on slip system α (defined in 3.2) and $\beta^\alpha(x)$ is the local antisymmetric Schmid tensor for slip system α, which is defined as

$$\beta^\alpha_{ij} = \frac{1}{2}(s^\alpha \otimes n^\alpha - n^\alpha \otimes s^\alpha) \tag{3.20}$$

where s^α is the slip direction and n^α is the slip plane normal. The second update is for the local critical resolved shear stress (CRSS) at each material point via hardening. In this work a Voce-type hardening model is used. The primary CRSS update formula is based on the amount of slip on each slip system:

$$\Delta\tau^{\alpha} = \frac{d\bar{\tau}^{\alpha}}{d\Gamma}\sum_{\beta} h^{\alpha\beta}\dot{\gamma}^{\beta} \tag{3.21}$$

where $\dot{\gamma}^{\beta}$ is the shear rate of slip system β, $h^{\alpha\beta}$ is a hardening matrix that dictates how different slip systems harden each other (when α=β it is self-hardening, when α≠β it is latent hardening) and the leading derivative is derived from the modified Voce hardening law[65]

$$\bar{\tau}^{\alpha} = \tau_0 + (\tau_1 + \theta_1\Gamma)\left[1 - exp\left(-\frac{\theta_0\Gamma}{\tau_1}\right)\right] \tag{3.22}$$

where τ_0, τ_1, θ_0 and θ_1 which are the initial CRSS, a value that when added to τ_0 is the back-extrapolated threshold stress, the initial hardening rate and the asymptotic hardening rate respectively. All these Voce parameters are determined empirically by determining what hardening parameters cause the stress-strain curve result of the elasto-viscoplastic model to fit an experimental stress-strain curve. Finally, the term Γ is the integral of accumulated net shear on all the slip systems.

From the constitutive equation (3.2), we know that the local fields depend on both the current local orientation and local CRSS. However, the update of these properties depends on the results of the local field calculations. Thus, to accurately predict the deformation history of the material these values must evolve in tandem, which in this model is performed explicitly for each boundary condition increment. The size of this increment is limited by the numerical iterative method by which the local micromechanical values are calculated. If the increment of the applied conditions is too large, the iterative method may not be able to converge upon a solution. Such a problem is not unique to this model but is inherent in many numerical methods. The elastic to plastic transition is often the limiting factor for the extent of increment that will lead to

convergence. For most cases in the EVPFFT model, the largest strain increment that can be applied while still ensuring convergence is 10^{-4}. Aside from limits on the boundary condition increment, there are also limits on how many increments can be applied while still accurately predicting the micromechanical responses. The Fourier transform method may only be performed on a microstructure grid that has uniform spacing between points, an assumption of which may be reasonable at lower levels of deformation but as strain increases the results will less accurately reflect material behavior. This limitation can be resolved through the use of dual-grid[66] or particle-in-cell[63, 67] adaptions of the EVPFFT model.

Chapter 4: Grain Boundary Normal Calculation Technique

4.1: Motivation

Grain boundaries can be characterized at the mesoscale by five parameters; three of these parameters specify the misorientation, which is the transformation that brings the crystal lattices of the grains on either side of the boundary into coincidence. The other two specify the unit vector that is locally normal to the grain boundary plane. These components are combined to produce a five-dimensional (5-D) grain boundary character. One method of visually representing the grain boundary character is to utilize grain boundary character distributions (GBCD) over the space of (3-parameter) misorientation and (2-parameter) grain boundary normal. These are generally visualized as stereographic projections of the density of interface orientations with respect to crystal axes for a particular misorientation of interest. The misorientation components are rather easily calculated because of the many ways grain crystallographic orientations can be found, such as electron backscatter diffraction (EBSD). There are a number of reasons as to why exact grain boundary normals are difficult to obtain. First, three-dimensional (3-D) information is required and this is expensive and time-consuming to acquire. The most common methods for getting three-dimensional microstructure information are serial-sectioning combined with EBSD measurements, which is a destructive technique[47], and the recently introduced non-destructive near-field high-energy diffraction microscopy (nf-HEDM)[48]. Both methods result in a series of two-dimensional (2-D) images that can then be aligned to form a 3-D image. However, the GB normals are still not easily obtained from this stack of 2-D images, due to the lack of information on the actual boundary inclination. The microstructure image obtained from EBSD or nf-HEDM is

similar to any other digital image; it consists of a grid of discrete points that does not explicitly include surfaces that would be needed to provide information on GB topology. At best, boundaries are known to lie between neighboring sets of points that belong to two different grains as shown in Fig. 4-1. However, the detailed boundary position in between the sampled points is not directly known.

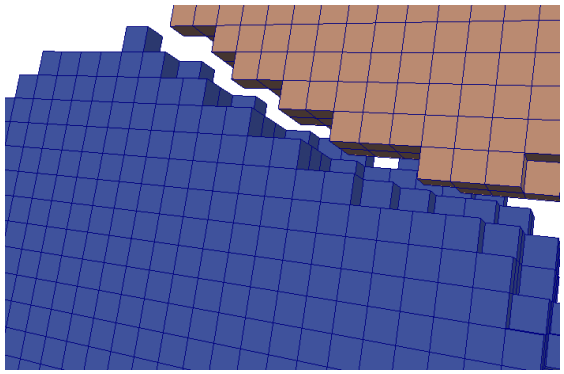

Figure 4-1. An image for two grains, where each corner of the cubic grid of lines represents a measured orientation point in the material. If all eight vertices of the cube agree in their orientation, the cube can be identified as belonging to that grain and is colored appropriately. If the eight vertices are not all in agreement, the volume must be associated with the grain boundary and is left vacant.

Requiring actual 3-D information can be avoided by using stereological methods to derive general plane normal distributions[68, 69]. However, information on individual boundaries cannot be obtained using stereology. Surface reconstruction, i.e. the method of generating surface information from a set of discrete points representing a shape, is required in order to define the missing GB information in 3-D data. This constitutes a difficult problem and many different techniques have been proposed aiming at solving it. For example, Dey and Goswami[70] developed a technique for surface reconstruction utilizing intersecting Delaunay balls to determine the surfaces. Hoppe *et al*.[71] and Mitra and Nguyen[72] generated surface information by fitting tangent planes to some specified number of local points. A similar method was developed by Ivasishin[73] who combined it

with a 3-D Monte-Carlo model. A technique by Moore and Warren[74] utilized polynomial fitting to develop polyhedral surfaces. Among surface reconstruction techniques, the most common and widely accepted way of approximating the GB surfaces is to generate a surface mesh from voxelized microstructure images. Different variants of this methodology have been proposed. One of the most used algorithms for developing a surface mesh from image data is the 'marching cubes' method[75], which is used in many software programs including the one utilized in this work, known as Dream.3D[76].

As with general surface reconstruction, the most common technique for grain boundary characterization is based upon developing an explicit surface mesh. However, there are also other methods that do not explicitly generate this mesh but still calculate surface information[77-79]. However, since the EVPFFT model works directly on a voxelized image, the previously described techniques cannot generate GB normals that are directly compatible with the local Cauchy stress tensors generated by the model and thus cannot be used to calculate grain boundary surface tractions, necessitating a technique that generates surface normals directly from the voxelized image. The methodology proposed by Ivasishin *et al.*[73] is one of the few cases of GB normals calculated directly from 3-D integer grid-based data. However, this technique was not validated against experimental microstructures. Another example of GB information inferred from voxelized images is that of Chandross *et al.*[80], who, however, focused on obtaining dihedral angles at triple lines. A method proposed by Chou and Gholinia[81] is another similar method calculating from voxelized images, in particular the part of the

method involving calculations over local spherical region of the image, but this technique calculates the surface normals relative to each voxel face.

To properly analyze tractions from the EVPPFT model, we develop a new method based on the gradients of binary indicator fields determined from the voxelized image data. We validate this technique by comparing the surface normals determined by the new technique with those calculated from a surface mesh with triangular elements, obtained using Dream.3D, on a synthetically generated microstructure. Based on the analysis of these synthetic cases, the method is further utilized to obtain the GBCD of a pure nickel 3-D microstructure image obtained by nf-HEDM in Section 3.4. These results are compared to the GBCD previously determined by Hefferan[53, 82, 83] for the same microstructure, but using a different surface reconstruction technique that instead utilizes the Computational Geometry Algorithms Library (CGAL) package. CGAL is software that is used to model surfaces for many applications ranging from Materials Science to Geology to Biology[84-86], to mention a few examples. Its algorithm is based on Delaunay refinement.

4.2: Cartesian Moment Method

A technique is presented here that can approximate grain boundary plane normals directly from 3-D microstructure data through the use of first order Cartesian moments. The equation for finding general Cartesian moments of arbitrary order[87, 88] is

$$M_{opq} = \iiint_S w(\boldsymbol{r}) x^o y^p z^q f(\boldsymbol{r}) d\boldsymbol{r} = \sum_{(i,j,k)\in S} w(\boldsymbol{r}) x_i^o y_j^p z_k^q f(\boldsymbol{r}) \qquad (4.1)$$

The order of a moment is determined by the sum of its indexes, represented here by the non-negative integers o, p and q. The function $w(\mathbf{r})$ is a weighting function that depends

upon the position $\mathbf{r} = (x_i, y_j, z_k)$ within the volume of interest S. The weight is often taken to be simply 1 for all points within S, but more generally it can be specified to have a range of values depending on the particular application. The function $f(\mathbf{r})$ is a scalar field that will be used as the indicator function. Some examples of scalar fields that can be used as indicator functions are composition, misorientation angle or von Mises equivalent stress. In this work, we use a *binary* indicator function. Such functions, which can adopt values of 0 or 1, are used to establish which points are part of the object of interest and which are not. For our present application, we know to which grain each voxel belongs, so we define an integer function $h(\mathbf{r})$ that returns the grain number for that location. The indicator function $f(\mathbf{r})$ is then defined as the delta function between the desired grain number m and the actual grain number $h(\mathbf{r})$: $f(\mathbf{r}) = \delta(m,h(\mathbf{r}))$. The function is 1 if the grain numbers match, and zero otherwise, and this would select out the volume elements belonging to grain m. Typically, the origin of the coordinate frame is selected as the center of position of the object of interest and the resulting evaluations define the *central* moments. Moment invariants can then be calculated from the central Cartesian moments of such binary indicator function, and these in turn can be used to characterize the shape of the object in a variety of ways[87, 88].

A related moment formulation can be used to define the local derivatives of the indicator function and provides a formal way of defining the edges and surfaces of an object[89-91]. Here, in particular, we are interested in calculating the surface normal of the grains, which are parallel to the gradient of the grain number indicator function[92-94]. Because the data is present on a regularly spaced grid, the gradients can be defined by the least-square formulations given in (4.2)[95-97].

$$\left.\frac{\partial f}{\partial x}\right|_{(0,0,0)} = \frac{\sum_{(i,j,k)\in S} w(\boldsymbol{r}) f(\boldsymbol{r}) x_i}{\sum_{(i,j,k)\in S} w(\boldsymbol{r}) x_i^2} = \frac{\sum_{(i,j,k)\in S} w(\boldsymbol{r}) f(\boldsymbol{r}) i}{\Delta x \sum_{(i,j,k)\in S} w(\boldsymbol{r}) i^2}$$
$$\left.\frac{\partial f}{\partial y}\right|_{(0,0,0)} = \frac{\sum_{(i,j,k)\in S} w(\boldsymbol{r}) f(\boldsymbol{r}) y_j}{\sum_{(i,j,k)\in S} w(\boldsymbol{r}) y_j^2} = \frac{\sum_{(i,j,k)\in S} w(\boldsymbol{r}) f(\boldsymbol{r}) j}{\Delta y \sum_{(i,j,k)\in S} w(\boldsymbol{r}) j^2} \tag{4.2}$$
$$\left.\frac{\partial f}{\partial z}\right|_{(0,0,0)} = \frac{\sum_{(i,j,k)\in S} w(\boldsymbol{r}) f(\boldsymbol{r}) z_k}{\sum_{(i,j,k)\in S} w(\boldsymbol{r}) z_k^2} = \frac{\sum_{(i,j,k)\in S} w(\boldsymbol{r}) f(\boldsymbol{r}) k}{\Delta z \sum_{(i,j,k)\in S} w(\boldsymbol{r}) k^2}$$

Here, in order to simplify the notation, we have shifted the origin to the center of the voxel of interest and define it to have the (*i,j,k*) indices of (0,0,0). The summations over (*i,j,k*) are within a region *S* which is used to evaluate the derivative. That defines a neighborhood about that central voxel, where the indices define the positions of the other voxels relative to it. The specifics of the weighting function $w(\mathbf{r})$ will be discussed in further detail below. For the regularly spaced grid, the distance vector is defined as:

$$\boldsymbol{r} = (x_i, y_j, z_k) = (i\Delta x, j\Delta y, k\Delta z) \tag{4.3}$$

Here, we emphasize that it is not required that the grid spacings (Δx, Δy, Δz) in the three different directions be equivalent. This is especially convenient as both the experimental data (EBSD, nf-HEDM) and results of the Fourier Transform-based simulations often have this attribute. The derivative evaluations can then be reduced to a somewhat simpler computational form shown in the second set of equalities in (4.2).

The numerators of the first set of equalities in (4.2) are seen to be the first order Cartesian moments within the neighborhood, and that these are proportional to the components of the gradient of $f(\mathbf{r})$, with the proportionality depending upon the definition of $w(\mathbf{r})$[89, 90]. We note that the use of this formulation requires that $w(\mathbf{r})$ and the definition of the neighborhood *S* be symmetric about the origin in addition to the data being present

on a regularly spaced grid. More complex formulations must be utilized if these conditions are not met. Our formulations can be further simplified by treating the indices in the three directions equivalently. This can be achieved by requiring the weighting function to be simply a function of the sum of the squares of the indices, reducing its dependence from a vector to a scalar quantity. A similar constraint on the definition of the neighborhood *S* is adopted as shown in (4.4) and (4.5).

$$w(\boldsymbol{r}) \to w(i^2 + j^2 + k^2) \tag{4.4}$$

$$(i, j, k) \in S \forall \left[i^2 + j^2 + k^2 \leq s^2 \right] \tag{4.5}$$

Under these conditions, the summations in the denominators in the second equalities of (4.2) become equivalent, and that is designated as the quantity *W*. This also enforces an equivalent statistical treatment of the gradient evaluation that is independent of the direction and specific axes orientation. The resulting formulations can then be simplified as in (4.6), where the scaled first order moments μ_{opq} are defined.

$$\begin{aligned}
\mu_{100} &= \frac{1}{\Delta x} \sum_{(i,j,k)\in S} w(\boldsymbol{r}) f(\boldsymbol{r}) i = W \frac{\partial f}{\partial x}\Big|_{(0,0,0)} \\
\mu_{010} &= \frac{1}{\Delta y} \sum_{(i,j,k)\in S} w(\boldsymbol{r}) f(\boldsymbol{r}) j = W \frac{\partial f}{\partial y}\Big|_{(0,0,0)} \\
\mu_{001} &= \frac{1}{\Delta z} \sum_{(i,j,k)\in S} w(\boldsymbol{r}) f(\boldsymbol{r}) k = W \frac{\partial f}{\partial z}\Big|_{(0,0,0)}
\end{aligned} \tag{4.6}$$

As mentioned above, here we are interested in the direction of surface normal and do not need to know the magnitude of the gradient. Consequently, these vector components can then normalized by the vector magnitude to generate a unit vector whose direction is the surface normal. Relationships for higher order derivatives could be similarly defined from the higher order moments to evaluate the grain surface curvature and triple junction characteristics, and those will be discussed in subsequent work.

Here, we just utilize first order Cartesian moments and in three dimensions these have indexes of 100, 010 and 001 for the x, y and z directions, respectively. The origin of the calculation volume is located at the center of the voxel found to be part of the surface of the shape, defining $(i,j,k) = (0,0,0)$. Then the gradient components represent a vector that is in the same direction as the normal vector to that surface. Here, because we know the identities of the grains to which each voxel belongs, we designate the surface voxels as simply being those for which at least one of the six face-sharing neighbor voxels belongs to a different grain. For evaluations centered on voxels located internally to the grain, small gradients that point towards the surface would arise if the voxel is sufficiently close to the surface. This is of significance only if the grain identities and surface points are not known *a priori*, but does not impact the current study.

In the present case of analyzing grain structure, the binary indicator function requires special consideration since there is the possibility of a point having nearest-neighbor points belonging to more than one different grain. Such points are designated *triple points* in the case of a total of three grains, or *quad points* in the case of four grains. Thus, to properly describe the surface at and near these points, the binary indicator function is modified be such that the points that are in the same central grain m are assigned a value of 0, the points in the one special neighboring grain n hold a value of 1, and all other points are also assigned a value of 0. Therefore, we modify the definition of the indicator function as follows: for defining the surface normal of a cell belong to a grain of type m with respect to a second grain of type n, $f(\mathbf{r}) = \delta(n,h(\mathbf{r}))$. Therefore for each point with l unique grain numbers among its nearest neighbors, there will be l-1 unique binary indicator functions, as shown in Fig. 4-2. By having multiple binary indicator functions at

a single triple point, we ensure that each vector calculated represents the surface between two grains. The points other than point 10 above that are highlighted by boxes show how regular grain boundary voxels near triple points will only be influenced by the single neighboring grain with no contribution from the nearby but not adjacent third grain.

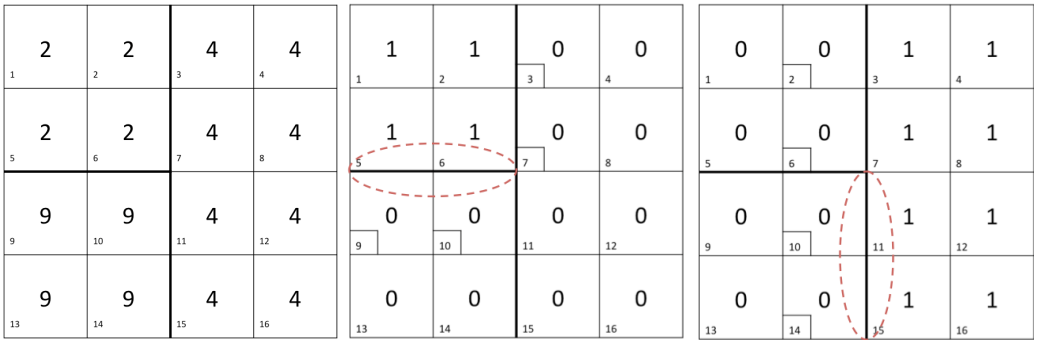

Figure 4-2. Example of the two indicator functions generated at point 10, which is the point in grain ID 9 that is at a triple point. The left figure shows the grid with the grain ID number in the center, and the point number (small font) in the bottom left corner of each cell. The middle and right figures show the two different indicator functions associated with point number 10, the first being between grains 9 and 2, and the second being between grains 9 and 4 (boundaries circled by dotted line). The point numbers highlighted by boxes are those that would use the kind of shape function presented in the image, showing that points that are not directly associated with triple lines are also affected by this, depending on the neighborhood size.

The three variants of the moment calculation that we will test are primarily different in terms of the weighting function $w(\mathbf{r})$ utilized in (4.2) and (4.6). The first variant studied here is inspired by techniques used in the general image processing literature, which utilize a Gaussian weighting function or *kernel*, $w(\boldsymbol{r}) = \exp\left[-(i^2 + j^2 + k^2)/\lambda^2\right]$, to effectively smooth the discrete data to a continuous function[90, 91, 98]. The derivatives of that smoothed function can then be readily calculated and used to identify edges, corners and similar features. Similar calculation has been performed with the Deriche filter[89], another function often used to smooth discrete data. For this kernel, the value of λ defines the radius within which the data has significant weighting (i.e., the weight is < 1/*e*

beyond that radius). To define the computational neighborhood S as described in (4.5), we use a value of s determined for when the weighting function decreases below a somewhat arbitrary value of 10^{-5}. Beyond that radius, we set $w(\mathbf{r}) = 0$. Hence, the values of λ and s are interrelated: $s = (\lambda/2)\ln(10^{-5})$. The values of λ that are tested in this work are √3, √6 and √9, which result in s values of 5.88, 8.48 and 10.18 respectively. Of particular significance for the Gaussian weighting function is that there exists a general lower limit of λ = √2 which generates a smooth function from regularly spaced discrete data[90, 98], and that neither adds nor subtracts extrema (minima, maxima, inflection points) to the raw discrete data. Somewhat larger values then add a level of smoothing to the data, which is desirable for data containing noise or uncertainties. Smaller values of λ could be used to define the local derivatives at the grid points themselves, but these could not be used for general points in space. Because there is a level of noise/uncertainty in this data, the comparison will start at √3, which was sufficient to filter that uncertainty, but did not noticeably remove any extrema. For the rest of this work this variant will be referred to as the Gaussian Weighting (GW) variant.

The second variant treats every point within some specified cut-off radius, l, as having equal weighting. That is, $w(\mathbf{r})=1$ for $(i^2 + j^2 + k^2) \leq l^2$ and $w(\mathbf{r})=0$ for $(i^2 + j^2 + k^2) > l^2$. This method will be tested with values of l being √3, √6 and √9. Because of this hard-cut on the radius, the neighborhood S can be defined to have this same radius $s = l$. A comparison of the difference in weighting between these two variants is shown in Fig. 4-3. Both of these approaches strive to define an spherically symmetric neighborhood over which to define the moments/gradients. Many earlier approaches are based on cubic neighborhoods, which add some bias for alignment of the gradients along the axis

directions[90, 91, 98]. The GW method deprecates the contribution of more distant neighbor cells with respect to the primary nearest neighbors as a function of distance, enhancing the locality of the measure despite the large neighborhood. The second variant treats all included points equally, smoothing the data more broadly within that footprint. For the rest of this work this second variant will be referred to as the Non-scaling, Equal Weighing (NEW) variant. By increasing the values of (λ, l) and increasing the volume included in the evaluation, one basically biases the results towards smoother and flatter surfaces, while decreasing those values enhances errors due to noise and the discrete nature of the data. The unknown factor is how much smoothing is required to suppress those errors without smoothing the true structure too far towards a planar surface.

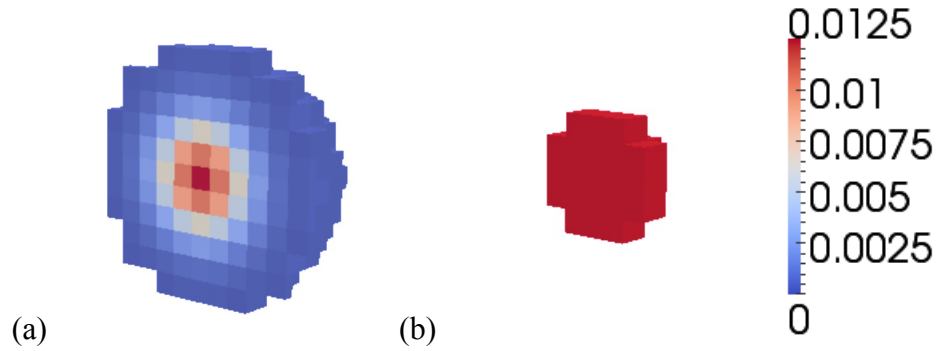

Figure 4-3. Normalized weighting factor relative to a central point using (a) GW with $\lambda=\sqrt{6}$ and (b) NEW with $l=\sqrt{6}$.

The third variant also treats every point within some cut-off radius l as having equal weighting, but the value of l is allowed to vary. Specifically, the value of l is determined as being the distance to the nearest triple junction or quad point, but its value cannot go below a fixed minimum value, l_{min}. The value of this minimum will be varied for the different test cases and is set to values of $\sqrt{3}$, $\sqrt{6}$ and $\sqrt{9}$ so that these results can be compared to the second variant. The purpose of the adaptable, scaling neighborhood is to

smooth out the larger boundary areas while preserving accuracy near the surface discontinuities (i.e. triple junctions). For the rest of this work, this variant will be referred to as the Scaling, Equal-Weighting (SEW) variant. All distance values for these three variants are evaluated and the results compared against an independent calculation of surface normals.

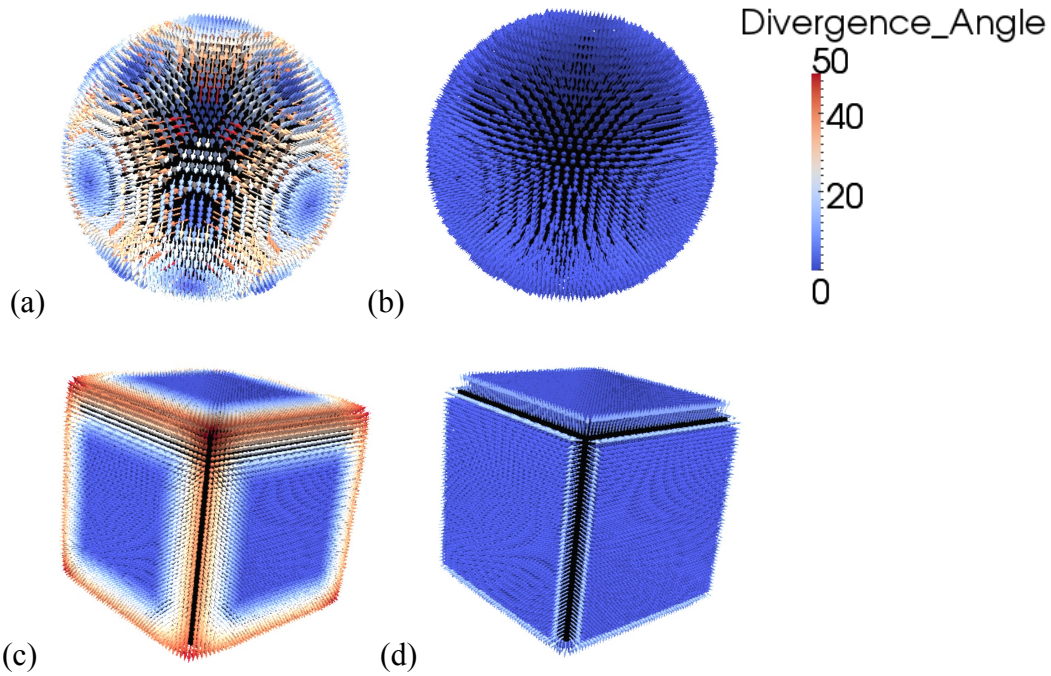

Figure 4-4. Surface normals for (a) a sphere using the NEW variant and *l* equal to √3, (b) a sphere using the second variant and *l* equal to half the radius, (c) a cube using the NEW variant and *l* equal to half the edge length and (d) a cube using the SEM variant and a minimum l_{min} of √3. All vector arrows colored by divergence angle using the same color scale as shown. The cubes show how scaling limits the smoothing of sharp edges.

To highlight the effect of the size of the neighborhood, Fig. 4-4 shows the divergence angle between calculated normals and true normals for a sphere and a cube using different variants. The divergence angle is defined as the angle that exists between the surface normals generated by this technique and the surface normals they are being compared against. The equation to calculate the divergence angle is:

$$\theta_{div} = cos^{-1}\left(\frac{\vec{v}_T \cdot \vec{v}_C}{\|\vec{v}_T\|\|\vec{v}_C\|}\right) \tag{4.7}$$

Here, $\vec{v}_T$ and $\vec{v}_C$ are the two surface normals being compared. For the first sphere (Fig. 4-4a), the NEW variant is used as the method of smoothing with $l = \sqrt{3}$. These results highlight the issue of discretization (i.e. stair-stepping); by representing a smooth sphere as a collection of cubes, the approximate surface is inherently rough, especially where it does not align well with the mesh, and errors are made in the surface normal calculations. For the value of $l = \sqrt{3}$, the result is an average divergence angle of ~21°. The result can be improved on by utilizing a larger value of l to achieve greater smoothing. For the second sphere (Fig. 4-4b), l is set to half the radius of the sphere, which results in a dramatically smaller average divergence angle of ~1°. Even if the sphere size is increased, a sufficiently large l will calculate the correct surface normals due to the high symmetry of a sphere. However, the penalty for using such a large footprint is illustrated for the first cube (Fig. 4-4c). Here, the NEW variant is used with l set to half the cube edge length, and the average divergence angle is found to be ~14°, where there is an excessive rounding of the cube corners. For the second cube (Fig. 4-4d), the third variant is used with the edges of the cube treated as triple points, which results in greater accuracy close to the edges of the cube. Setting the value of l_{min} to $\sqrt{3}$, the average divergence angle decreases to ~1°. The size of the cube can then increase freely as long as the value of l is controlled such that it does not extend beyond the corners. These test cases emphasize that one should keep the neighborhood as small as possible in order to avoid these corner-rounding effects, albeit that smaller neighborhoods can increase the level of error arising from stair-steps. The SEW variant was constructed as a compromise between these factors as well as a way of scaling with different grain sizes. However, the

location of the edges/triple junction must be known to use the third variant of the technique because they are utilized to determine l_{min} and such information may not always be available.

4.3: Mesh Comparison

One method to evaluate these approaches is to generate a surface mesh of a microstructure image and compare the surface normals from the mesh to those found by the proposed technique for the same image. To do this, the synthetic microstructure shown in Fig. 4-5 is used. It was generated using MBuilder[99, 100] and it has 860 grains discretized onto a 128x128x128 voxel grid. A triangular surface mesh for this microstructure is generated using the Dream.3D software package with a marching cubes algorithm and smoothed with a Laplacian smoothing algorithm for 40 iterations. Some conversion steps are needed in order to obtain a one-to-one comparison between the surface normals of the mesh and those of the proposed technique. First, all the nearby nodes to a given grain boundary voxel are identified, then the surface normals of the triangle elements which include those nodes are averaged with a weighting based on the triangle area. In particular the triangle elements used in the averaging are only those that are associated with the same grain boundary number pair as those of the grain boundary voxel. Thus if the grain boundary voxel is on a triple line, then two vectors from the triangle mesh will be generated for both possible grain number pairs.

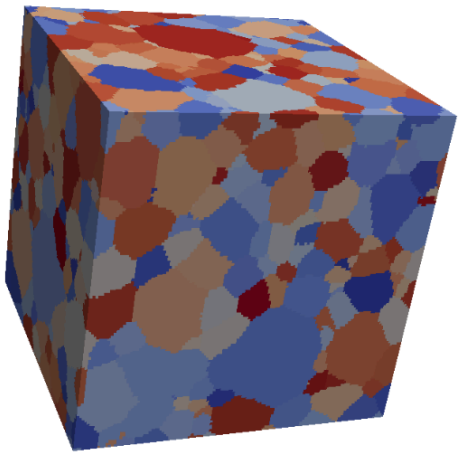

Figure 4-5. The synthetic microstructure used to validate the grain boundary normal technique.

The angle between this approximated surface normal from the mesh and the surface normal calculated by our techniques represents a measure of how different the two sets of normal vectors are, with a value of 0˚ indicating complete agreement between them. Here, we use this angle as a measure of the accuracy of the technique with the aim being to find conditions that minimize the angles. For each of the nine cases described in Section 4.2, we determined the divergence angle for each grain boundary surface normal calculated from the image. The probability distribution of the divergence angles for each test case is shown in Fig. 4-6, with the results split between grain boundary voxels with a distance to the nearest triple point of one or less, and those with a distance greater than one. We make this distinction because there are greater uncertainties about the surface normals near triple junctions, due to both resolution related issues as well as difficulties that both our currents techniques and surface meshing techniques might have in that vicinity. These probability distributions show that, for each model variant, one can identify a preferred setting that results in the lowest average divergence angle for voxels that have a triple point distance greater than one. We also note that these lowest average

divergence angles are fairly close to each other. These conditions are $\lambda=\sqrt{3}$ for the GW variant, $l=\sqrt{6}$ for the NEW, and $l_{min}=\sqrt{6}$ for the SEW variants. Also, we observe that the distributions for voxels that have a triple line distance less than or equal to one are reasonably insensitive to the choice of technique used, although the divergence angle is generally larger for points on triple lines than the other points. For completeness, we also characterized $\lambda=\sqrt{2}$ for the GW variant, but those results were of lower quality than for $\lambda=\sqrt{3}$.

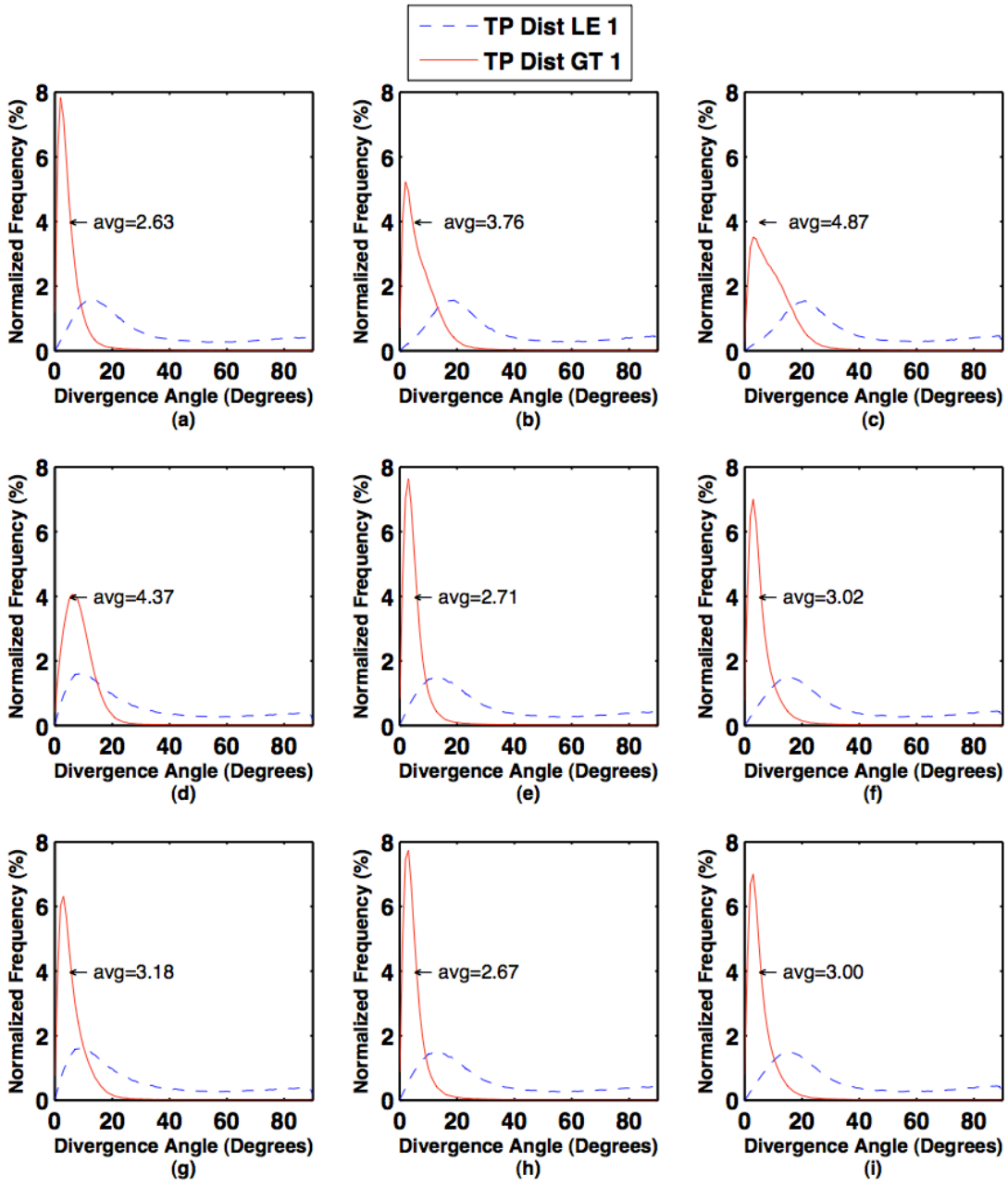

Figure 4-6. Probability distributions of the nine test cases, with the data separated into voxels with a triple point distance of one or less (blue) and voxels with a triple point distance greater than one (red). The average divergence angle of the red curve is displayed on each graph. The GW variant is represented by (a), (b) and (c) for λ=√3, √6 and √9 respectively. The NEW variant is represented by (d), (e) and (f) for l =√3, √6 and √9 respectively. The SEW variant is represented by (g), (h) and (i) for l_{min}=√3, √6 and √9 respectively.

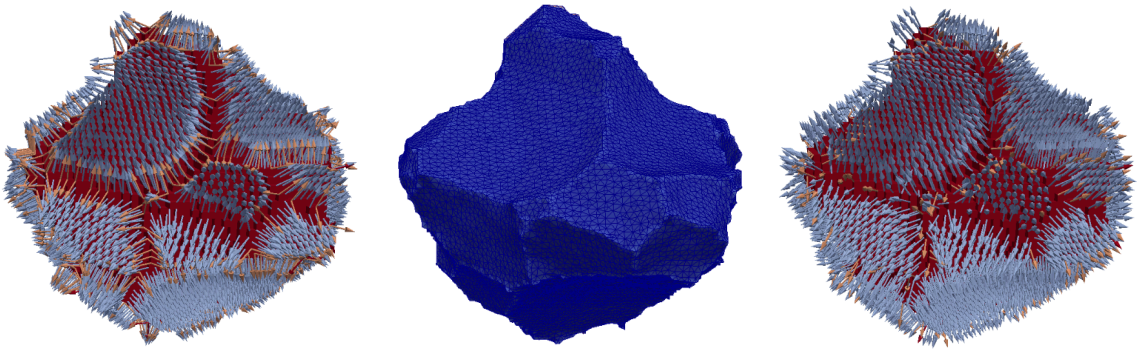

Figure 4-7. Grain boundary normals for a particular grain are shown for the scaling, equal-weighting model variant with $l_{min}=\sqrt{6}$ (left) and for the normals from the mesh (right), with the mesh itself also shown (center). The vectors are colored by the number of nearest-neighbor grains.

The grain boundary normal vectors generated from the mesh and from the scaling, equal-weighting variant for a particular grain are shown in Fig. 4-7, along with the underlying triangular mesh. The images show that both cases reflect relatively smooth surfaces away from the triple junctions. However, for the grain boundary normals approximated from the mesh, there is great variation in the normals at the triple junctions. This is likely due to irregularities in the mesh smoothing in these areas, which can be seen in the center image of Fig. 4-7. These irregularities are reflected in the higher divergence angles measured on voxels in these areas. From these results we can conclude that, at least for this microstructure, all three variants of the technique, for at least one value of (λ, l, l_{min}), are reasonably accurate at determining grain boundary normal vectors when compared to those from the standard method based on triangular surface meshes.

4.4: GBCD Comparison

Next, we compare our normal vector approximations to those obtained from a state-of-the-art meshing algorithm applied to an experimentally measured 3D microstructure. The comparison is statistical in that we compare grain boundary normal distributions rather

than point-by-point values as above. This comparison is carried out for two specific misorientations, thus displaying two-dimensional subspaces of the complete, five-parameter GBCD. The normals are shown in crystallographic coordinates, with each normal appearing twice, once for each of the neighboring crystals.

The sample used is pure nickel while the measurement was performed by Hefferan *et al.*[53, 82, 83] using nf-HEDM[48, 101]. The nf-HEDM reconstruction yields a set of triangular voxels (in this case 1.2 micron side length equilateral triangles) in each of a set of 71 measured 2-D sections that are spaced in 4 micron intervals perpendicular to the section planes. This structure was interpolated onto a cubic lattice, as shown in Fig. 4-8a. The grain boundaries were meshed using a weighted Delaunay triangulation method developed by S.F. Li[102]. It utilizes algorithms available in the Computational Geometry Algorithms Library (CGAL)[103] package with adaptations influenced by Boltcheva *et al.*[104] to preserve important features, such as triple lines and quad points. The resulting mesh of this Ni microstructure is shown in Fig. 4-8b.

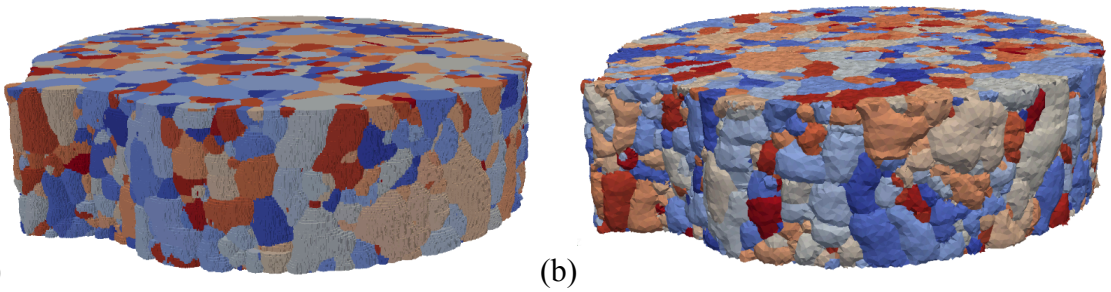

(a) (b)

Figure 4-8. (a)Pure nickel microstructure from Hefferan *et al.*[53, 82, 83] has a resolution of 1000 x 1000 x 71 points with spacing of 1.2x1.2x4 µm. (b) Surface mesh generated for this image. In both case, the false color is based on randomly assigned grain number ID's.

Using the meshed boundaries, Hefferan[53, 83] displayed the normal distributions for two specific crystallographic misorientations, denoted as the Σ3 (60° rotation around the

<111> axis) and Σ9 (38.94° rotation around the <110> axis) boundaries. To generate the GBCD, the grain boundary surface normals are transformed into the crystallographic reference frame of their respective grains and then represented as a stereographic projection of the rotated vectors, with only the grain boundary points that have the misorientations of interest being included. Before rendering the vectors as a stereographic projection, the vectors are first transformed into spherical coordinates and then binned by 10° intervals. The bins are then normalized such that they are expressed as multiples of random density. The values of (λ, l, l_{min}) found in Section 4.3 that resulted in the greatest accuracy for each variation of the technique are used to generate GBCD from the nf-HEDM images. The Σ3 grain boundary character distributions generated from the surface meshing and the three variants of the technique are shown in Fig. 4-9.

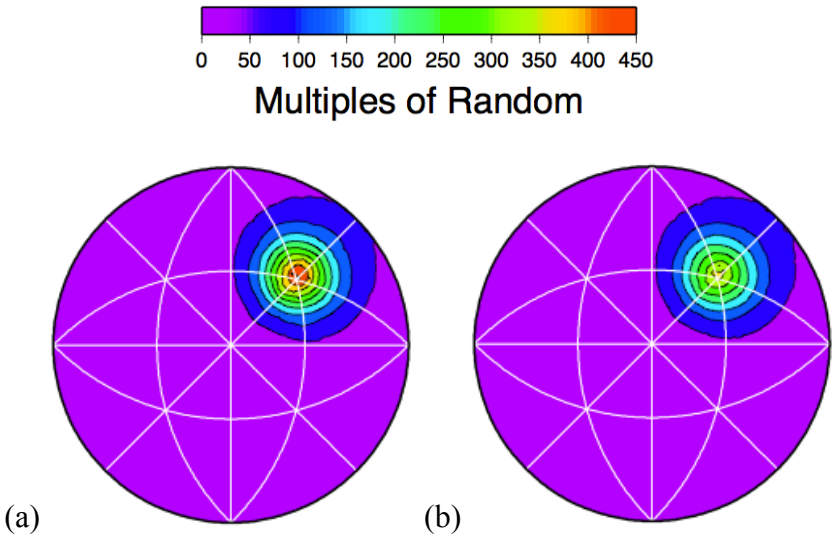

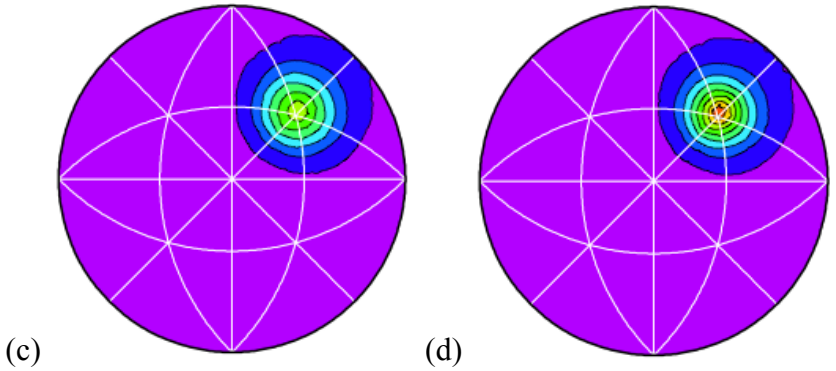

(c) (d)

Figure 4-9. Σ3 GBCD (a) from Hefferan *et al.*[53, 83], (b) the GW variant of the proposed model with λ=√3, (c) the second variant (NEW) with *l*=√6 and (d) the SEWvariant with l_{min}=√6. The strong peak in the upper right quadrant is associated with coherent twin boundaries, which are very common in most annealed fcc metals such as the Ni studied here.

What we see from these GBCD is that each model variant shows a very similar distribution shape but the primary difference is in the spread and peak of the distributions. The GBCD that is closest to Hefferan's Σ3 baseline, in terms of peak value, is obtained with the SEW variant, followed by the GW variant with the NEW variant being the least accurate. To quantify this comparison, Fig. 4-10 shows these same projections but colored by the value of the difference between with respect to Hefferan's GBCD. The largest absolute difference calculated in each case is 104.5 MRD for the GW variant, 143.6 MRD for the NEW variant and 50.9 MRD for the SEW variant; these results are also shown in Table 4-1.

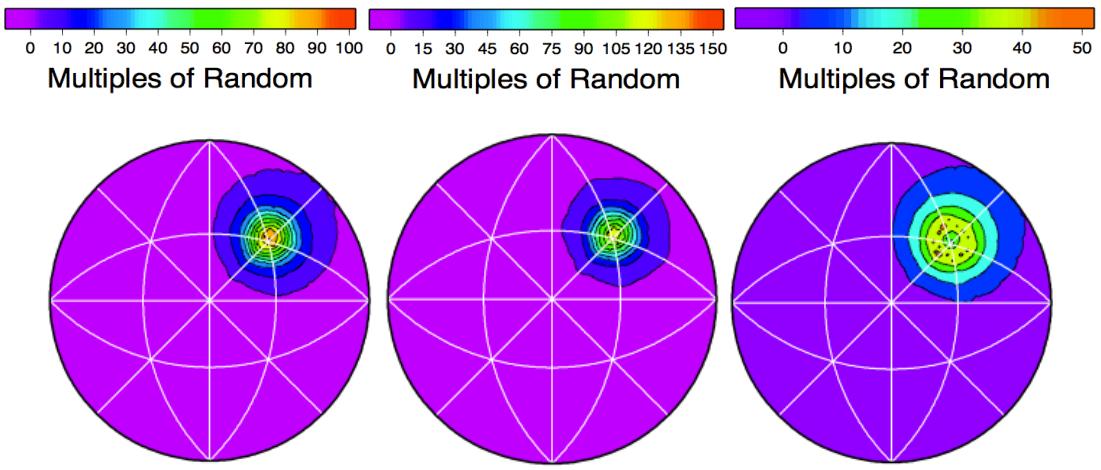

Figure 4-10. Difference in MRD values for Σ3 boundaries between Hefferan's GBCD and the GBCD from (left) the GW variant, (center) the NEW variant and (right) the SEW variant.

	Difference in Σ3 GBCD (MRD)	Difference in Σ9 GBCD (MRD)
GEW	104.5	2.03
NEW	143.6	2.80
SEW	50.9	2.16

Table 4-1: Peak Difference in MRD between the GBCD from Hefferan and the GBCD generated by the three variants for both Σ3 and Σ9 boundaries.

In particular, the largest difference for the SEW variant is not located at the standard Σ3 GBCD peak, as it is for the other two. The Σ9 grain boundary character distributions generated from the surface meshing and the three versions of the technique are shown in Fig. 4-11.

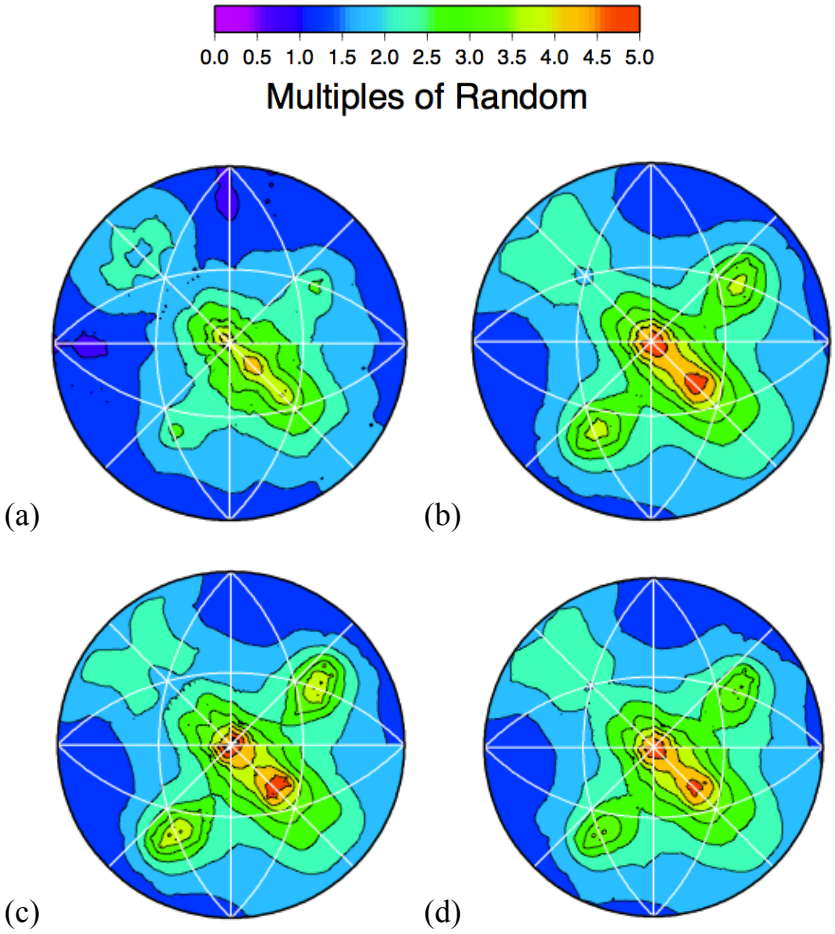

Figure 4-11. Σ9 GBCD (a) from Hefferan *et al.*[53, 83], (b) the first variant (GW) of the proposed model with λ=√3, (c) the NEW variant with l=√6 and (d) the SEW variant with l_{min}=√6.

Again the different variants of the technique show general agreement on the shape of the distribution but here there are more differences when compared to the Σ9 baseline in that the peaks do not exactly line up, though they are all on the same <110> tilt profile, and the secondary shapes in the distributions are also slightly different but occur in the same positions in the plot. Again, the differences between the GBCD from Hefferan and the GBCD from this technique are shown in Fig. 4-12. The largest absolute difference calculated in each case is 2.03 MRD for the GW variant, 2.80 MRD for the NEW variant

and 2.16 MRD for the SEW variant. These results are also shown in Table 4-1. The NEW variant is the most different from Hefferan's GBCD and is also farther from the other two

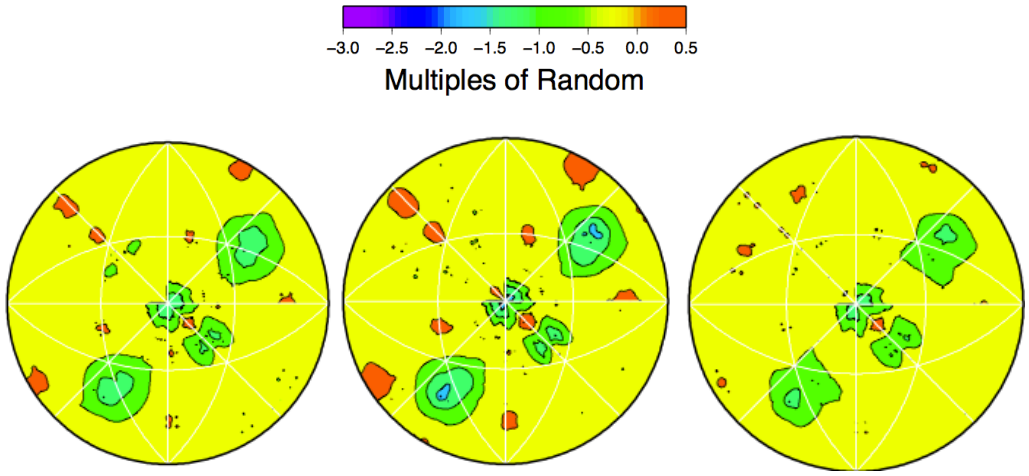

Figure 4-12. Difference in MRD values for Σ9 boundaries between Hefferan's GBCD and the GBCD from (left) the first variant (GW), (center) the second variant (NEW) and (right) the third variant (SEW).

variants, which are themselves quite similar in their differences compared to Hefferan's. Overall, the Σ9 GBCD from the technique have greater relative differences to Hefferan's Σ9 GBCD, than for the Σ3 GBCD, though the magnitudes are smaller. In general, the GBCD obtained from the SEW variant exhibits the best agreement with Hefferan's. The explanation for why the SEW variant is favored here while in Section 4.3 all three had similar accuracy is that the resolution of the nf-HEDM sample (71×10^6 voxels) is greater than that of the synthetic microstructure ($\sim2\times10^6$ voxels) and this particular variant has a consistent smoothing effect with increasing resolution while the other two are indifferent to resolution changes.

4.5: Triple Junction Line Vectors

While the above technique, presented in Lieberman *et al.*[13], can define the grain boundary surface normals, it does not describe the triple junctions themselves as distinct

structures and thus a separate technique must be found. As Fig. 1-1 shows, damage can nucleate specifically on triple junctions so being able to analyze them as features separate from the grain boundary plane is useful. Accordingly, in order to analyze the triple junctions in addition to grain boundaries, we propose a technique that calculates the triple junction line vector using certain special properties of second order Cartesian moments as described by Lichter and Dubowsky[105]. Following the properties of the general Cartesian moment equation shown in (4.1), the second order Cartesian moments consist of six distinct values. These values are used to construct a diagonalizable symmetric matrix as shown

$$\begin{bmatrix} \mu_{200} & \mu_{110} & \mu_{101} \\ \mu_{110} & \mu_{020} & \mu_{011} \\ \mu_{101} & \mu_{011} & \mu_{002} \end{bmatrix} = P^{-1}\Lambda P \tag{4.8}$$

where Λ is a diagonal matrix composed of the eigenvalues of the second order Cartesian moment matrix and P is a matrix whose columns are the eigenvectors of the moment matrix. In this instance, a different variation of the discrete Cartesian moment equation is used as shown

$$\mu_{opq} = \sum_{(i,j,k)\in S} w(\boldsymbol{r}) f(\boldsymbol{r}) (i\Delta x)^o (j\Delta y)^p (k\Delta z)^q \tag{4.9}$$

For this technique the weighting function and volume of interest S are defined by the GW variant. If the indicator function used in the moment equation is representative of some object in space, the eigenvectors will correspond to the principal axes of that object while the eigenvalues are proportional to the relative magnitudes of size of the shape along the corresponding axes.

To make use of these properties, the triple junctions are expressed as voxelized shapes, each uniquely defined as the set of voxels that among their first nearest neighbors

have the same three grain numbers. While in continuous three-dimensional space a triple junction is a one-dimensional feature, it becomes a cylindrical voxelized shape in a discrete three-dimensional space. These cylinders have a single major principal axis and two non-unique minor principal axes. Thus the largest eigenvalue of the second order Cartesian matrix for a cylinder corresponds to the eigenvector that represents the major principal axis of that cylinder. When applied to a triple junction shape, this major principal axis is parallel to the triple junction line vector. An example of the results of this technique applied to a single triple junction is shown in Fig. 4-13. By using the two techniques of quantifying the grain boundary surface normals and triple junction tangent vectors we are able to analyze the morphological influence in void nucleation as well as calculate the surface tractions on these two features.

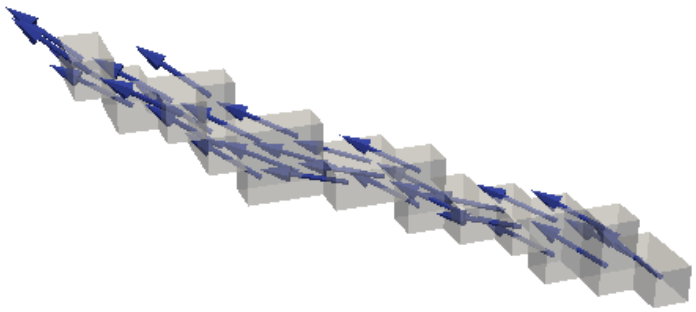

Figure 4-13. A set of voxels for a single triple line between three grains, determined by the number of unique grains amongst nearest neighbors. At each point of the triple line a local tangent vector is calculated and shown as an arrow glyph.

4.6: Discussion

The proposed technique based on the use of first order Cartesian moments to calculate a voxelized field of grain boundary normals has been shown to compare favorably to

normals found using surface meshing. When locally comparing the grain boundary normals obtained by the proposed technique to those from a triangular mesh, the greatest differences are found near the triple junctions and quad points, regions which are known to have inconsistencies with the smoothing due to most algorithms allowing triple junction nodes less freedom of positioning than other grain boundary nodes. Elsewhere the differences between the mesh normals and the normals generated by the technique are on average less than 3˚. Differences between the different variants of the technique appear when tested on the higher resolution nf-HEDM sample. The scaling, equal-weighting (SEW) variant is the one having the most success at replicating the GBCDs produced by Hefferan[53], which is reasonable considering that this variant is the only one to scale with resolution changes. This allows the smoothing to increase with increasing resolution and match the results of surface mesh smoothing that is indifferent to resolution. Thus the scaling, equal-weighting (SEW) variant is the best choice if one assumes that the boundaries being considered are smooth. However, if the above does not hold or the triple junction or other surface edge information is not known, then the Gaussian weighting (GW) variant, which had the next best success at replicating the GBCD, would be a viable option as well. We note that all of the methods exhibited higher divergence near the triple lines in the first surface mesh comparison in part because of a combination of an effective high curvature at the corners and the inability to recognize the transition between two different neighboring grains, which should give rise to a discontinuity in this simple definition of a surface normal. The addition of higher order moments/derivatives should improve the descriptions near the triple junctions. The properties of second order Cartesian moments are used to generate vectors that run

tangent to triple lines along various points of the triple junction and thus any relationship between triple junction morphology and damage nucleation may also be analyzed.

Chapter 5: Surface Traction Analysis

5.1: Simulation Setup

To analyze patterns associated with extreme values of surface tractions we must establish a statistically significant number of observations across different cases. We achieve this by performing EVPFFT simulations on multiple microstructure images and with multiple loading conditions. For this work, we ran the series of simulations on a microstructure that was generated using the software package MBuilder[99, 100]. The grain structure is the same as the one shown in Fig. 4-5. The microstructure is composed of 866 relatively equiaxed grains, with the general sizes following a log-normal distribution as shown in Fig. 5-1.

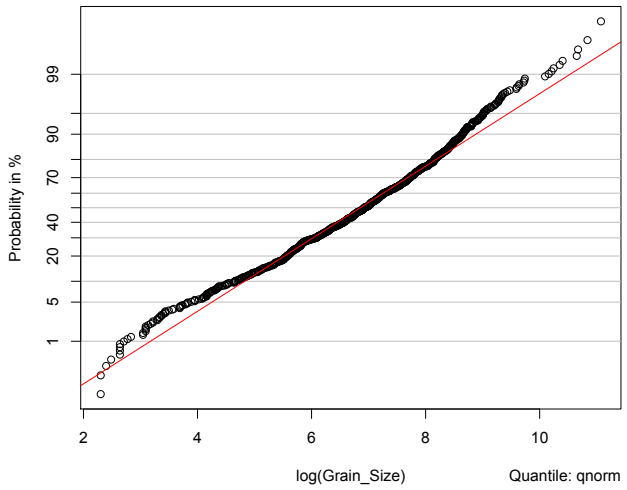

Figure 5-1. Log distribution of the grain sizes from the microstructure shown in Fig. 3-7, showing a nearly log-normal distribution.

Each grain has a single orientation that was assigned to it by the MBuilder package. By generating ten different randomizations of the orientation assignment, we produce ten microstructure images that will produce different local responses with the same grain

morphology. These orientations are expressed as Bunge Euler angles as described in Section 2.2. The orientation distribution of these grains is represented by an inverse pole figure relative to the [001] direction as shown in Fig. 5-2. Generating this inverse pole figure involves taking a chosen sample space vector (in this case [001]) and rotating the vector by the orientation on each point microstructure grid combined with each cubic crystal symmetry variation. The resulting vectors then undergo stereographic projection onto a 2D plane and a single cubic fundamental zone is selected for the plot. The inverse pole figure for this microstructure shown in Fig. 5-2 shows that the orientation distribution is not random but in fact has a ⟨100⟩ texture, though the intent was for it to be random.

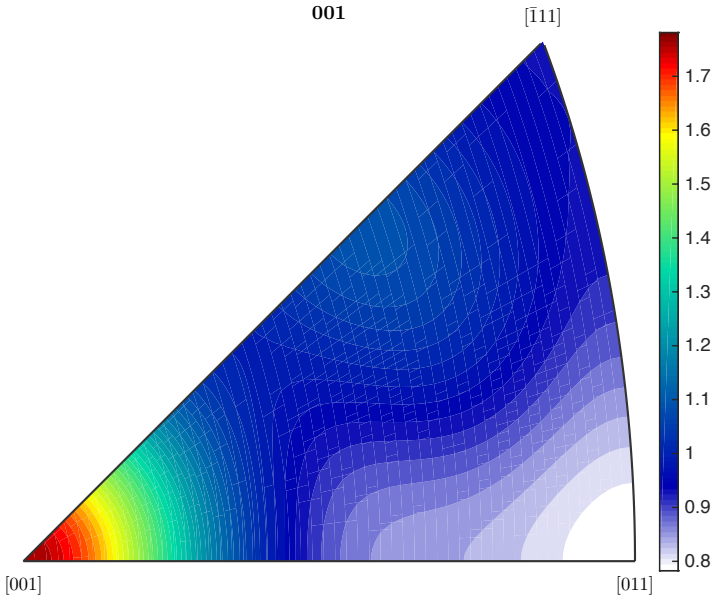

Figure 5-2 Inverse pole figure relative to the [001] direction for the microstructure shown in Fig. 4-5.

Initially we consider three different loading conditions: uniaxial tension along the *z*-axis, uniaxial compression along the *z*-axis and pure shear over the *x*-*z* plane. The EVPFFT model accepts these conditions as an applied velocity gradient (with additional

stress conditions as necessary). For uniaxial tension a velocity gradient of 1 s^{-1} is applied in the z-direction while the stress in the x and y-directions is held to 0 MPa, for uniaxial compression a velocity gradient of -1 s^{-1} is applied in the z-direction while the stress in the x and y-directions is held to 0 MPa and for pure shear a velocity gradient of 1 s^{-1} is applied as a shear strain along the xz-plane (represented as simultaneous shears in the x-direction along the z-plane and in the z-direction along the x-plane). These rates are applied via an incremental time step of 0.0001 s for 200 increments; thus for example the case of uniaxial tension results in a total strain of 0.02 in the z-direction, equivalent to 2 % elongation. The material selected for the model is pure copper; thus the microstructure has a face-centered cubic (FCC) crystal structure and the plasticity equations are calculated over the 12 $\{111\}\langle 110\rangle$ slip systems. The hardening model used with these slip systems is the Voce hardening model shown in Chapter 3. To simulate the elastic response of a copper polycrystal, stiffness tensor constants were obtained from literature[10] and to simulate the plastic response, Voce hardening parameters are acquired by determining what values will result in a response from the model that fit a stress-strain curve that was experimentally measured during uniaxial tension of a pure copper polycrystal sample. The stiffness tensor and Voce hardening parameters used in the model are shown in Equations 5.1 and 5.2:

$$\boldsymbol{C} = \begin{bmatrix} 168.4 & 121.4 & 121.4 & 0.0 & 0.0 & 0.0 \\ 121.4 & 168.4 & 121.4 & 0.0 & 0.0 & 0.0 \\ 121.4 & 121.4 & 168.4 & 0.0 & 0.0 & 0.0 \\ 0.0 & 0.0 & 0.0 & 75.4 & 0.0 & 0.0 \\ 0.0 & 0.0 & 0.0 & 0.0 & 75.4 & 0.0 \\ 0.0 & 0.0 & 0.0 & 0.0 & 0.0 & 75.4 \end{bmatrix} \text{GPa} \tag{5.1}$$

$$\tau_0 = 45,\ \tau_1 = 30,\ \theta_0 = 800,\ \theta_1 = 130 \tag{5.2}$$

Once these properties and microstructure are entered into the model and the conditions are run to completion, the information that is output is the local Cauchy stress tensor, the local total strain tensor and the local orientation in Bunge Euler angles along with things that were constant throughout such as the grain identification numbers, all for each point of the microstructure grid. The results for von Mises equivalent stress and total von Mises equivalent strain for these three cases are displayed in Fig. 5-3 and 5-4 respectively. With the information given by the model, the local grain boundary surface tractions may be calculated and then thresholded for extreme values. The values that lie above the threshold are then analyzed for patters relating to other micromechanical values or microstructural features.

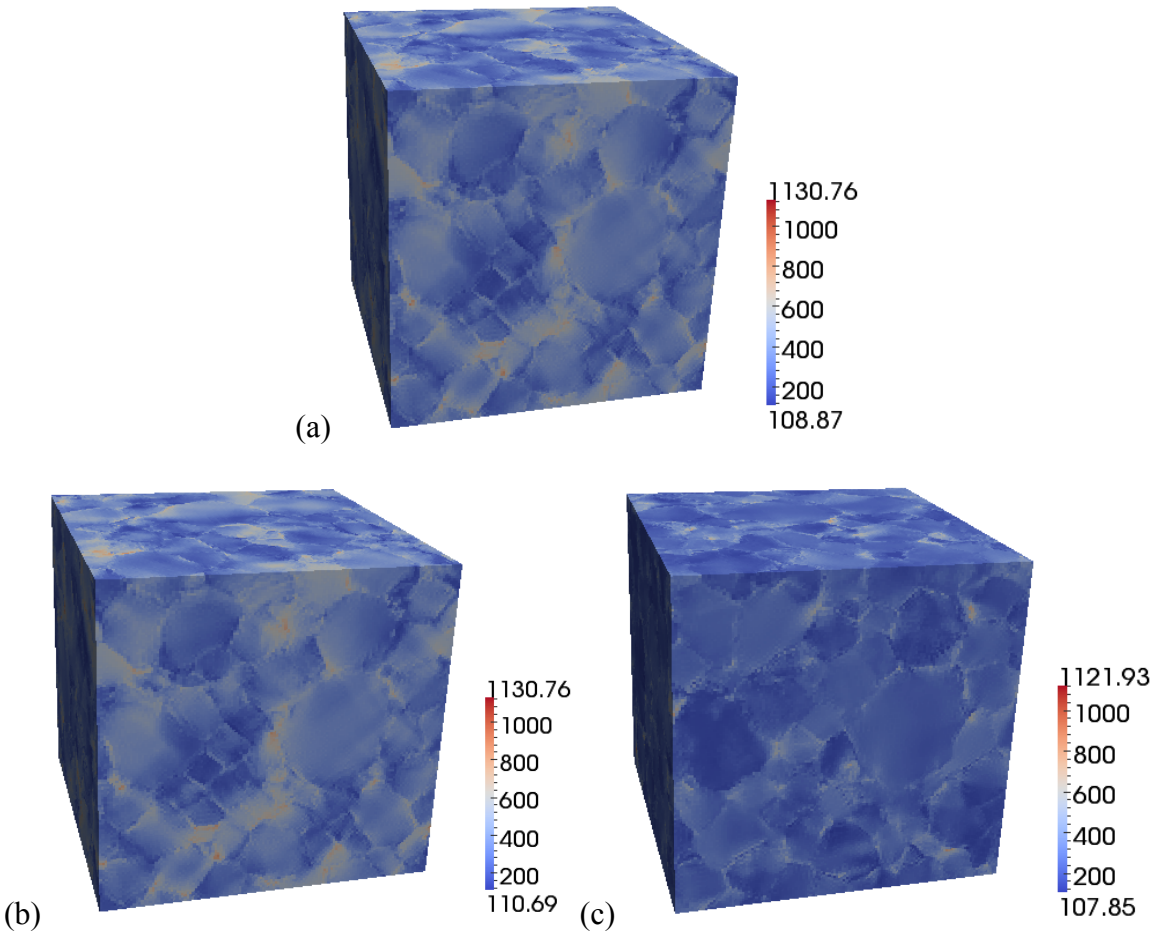

Figure 5-3. Coloring of the microstructure points by von Mises stress (MPa) for (a) uniaxial tension, (b) uniaxial compression and (c) pure shear.

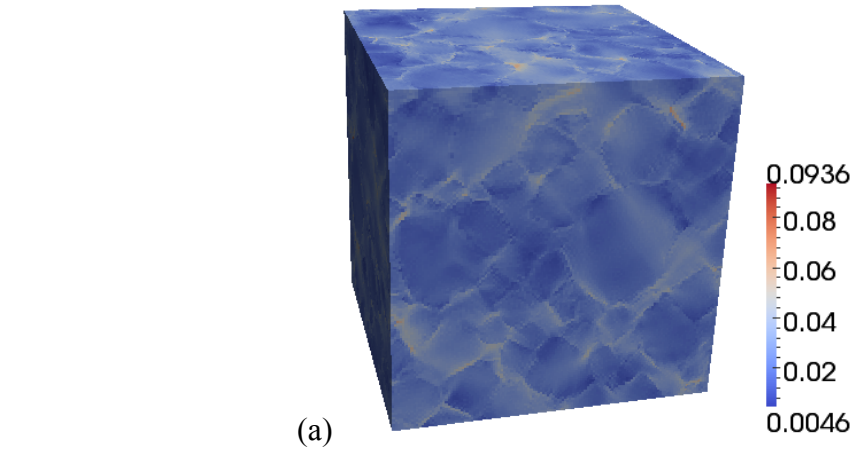

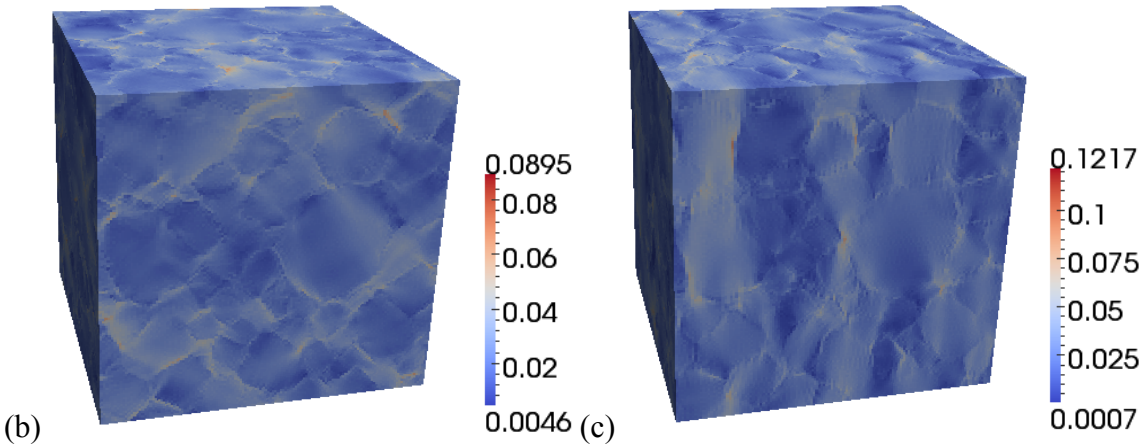

Figure 5-4. Coloring of the microstructure points by total von Mises strain (MPa) for (a) uniaxial tension, (b) uniaxial compression and (c) pure shear.

5.2: Traction Extreme Value Thresholding

The results are then run through a post-processing program to calculate the grain boundary surface normals as described in Chapter 4 and subsequently the grain boundary surface tractions. The calculation of a grain boundary surface traction and its two components follows the equations as shown

$$\vec{T}_i(x) = \sigma_{ij}(x)\hat{n}_j(x)$$
$$T^n(x) = \vec{T}(x) \cdot \hat{n}(x) \tag{5.3}$$
$$\vec{T}^s(x) = \vec{T}(x) - T^n(x)\hat{n}(x)$$

where σ_{ij}(x) is the local Cauchy stress tensor, $\hat{n}_{ij}$(x) is the local surface normal vector, T^n is the normal component of traction and T^s is the shear component of traction. A graphical representation of the relationship between these components is shown in Fig. 5-5. These values are calculated for each point that is considered a grain boundary point, which in this case will be points that have among their first nearest neighbors a point from a different grain. The normal component of traction and the magnitude of the shear component of traction vector are shown on the grain boundary points in Fig. 5-6 and 5-7. The specific coloring scale chosen for Fig. 5-6 highlights the dichotomy of the normal component of traction results between positive and negative values, which give indication of the direction of the traction. Similarly, note that the scalar display of the shear component of traction vector in Fig. 5-7 does not indicate the direction of the traction.

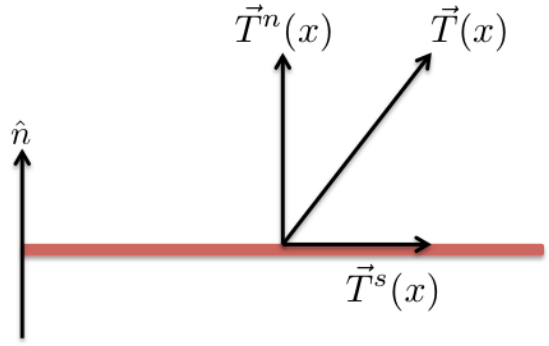

Figure 5-5. Demonstration of the relationship between the general traction vector and the normal and shear components of traction.

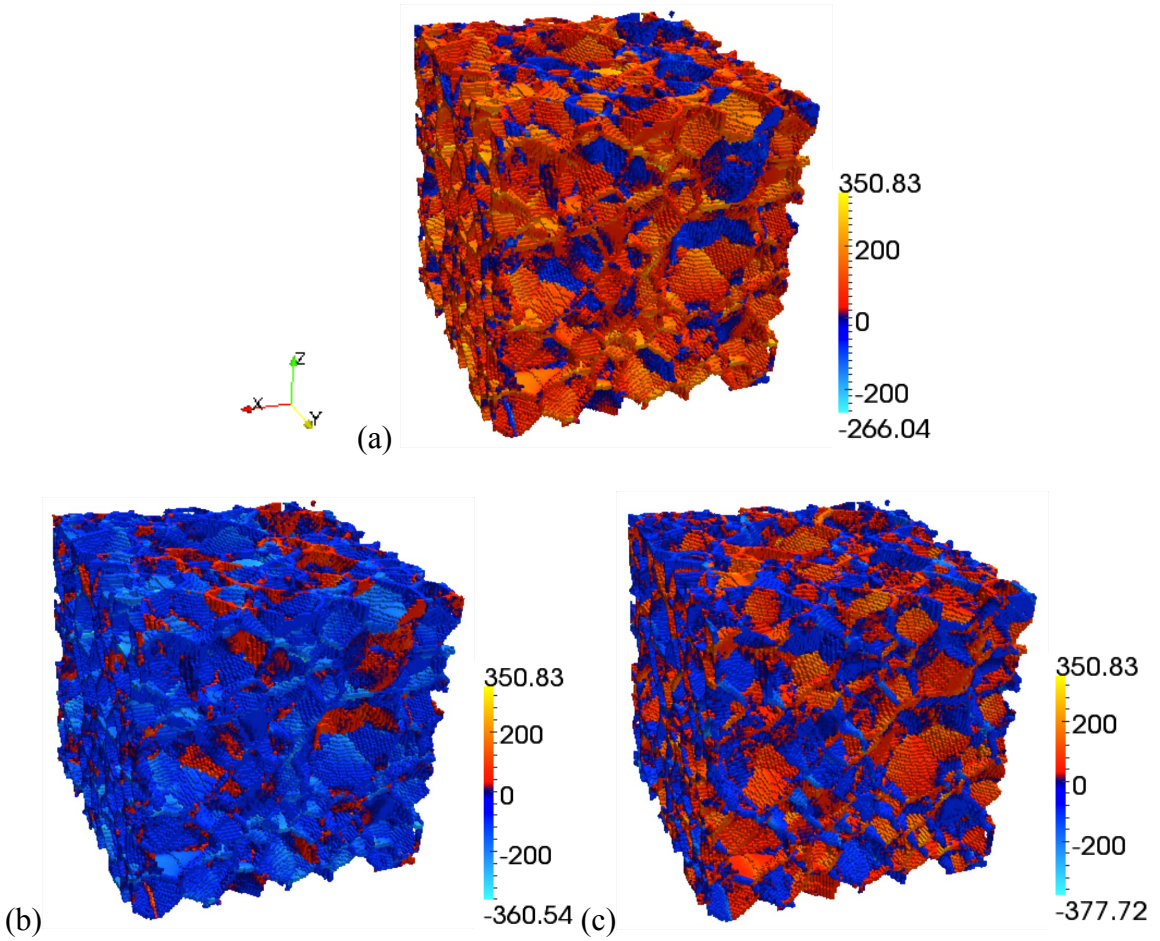

Figure 5-6. Coloring of the grain boundary points by the normal component of traction (MPa) for (a) uniaxial tension, (b) uniaxial compression and (c) pure shear.

Our interest is in determining which value of grain boundary surface traction components can be considered "extreme values". To do this, we use a method developed by Donegan *et al.*[106] to determine a threshold value the points above which will be considered extreme values. This method involves an analysis of the data that exceeds a

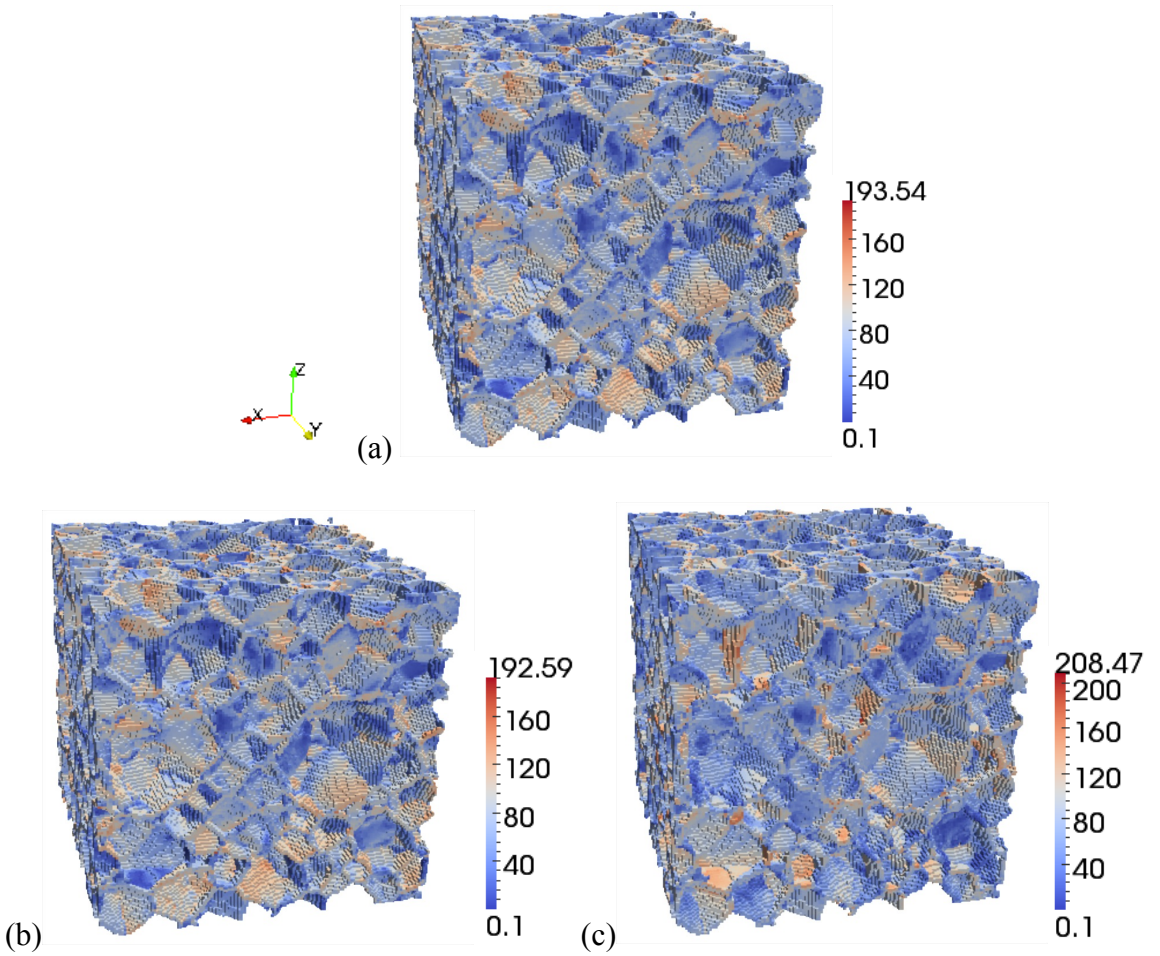

Figure 5-7. Coloring of the grain boundary points by the shear component of traction (MPa) for (a) uniaxial tension, (b) uniaxial compression and (c) pure shear.

chosen threshold and is known as the peaks-over-threshold approach, with the key point being that if an appropriate threshold was selected then the data above the threshold converge to the generalized Pareto distribution. The generalized Pareto distribution is a probability distribution family that is described by three parameters: scale (σ), shape(ξ) and location (μ). In this case the location parameter is analogous to the threshold. Donegan showed that if the points above a chosen threshold really do converge to the generalized Pareto distribution then an increase in the location parameter/threshold should not cause a change in the shape or scale parameters[106].

A threshold choice plot can be used to check this for a given set of data by plotting the shape and scale parameters against varying threshold choices, thus reasonable threshold choices can be found in regions of the plot which show relatively constant trends. Another plot that can be used to identify thresholds is the mean residual life plot, which tracks the average excess of values above the threshold value. When the mean residual life plot has a linear trend, the points above threshold converge to the generalized Pareto distribution. Thus the general method for determining a threshold is to generate both sets of plots for a given dataset and identify a threshold that is in both a constant region of the threshold choice plots and a linear region of the mean residual life plot. Donegan *et al.* also noted that the Pickands-Balkema-de Haan theorem indicates that data above a threshold converges to the generalized Pareto distribution as the threshold approaches the right end of the overall distribution. Thus for the case where multiple thresholds could satisfy the already stated criterion, the largest threshold should be selected. An example of the use of these plots for threshold selection in this work is shown in Fig. 5-8 for the case of uniaxial tension. We use this technique to determine extreme value thresholds for both the normal and shear components of traction. For the normal component of traction the positive extreme value thresholds found are 225 MPa for the case of uniaxial tension, 90 MPa for the case of uniaxial compression and 175 MPa for the case of pure shear. For the magnitude of the shear component of traction vector the extreme value thresholds found are 140 MPa for the case of uniaxial tension, 140 MPa for the case of uniaxial compression and 150 MPa for the case of pure shear.

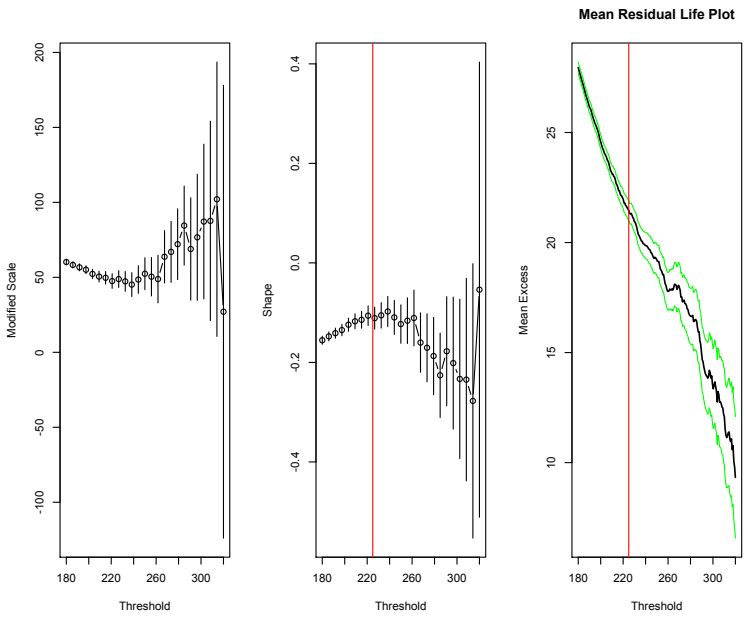

Figure 5-8. Threshold choice plots and mean residual life plot for the tail of the normal component of traction distribution for uniaxial tension; red line indicates threshold choice.

5.3: Results of Hot Spot Analysis

With this information we identify the set of points that constitute extreme values and collect various parameters on these points, which from here on will be labeled 'hot spot' points. The parameters of interest are the von Mises equivalent stress, the von Mises equivalent strain, the hydrostatic stress, the local crystal orientation and the angle between the grain boundary surface normal and the sample directions. The von Mises equivalent stress and strain are represented by the equations shown

$$\sigma_{VM} = \sqrt{\frac{3}{2}\sigma' : \sigma'} \tag{5.4}$$

$$\varepsilon_{VM} = \sqrt{\frac{2}{3}\varepsilon' : \varepsilon'} \tag{5.5}$$

where σ' and ε' are the deviatoric stress and strain tensors. The hydrostatic stress is the average of the trace of the Cauchy stress tensor represented by the equation $p=(1/3)\Sigma\sigma_{ii}$.

Plots of these three factors against the normal and shear component of traction hotspot points are shown in Fig. 5-9 for normal component hot spots under uniaxial tension, Fig. 5-10 for shear component hot spots under uniaxial tension, Fig. 5-11 for normal component hot spots under uniaxial compression, Fig. 5-12 for shear component hot spots under uniaxial compression, Fig. 5-13 for normal component hot spots under pure shear and Fig. 5-14 for shear component hot spots under pure shear. The angle from the grain boundary surface normal to the three principal sample directions is calculated via dot product of the normal vector with the sample direction vectors. The sample directions are designated as the normal direction (ND) for the *z*-axis, the rolling direction (RD) for the *x*-axis and the transverse direction (TD) for the *y*-axis. Distribution plots of the angle from surface normal to the normal direction (which is also the loading direction) for normal component and shear component hot spots for the case of uniaxial tension are shown in Fig. 5-15. The same information for the case of uniaxial compression is shown in Fig. 5-16. For the case of pure shear loading conditions, measuring the angle to a single direction is insufficient due to the unique nature of the loading conditions. Thus distribution plots of the angle from the surface normal to all three sample directions are shown in Fig. 5-17 for the normal component hot spots and in Fig. 5-18 for the shear component hot spots.

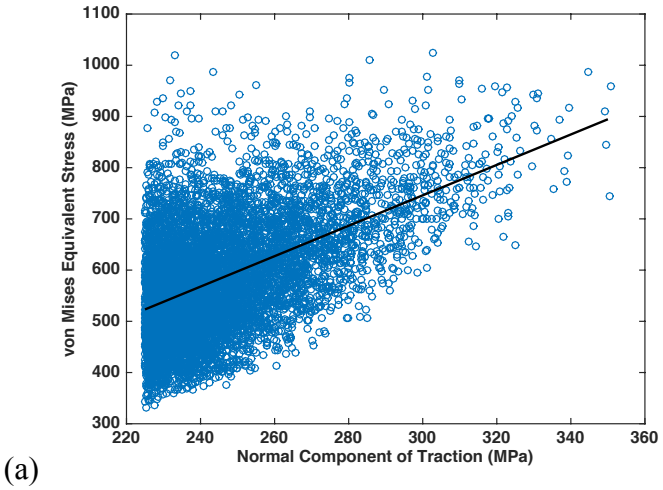

(a)

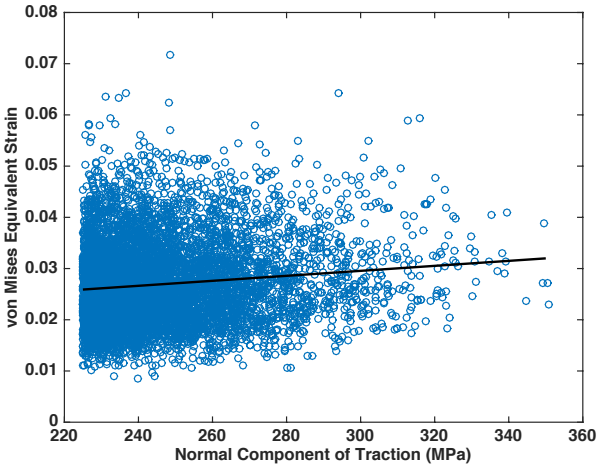

(b)

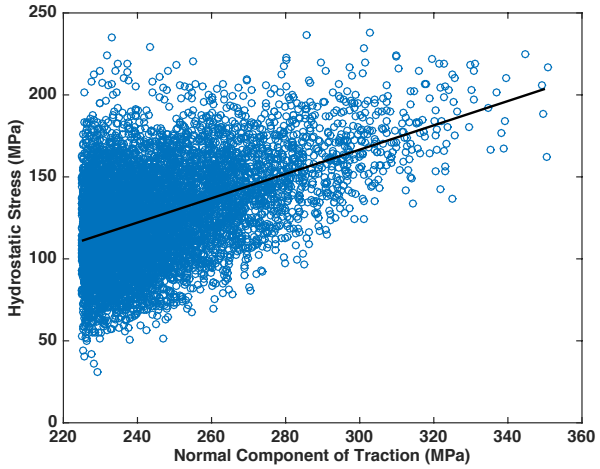

(c)

Figure 5-9. Plots and trend lines of (a) von Mises stress and (b) strain as well as (c) hydrostatic stress for the normal component hot spots under uniaxial tension.

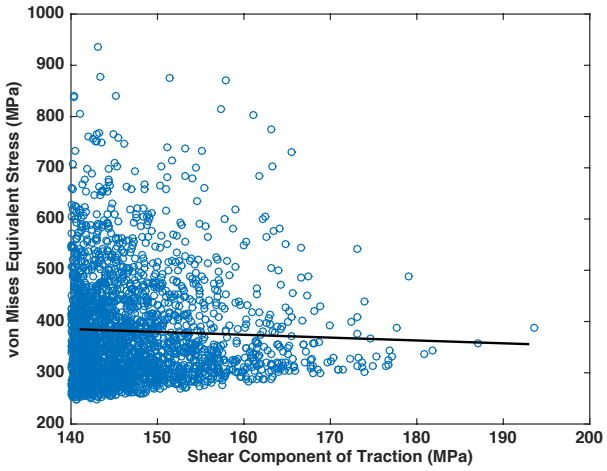

(a)

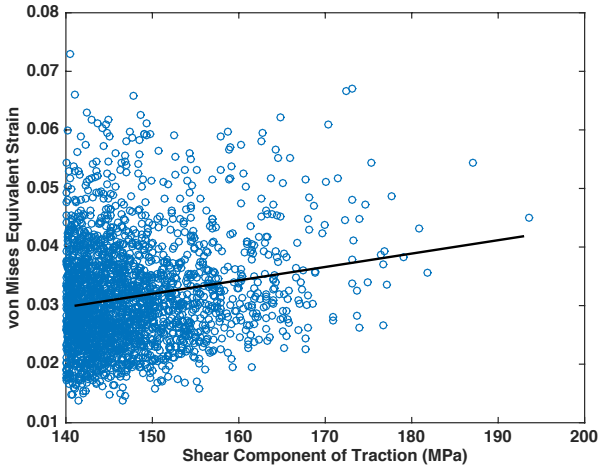

(b)

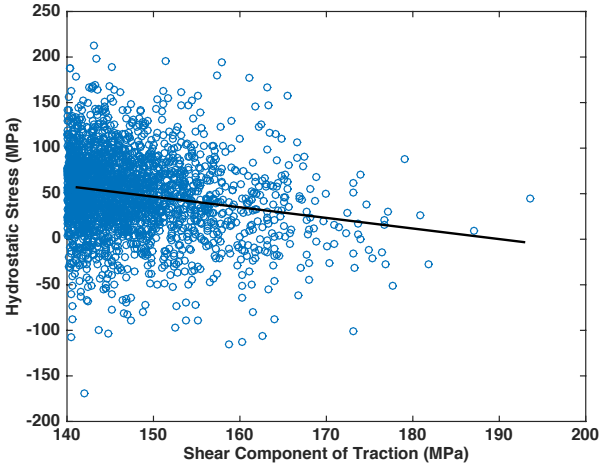

(c)

Figure 5-10. Plots and trend lines of (a) von Mises stress and (b) strain as well as (c) hydrostatic stress for the shear component hot spots under uniaxial tension.

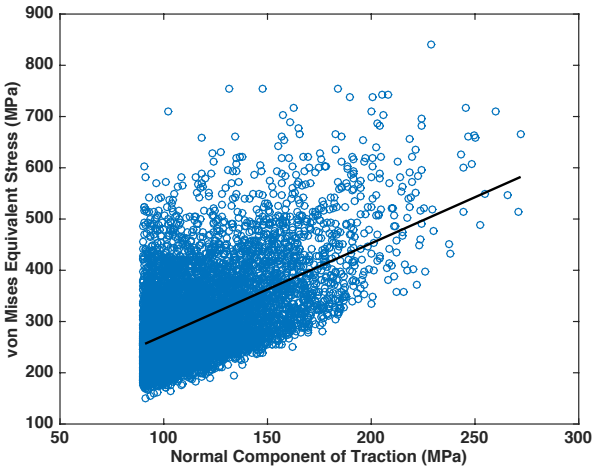

(a)

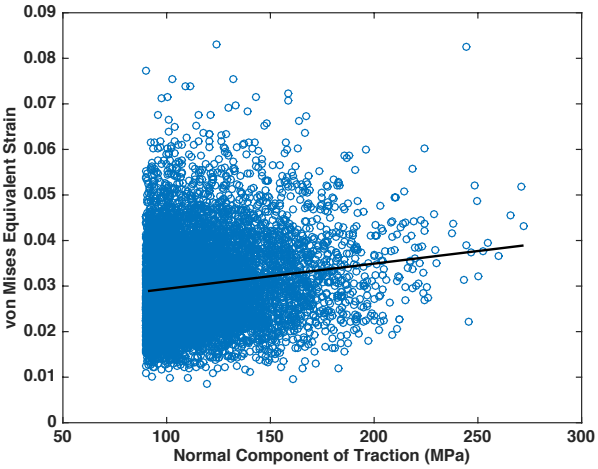

(b)

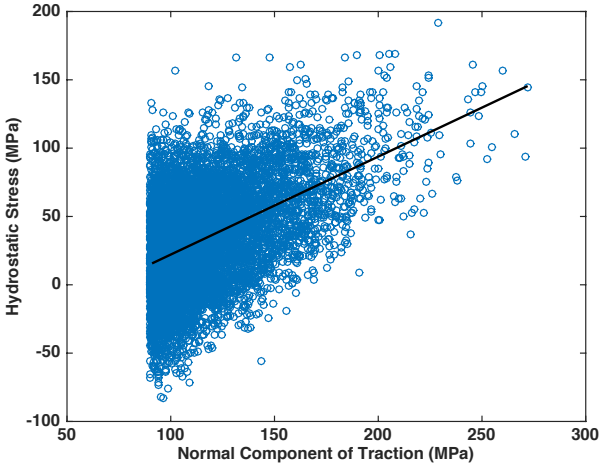

(c)

Figure 5-11. Plots and trend lines of (a) von Mises stress and (b) strain as well as (c) hydrostatic stress for the normal component hot spots under uniaxial compression.

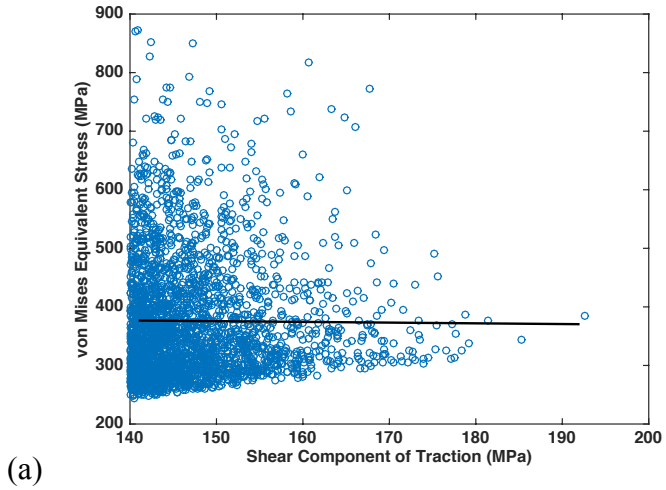

(a)

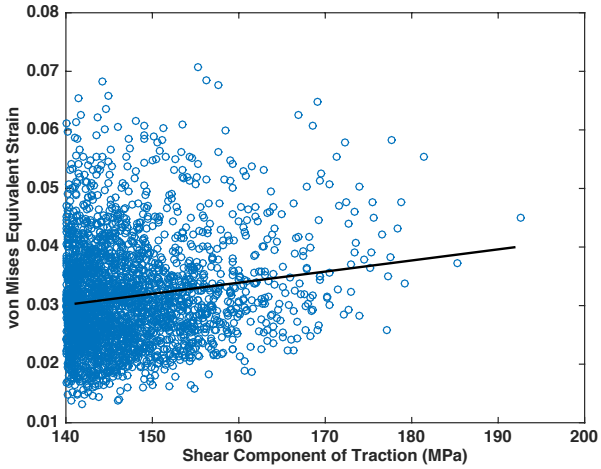

(b)

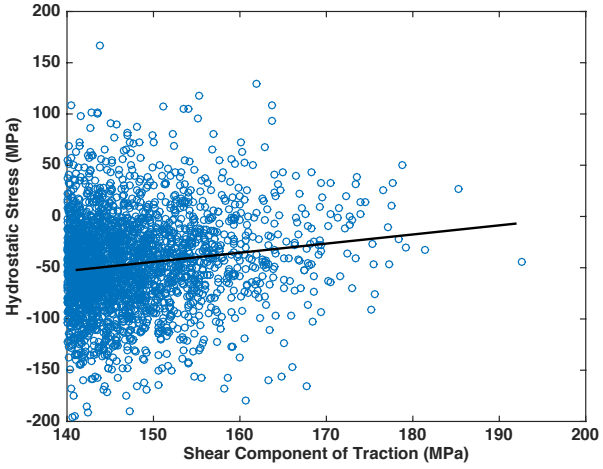

(c)

Figure 5-12. Plots and trend lines of (a) von Mises stress and (b) strain as well as (c) hydrostatic stress for the shear component hot spots under uniaxial compression.

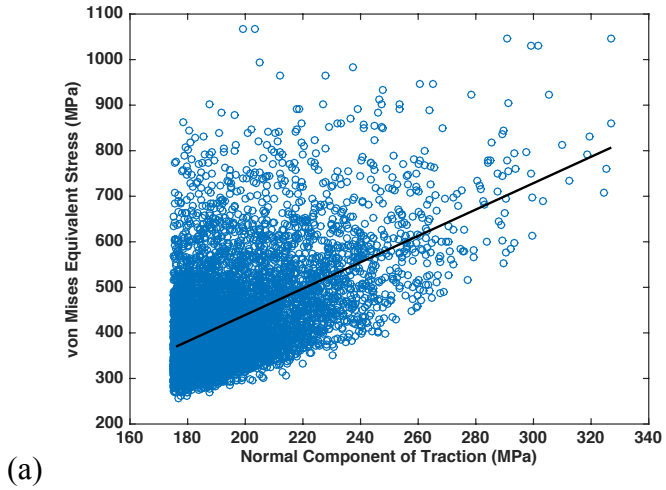

(a)

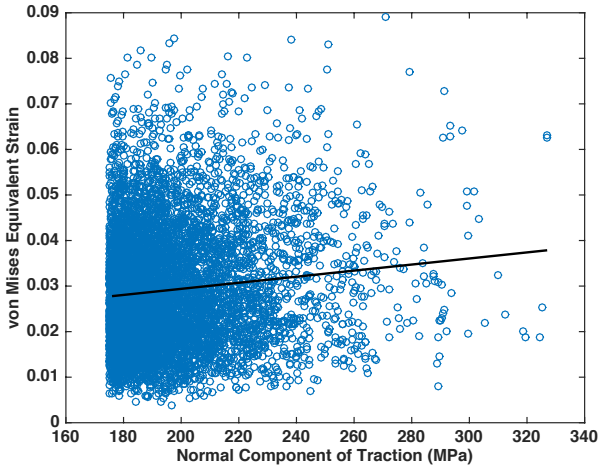

(b)

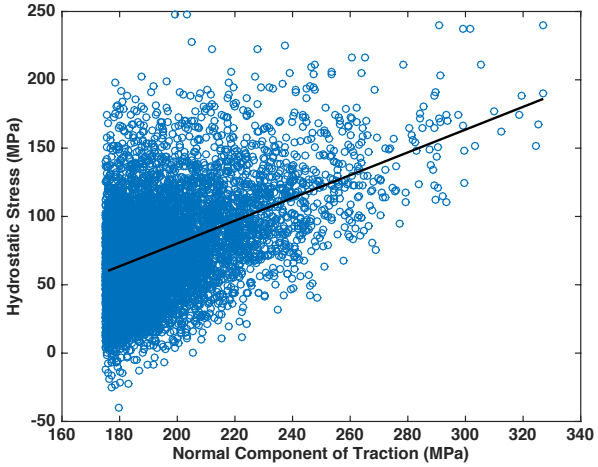

(c)

Figure 5-13. Plots and trend lines of (a) von Mises stress and (b) strain as well as (c) hydrostatic stress for the normal component hot spots under pure shear.

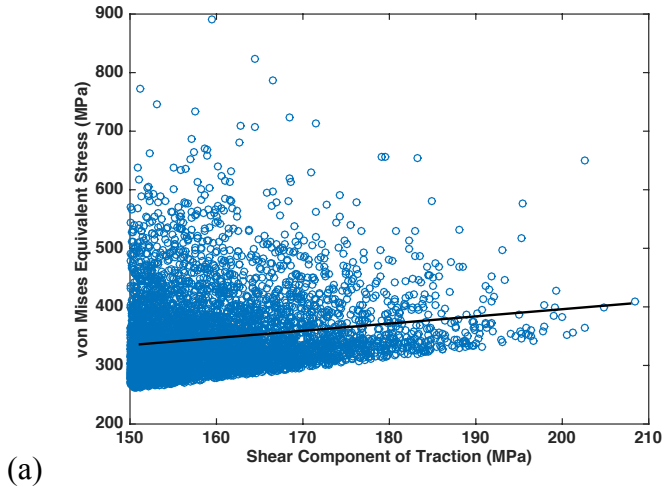

(a)

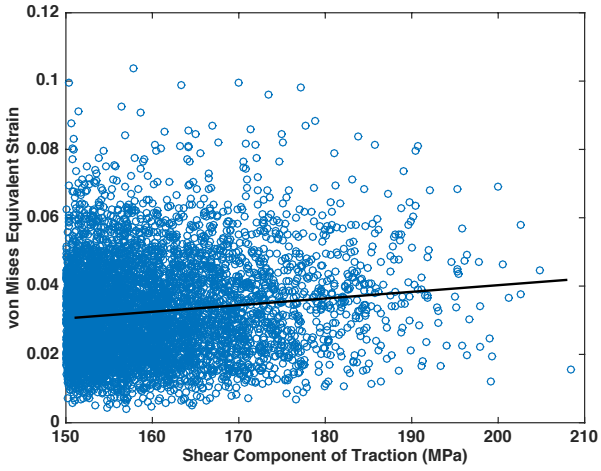

(b)

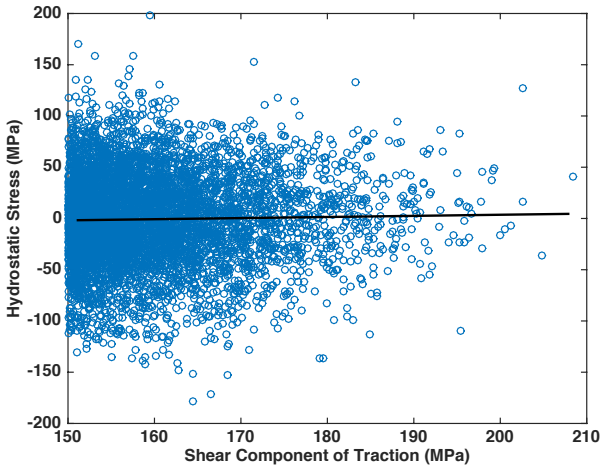

(c)

Figure 5-14. Plots and trend lines of (a) von Mises stress and (b) strain as well as (c) hydrostatic stress for the shear component hot spots under pure shear.

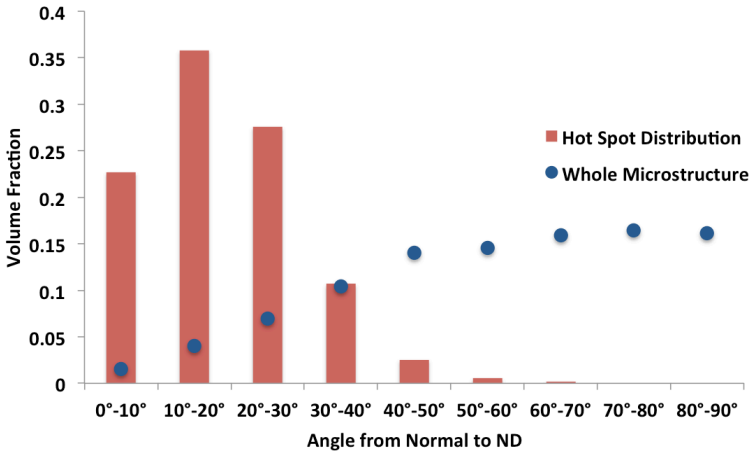

(a)

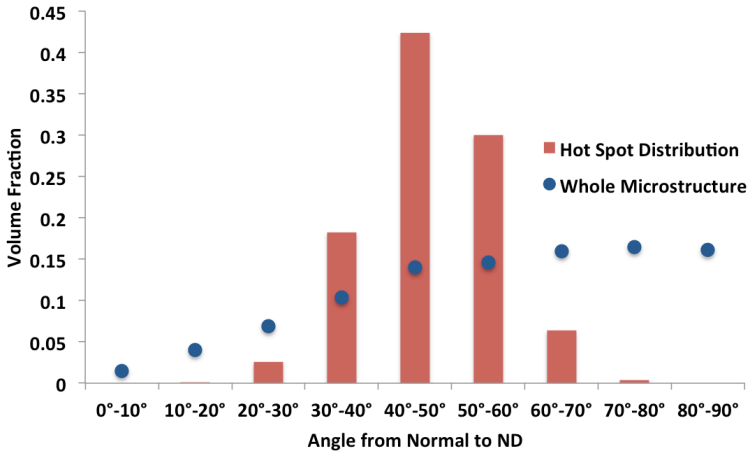

(b)

Figure 5-15. Distribution plots of the angle to normal direction for the (a) normal and (b) shear component hot spots under uniaxial tension along with the plot of the angle from all surface normals to the normal direction.

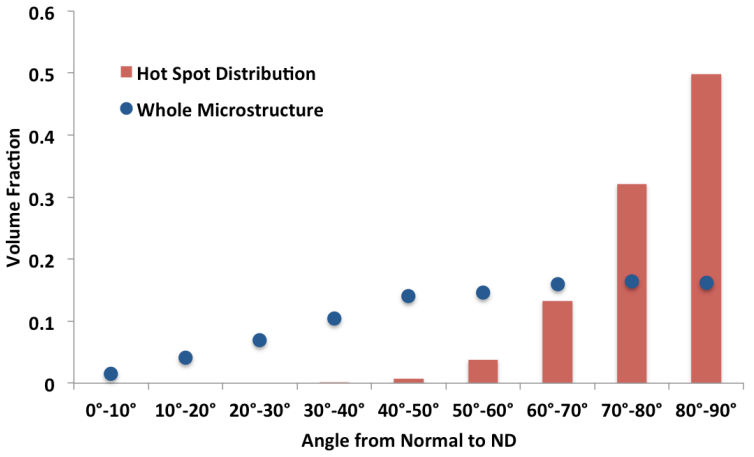

(a)

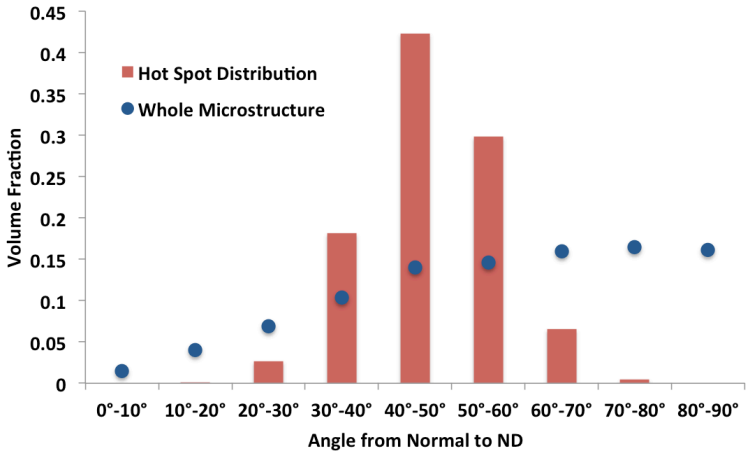

(b)

Figure 5-16. Distribution plots of the angle to normal direction for the (a) normal and (b) shear component hot spots under uniaxial compression.

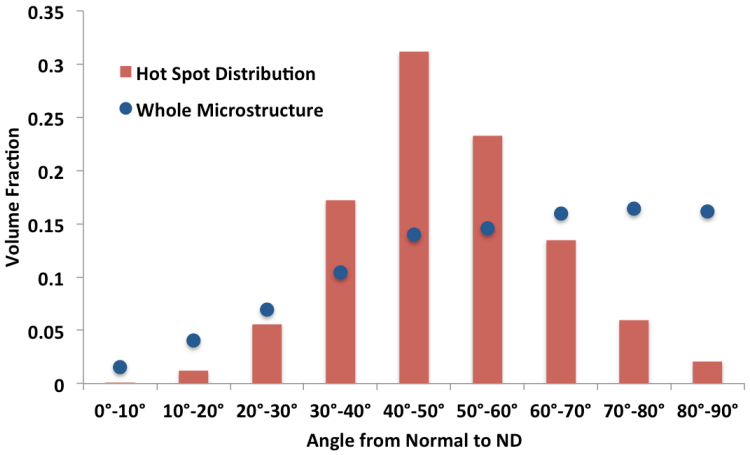

(a)

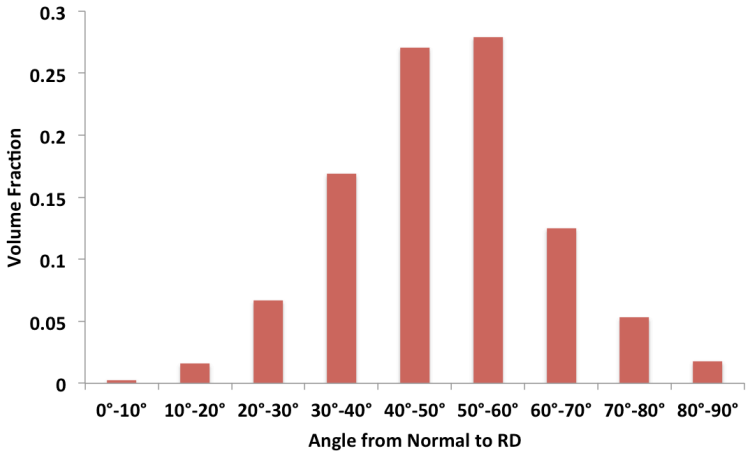

(b)

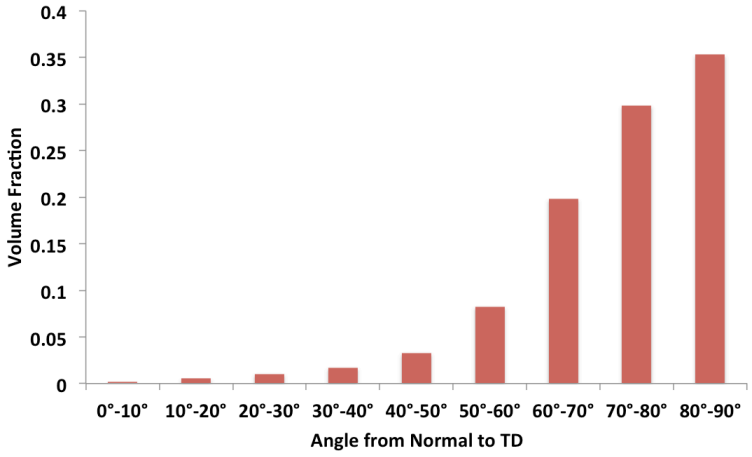

(c)

Figure 5-17. Distribution plots of the angle from the surface normals of normal component hot spots under pure shear to the (a) normal direction (*z*-axis), (b) rolling direction (*x*-axis) and (c) transverse direction (*y*-axis).

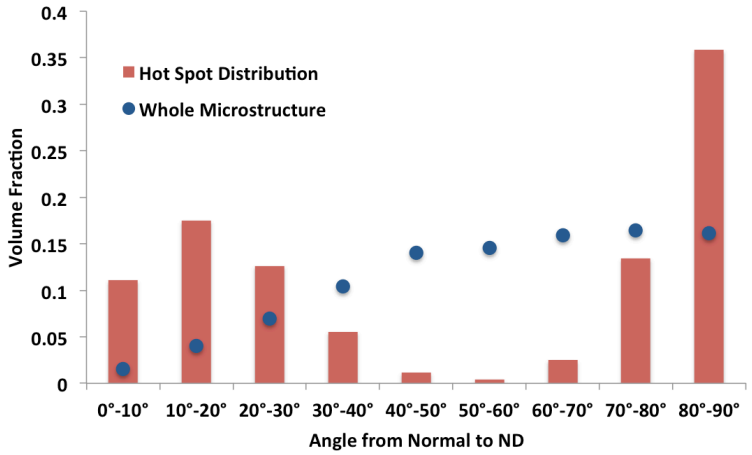

(a)

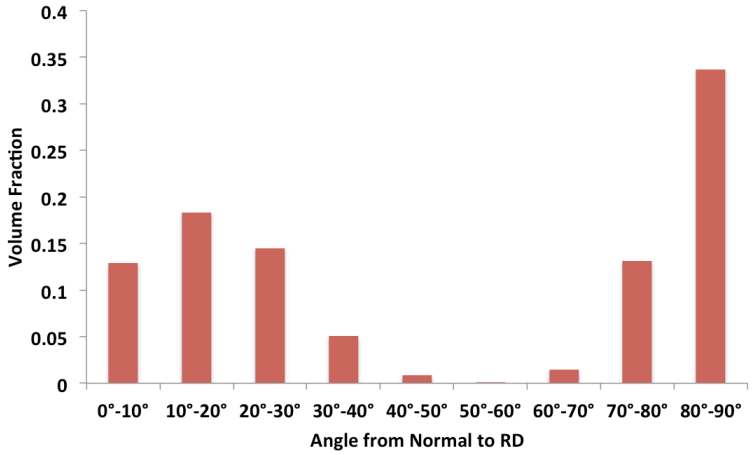

(b)

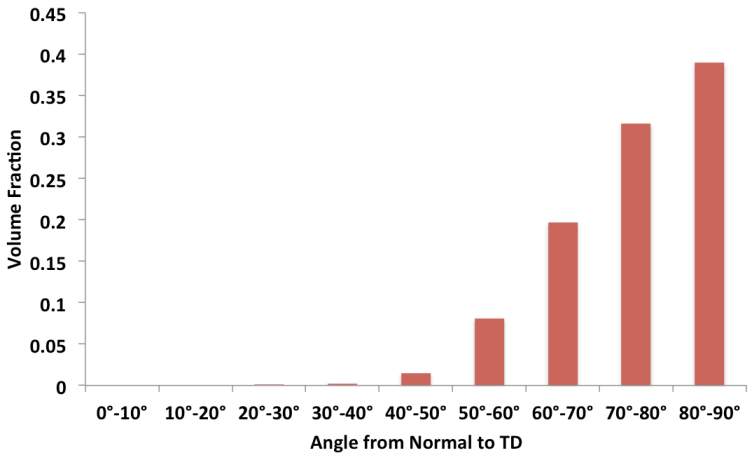

(c)

Figure 5-18. Distribution plots of the angle from the surface normals of shear component hot spots under pure shear to the (a) normal direction (*z*-axis), (b) rolling direction (*x*-axis) and (c) transverse direction (*y*-axis).

Applying these thresholds to this microstructure results in a possibly limited dataset where the resulting points make up less than 2 % of the total set of grain boundary points and come from a limited number of boundaries in the given microstructure. To ensure that the data being considered is statistically significant, particularly for comparison with experimental results that contain many more grains than this test microstructure, a greater number of microstructures are run through the model under uniaxial tension loading conditions. The same grain structure as that shown in Fig. 4-7 is used in all the cases to maintain the same morphology while the orientations assigned to each grain are randomly reassigned; this process is used nine times for a total of ten microstructures. Distribution plots of the angles from normal vector to the normal direction from all ten microstructures are shown in Fig. 5-19 for both normal and shear component hot spots. We use the orientations from the grain boundary points that constitute the hot spots from all ten microstructures to generate inverse pole figures relative to the loading axis; these are shown in Fig. 5-20. Similarly, we use the orientations on both sides of the grain boundaries that constitute the hot spots from all ten microstructures to generate

misorientation angle distributions, which are shown in Fig. 5-21 for normal and shear component hot spots.

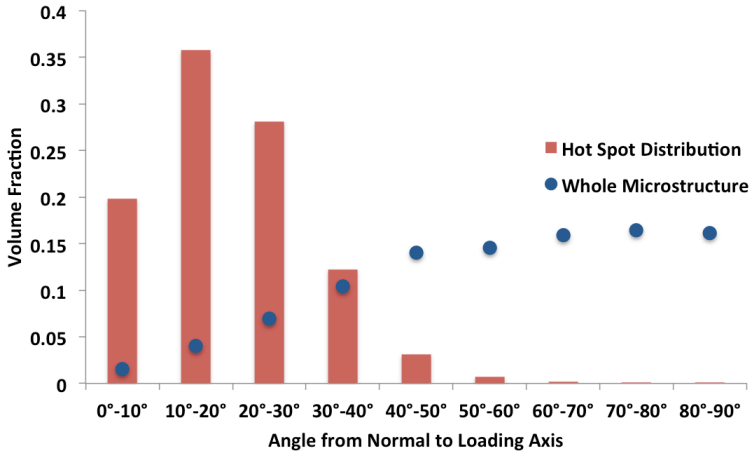

(a)

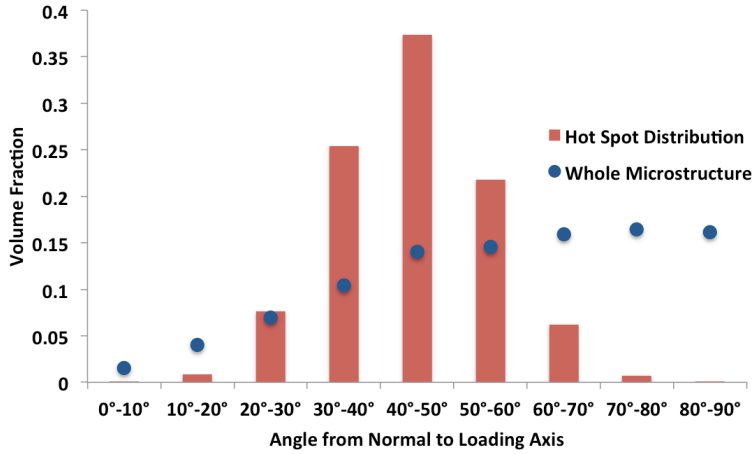

(b)

Figure 5-19. Distribution plots of the angle to normal direction for the (a) normal and (b) shear component hot spots from all ten microstructures, all under uniaxial tension.

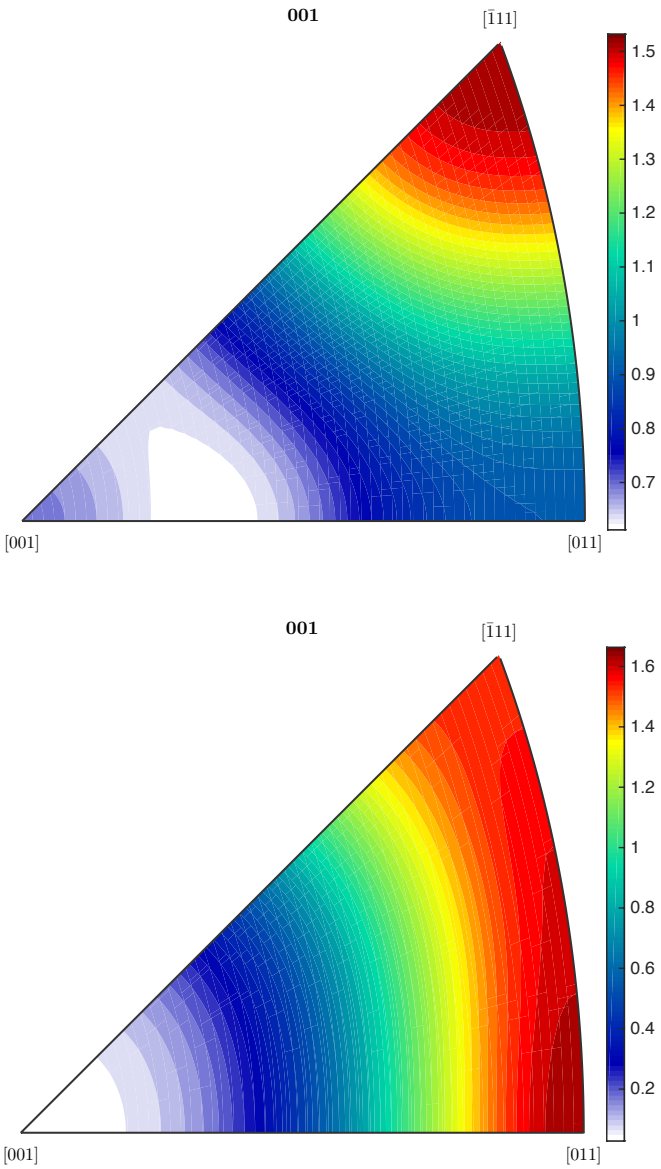

Figure 5-20. Inverse pole figures from the crystal orientations of the normal (top) and shear (bottom) component hot spots from all ten microstructures, all under uniaxial tension.

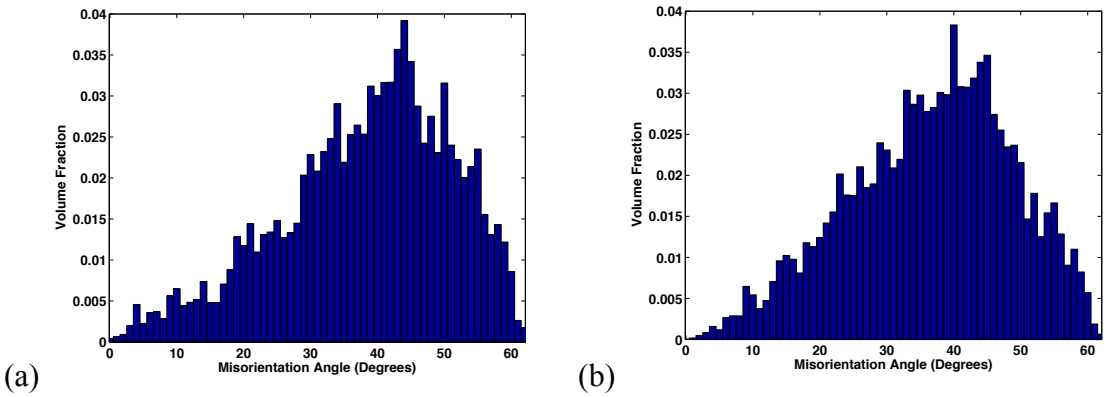

(a) (b)

Figure 5-21. Misorientation angle distribution from the grain boundary points that make up the (a) normal and (b) shear component hot spots from all ten microstructures, all under uniaxial tension.

5.4: Discussion

Considering just the normal component hot spots under all three loading conditions as shown in Fig. 5-9, 5-11 and 5-13 (parts a and c), there appears to be a general positive trend between the normal component of traction and both the von Mises stress and the hydrostatic stress but it is not a particularly strong correlation. The important thing to take from this result is that both factors taken from the stress tensor show a trend here, indicating that both do contribute to the normal component of stress. By contrast, the shear component hot spots under all three loading conditions do not trend with hydrostatic stress, despite using the full stress tensor, but actually seem to trend more strongly with von Mises stress than the normal components do. This indicates that the normal component hot spots have some relationship with hydrostatic stress, which represents a dilatational stress effect. Such an effect is related to void growth and possibly void nucleation; it is this sort of relationship that is investigated further in the experiment on the shocked copper. Similarly, while we note the relationship between the shear component hot spots and von Mises equivalent stress, an experimental comparison

has not yet been identified. Neither the normal component hot spots nor the shear component hot spots show any sort of trend with von Mises equivalent strain. Work by Rollett *et al.*[107] has found that von Mises stress hot spots in a pure viscoplastic FFT model tend to be associated with grain boundaries, reinforcing the connection seen here.

The first observation to make about the spatial trends for the normal component of traction is that it has a duality in its result. We interpret a positive normal component of traction as being a tensile load on the interface while a negative normal component is a compressive load on the interface. When we look at the results in Fig. 5-6, it shows that the normal component values have a range that extends from positive to negative and in particular that individual grain boundaries appear to be either fully positive or fully negative. Looking between the different loading cases, there are trends in the inclination of the boundaries with respect to the stress system in terms of tensile versus compressive loads. The largest positive normal components appear to be on boundaries that are perpendicular to loading axis in the case of applied uniaxial tension while for the case of uniaxial compression it appears that the only positive normal components are on boundaries that are parallel to the loading direction. The case of pure shear loading conditions does appear to have a trend for positive and negative normal components, one that likely conforms to some sort of 45˚ angle trend similar to shear banding. The main contrast is that some of the boundaries following that trend are positive while some are negative; it is apparent that the boundaries that are aligned roughly perpendicular to the (+x, +z) axis have positive normal components while those aligned roughly perpendicular to the (+x, -z) axis have negative normal components as seen in Fig. 5-6c. The shear component of traction magnitude shows trends that are to first order the inverse of those

shown for the normal component. For the cases of uniaxial tension and compression (which show strong similarity to each other) the larger shear components appear to avoid boundaries that are perpendicular to the sample axes while for the case of pure shear loading conditions it is on these same boundaries that the largest shear components are concentrated.

The measurements of the angles from the boundary normal can quantify these observations. From the normal component hot spot angles for applied uniaxial tension shown in Fig. 5-15a, we see that there is a strong preference for smaller angles, with a maximum from 10˚ to 20˚, which equates with highly loaded boundaries that are closer to perpendicular to the loading direction. By contrast, the same measurement shown in Fig. 5-16a for applied uniaxial compression shows a strong preference for larger angles, with a maximum from 80˚ to 90˚, which equates with preferring boundaries that are close to parallel with the loading direction. The interesting thing is that while in the case of uniaxial compression the normal component hot spots cluster at one extreme of the angle range, while in the case of uniaxial tension they do not appear to be exactly perpendicular. The explanation is the differences in the overall distribution of angles to the normal direction, which are predominantly at higher angles, an expected phenomenon in a three dimensional case. To understand this expectation, consider a discrete point sphere with any arbitrary axis drawn through it; there will be more points for the circumference of the sphere at the 'equator' than at the 'poles' relative to this axis. Thus, for the uniaxial tension normal component hot spots there are more results in the 10˚-20˚ bin than the 0˚-10˚ bin because overall there are more boundary points that fall in to those bins (as seen in Fig. 5-15a), while for the uniaxial compression normal component hot

spots the range of bins over which the points are dominant are together relatively constant on the overall distribution (as seen in Fig. 5-16a). The normal component hot spots are in very different places for the case of pure shear loading conditions; from Fig. 5-17 we see that the hot spots prefer to be on boundaries that are perpendicular to the xz-plane due to the predominance of large angles relative to the transverse direction. Within the xz-plane the hot spots concentrate on boundaries that are located around 40˚-50˚ to the normal and rolling directions; however this can be deceiving since while all the hot spots are on boundaries that are around that angle range, not all boundaries around that angle range have the possibility of being hot spots due to the arrangement of positive and negative normal component boundaries as mentioned in the previous paragraph.

The differences between loading conditions for boundaries preferred by normal component hot spots follow trends that are also seen in experiments. Gurland subjected spheroidized 1.05% C steel cylindrical samples to both uniaxial tension loading and torsion loading and measured the angle of cracks in cementite particles and measured the angle from the crack traces to the long axis of the sample[17]. What he found was that the crack traces that formed under uniaxial tension tended to be oriented 90˚ to the long axis and under torsion tended to be oriented 45˚ to the long axis as shown in Fig. 5-22.

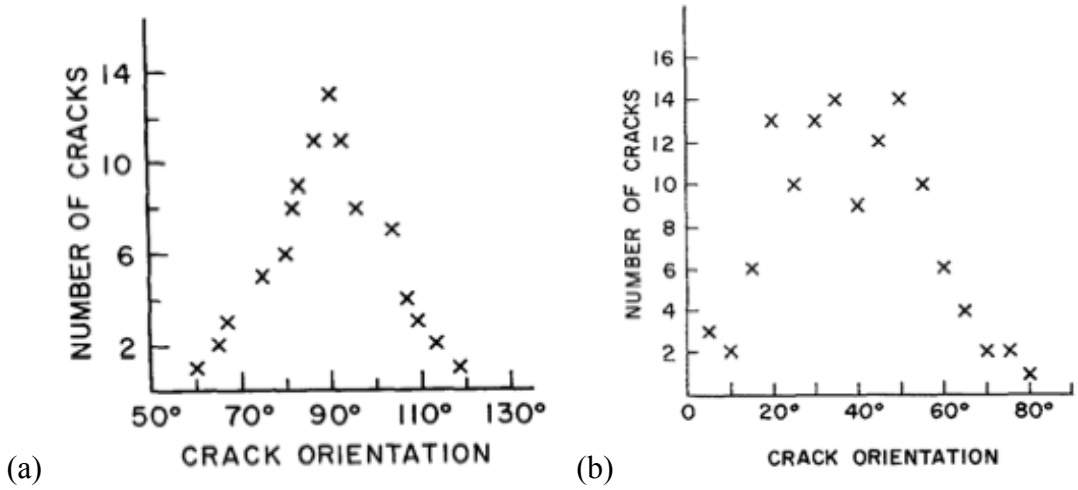

Figure 5-22. Plot of the angle from crack trace to the cylinder long axis for (a) uniaxial tension loading and (b) torsion loading; taken from Gurland[17].

Recall from Fig. 2-2 that the situation of particle cracking involves crack traces that are perpendicular to the long axis of the particle and parallel to the voids that form due to interface decohesion. The concept of the crack trace being at 90˚ to the loading axis means that the crack plane is perpendicular to the loading axis and thus that plane normal would be 0˚. In general, what Gurson and this work observe is that many potential damage planes tend to be oriented perpendicular to the direction of principal tensile loading axes; applied shear is equivalent to a tensile load on the body at 45˚ to the plane the shear is applied on.

The shear component hot spots for the cases of both uniaxial tension and compression show a preference for boundaries inclined around 40˚-50˚ to the loading axis as shown in Fig. 5-15b and 5-16b. While the effect of the overall angle distribution might affect the bin heights around the peak, the location of the peak at the 40˚-50˚ bin will not change. The shear component hot spots for the case of pure shear loading again appear to be primarily on boundaries that are parallel to the transverse direction as revealed by Fig. 5-

18c. Within the xz-plane, Fig. 4-18 shows that the shear component hot spots under pure shear prefer boundaries that are perpendicular to either the normal or rolling directions. We see again that the 10˚-20˚ bin has a higher value than the 0˚-10˚ bin for the same reason as before with the normal component hot spots.

When looking at the grain orientations around boundaries from Fig. 5-20, normal component hot spots show an increased tendency for those grains to have their <111> crystal direction orientated parallel to the loading direction; the shear component hot spots instead tend to favor the <101> crystal direction though there is a presence of directions all along the <101>-<111> symmetry line. The differences between Fig. 5-20 and Fig. 5-2 show that the textures seen where normal and shear traction hot spots occur is different than the texture of the overall microstructure. The misorientation angle distribution shown in Fig. 5-21 fits very closely the misorientation angle distribution expected for a cubic polycrystal with randomly oriented grains, which is known as the Mackenzie curve[108]. Being close to fitting the Mackenzie curve is another indicator that perhaps the crystallographic nature of the grain boundary itself might not be as significant in determining void nucleation.

Though the determination of the hot spot thresholds does not relate to any physical phenomena, we aim to analyze the connection between large traction concentrations and damage by limiting the comparisons to only those statistically extreme values. The principal analysis of these results is comparing the measurements from the normal component hot spots to similar measurements made in an experiment by Fensin *et al.*[34] on the shock loading of copper polycrystals. In their work, the samples were oxygen-free, high-conductivity polycrystalline copper which was fully annealed and was subjected

shock loading by being struck by quartz flyer plates with a velocity of 130 m/s, leading to a peak tensile stress within the microstructure estimated to be 1.3 GPa. Cross-sectional EBSD images of the deformed/damaged samples were taken and the angle from the shock direction to the grain boundary trace from all boundaries was measured; one of the EBSD images as well as an example of measuring the angle is shown in Fig. 5-23. The rules of stereology were used to allow the two-dimensional EBSD images to be able to appropriately analyze the grain boundaries, which are three-dimensional features. Stereology accomplishes this by using a sufficiently large number of randomly oriented two-dimensional slices of a three-dimensional material.

The distribution of the angles measured from all boundaries and just from those that nucleated voids is shown in Fig. 5-24a. To perform this comparison, we use the data obtained from the ten generated microstructures so that we have a larger normal component hot spots since there is a large number of voided boundaries in the actual sample. We ran these microstructures under uniaxial tension because it is an approximation of the type of strain mode experienced by shock loading conditions.

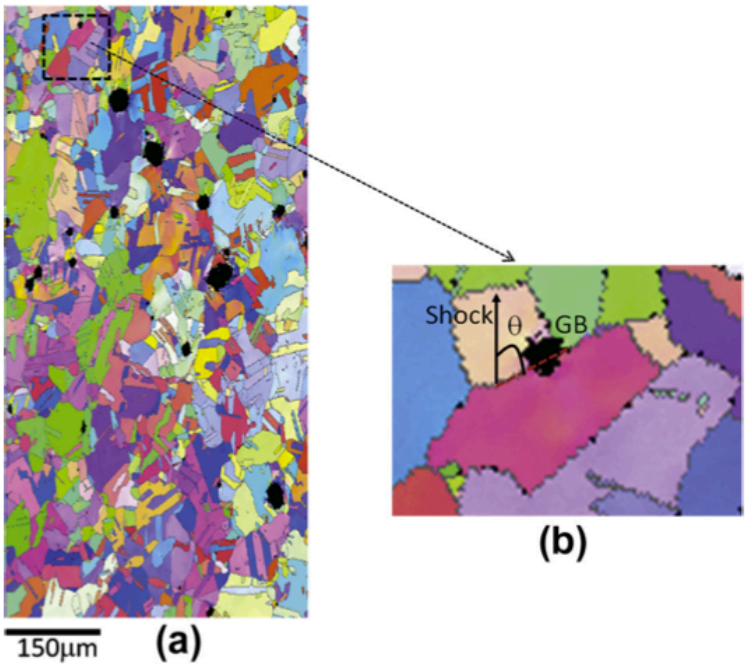

Figure 5-23. EBSD image of the cross-section of a copper polycrystal sample after shock loading (a) and a magnified image showing how the grain boundary trace angle is measured (b); taken from Fensin *et al.*[34]

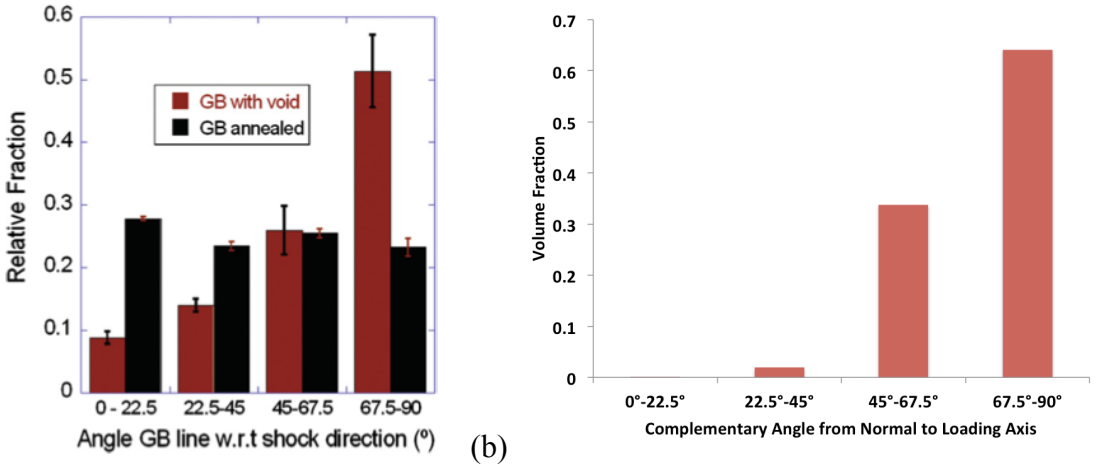

Figure 5-24. Plot of the angle distribution of (a) voided grain boundary traces (taken from Fensin *et al*[34]) and of (b) normal component hot spot boundary traces.

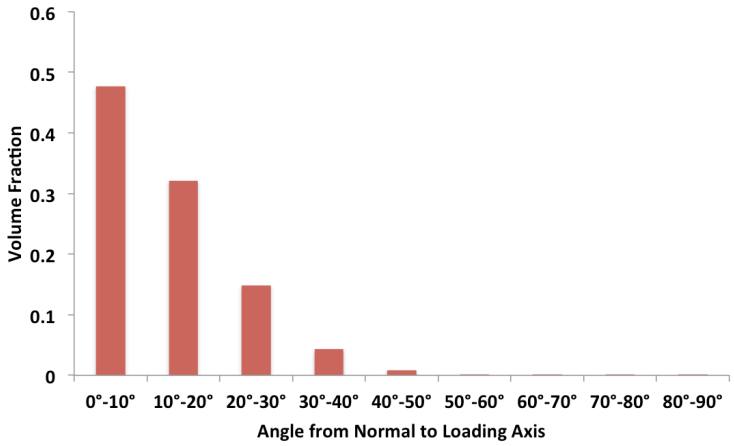

Figure 5-25. Distribution plot of the angle from the normal to loading axis for normal component hot spots under uniaxial tension normalized by the overall angle distribution.

While the angle distribution we show in Fig. 5-19a is fundamentally what we want to compare with the distribution in Fig. 5-24a, some adjustments must be made so that the data is truly comparable. First the raw angle distribution for the normal component hot spots is normalized by the angle distribution for the whole microstructure, creating Fig. 5-25. The next change is to recognize that the initial angle measured from this work is from the normal while the angle measured from the shock loading experiment is the complement of that angle and was the angle from the grain boundary trace; Fig. 5-24b shows the normalized Fig. 5-25 as the complement angle and with the bin size used in Fig. 5-24a. In comparing these two angle distributions, we see that there is very strong similarity between the distributions; both of them show strong trends towards a 90˚ angle that represent boundaries that are perpendicular to the loading/shock direction. Such a trend indicates that the original hypothesis, which stated that void nucleation in shock-loaded copper polycrystals is dependent on extreme values of grain boundary surface tractions, is a reasonable expectation for the evidence presented up to this point. In order

for a boundary to fail and a void to nucleate a sufficient stress must be placed on it and the normal component of traction represents a measure of that.

However, a closer inspection of this comparison indicates that there may be additional factors that go along with the normal component of traction in characterizing the nucleation of voids. Comparing the normalized volume fraction of the plots in Fig. 5-24, it appears that the normal component hot spots trend more sharply to 90˚ than the voided boundaries from the shock loaded copper experiment. The normal component hot spots have a greater volume fraction in the 45˚-90˚ while in the 0˚-45˚ bins the voided boundaries have more presence. Such differences are indicative of other factors that influence the nucleation of voids at grain boundaries. These factors should represent the ability for a given grain boundary to resist damage and thus different grain boundaries may nucleate voids under different amounts of load. For example, a grain boundary could have a very high normal component of traction but not nucleate a void if it has a high resistance to damage, which would explain why the 67.5˚-90˚ bin for the normal component hot spots is much higher, and similarly a grain boundary could have a comparatively low normal component of traction yet still nucleate a void if it has a low resistance to damage, which would explain why the 0˚-22.5˚ bin for the voided grain boundaries is much higher.

An example of this idea of grain boundary damage resistance is presented in works by Fensin *et al.*[40, 41] that used molecular dynamics simulations to investigate possible grain boundary properties that might correlate with void nucleation. Shock loading conditions were simulated on a copper bicrystal with grain boundaries conforming to certain known coincident site lattice (CSL) arrangements. The load experienced by the boundaries that

led to failure was recorded and compared against common parameters associated with the grain boundary itself. The parameters considered were grain boundary energy, excess volume, energy of separation, which is the difference between the grain boundary energy and the energy of the two free surfaces created by its separation, and excess energy, which is the energy increase in the system due to plasticity. What they found is that none of the first three parameters correlated with the grain boundary failure load while the final one correlated positively with increasing failure load. This appears to indicate that the grain boundary resistance to damage may depend more on the grain boundary response to plastic deformation and not on basic descriptive parameters of grain boundary character. To take into account these new observations, the hypothesis is revised to read: "Void nucleation in shock-loaded copper polycrystals is dependent on extreme values of grain boundary surface tractions as well as measures of a grain boundaries resistance to damage." To investigate these this new hypothesis, we perform a direct comparison between experimentally measured voids and micromechanical factors generated using crystal plasticity modeling in the following chapter.

Chapter 6: Correlation of Shock-Induced Porosity with Micromechanical Factors via Simulation

6.1: Shock Loading Experiment and Image Processing

To investigate microstructural properties influencing damage initiation, this work utilizes the results of a unique experiment performed by Bingert *et al*.[109] and analyzed by Menasche *et al.* [55], whose goal was to obtain 3-D images of a material in which incipient spall occurred. In this experiment, a 99.997% pure polycrystalline copper sample was machined into a 1.2 mm diameter cylinder of height 2.42 mm. This sample was then characterized using nf-HEDM over a height of 0.704 mm. The sample was machined down to a 0.725 mm tall piece centered about the characterized section. This sample was then embedded into two copper polycrystal radial momentum traps and impacted by a copper flyer plate at 300 ms^{-1}. The experimental setup involved placing the ringed sample onto the front of a pipe that was slightly larger in diameter than the nf-HEDM characterized sample; thus when the target was impacted the sample alone is stripped from the momentum trapping rings and soft-captured. The velocity was specifically selected such that the sample was recovered while causing incipient spall voids. The recovered sample was then characterized using both nf-HEDM and X-ray tomography. The end result was a pair of 3-D orientation maps of the same volume as the copper sample both before the experiment and after the plate impact had produced voids within the sample. Computed tomography also provided 3-D images of the porosity distribution. The tomography provided higher spatial resolution of the voids compared to the nf-HEDM reconstruction process.

Menasche *et al*.[55] analyzed the experiment by mapping the voids characterized from the deformed sample onto the microstructure measured from the undeformed sample.

First, a technique was developed to map the voids identified via tomography in the post-shocked sample to the corresponding nf-HEDM image. This was achieved by aligning larger-scale surface features present in both sample images. Next, the nf-HEDM images of the sample both undeformed and deformed were aligned with each other through the use of rotations and affine transformations. The purpose of this was to account for differences in sample alignment of the two measurements, as well as for the plastic deformation experienced by the sample as a result of the shock loading. This plastic deformation also made registration between the two nf-HEDM datasets more difficult because defect accumulation and crystal rotation results in larger uncertainty in crystal orientation. The final result was that it was possible to identify certain regions within the nf-HEDM image of the undeformed sample as having developed voids in the deformed sample.

Using the orientation field of the undeformed sample obtained by Menasche *et al*.[55] as the input of a micromechanical simulation, this work analyzes the local response of the material in the regions developing porosity. A full-field crystal plasticity model that utilizes Fast Fourier Transforms (FFT) to solve the micromechanical governing equations[3, 63] is used to determine the local micromechanical fields under shock loading conditions, as described in the following section. Menasche *et al.* found that (see Table 6-1) of the 485 measured voids, 332 occurred at grain boundaries. Of those 332 grain boundary voids, 196 occurred on grain boundary planes, 126 occurred on triple junctions and 10 occurred on higher-order intersection points. Thus, grain boundaries regions will be the particular focus of our analysis because of the predominance of voids forming at those features. Moreover, a number of micromechanical fields can be investigated at

grain boundaries with the available modeling tools. Some of the fields that are unique to boundaries require the ability to quantitatively evaluate the interface normals. Novel techniques utilizing Cartesian moments are used to generate such values from the discrete microstructure images obtained by nf-HEDM.

6.2: Approximation of Shock Loading Conditions in EVPFFT

The presently available numerical implementation of the EVPFFT model cannot directly consider shock loading conditions. Therefore, we use the output of finite element (FE) simulations that model such conditions to provide input to the EVPFFT code. Here we use macro- and meso-scale FE simulations of the type reported by Bronkhorst *et al*.[6, 110]. As mentioned previously, the spall plane is a region of high tensile stress cause by wave interactions and it is the effect of this tensile pulse that is considered in this work. In order to simulate microstructural effects of shock loading with EVPFFT, we need to obtain from FE simulations time-evolving strain-rate boundary conditions and Voce hardening parameters. For this, a FE simulation including a damage model described elsewhere[110] was run for polycrystalline copper under shock loading conditions, to the point in time where the model predicted that damage initiation occurred. The sample geometry and loading type in this simulation represented the experiment by Bingert *et al.*[109]. This FE model predicted the time after impact at which void nucleation began, 0.15 μs, as well as the peak stresses at the spallation plane, in the shock and radial directions, 944.77 MPa and 894.5 MPa, respectively as shown in Fig. 6-1a. Such values of stress indicate a large hydrostatic stress component with an overall tensile plastic response. Assuming a constant stress rate from 0 to the peak stress tensor, and discretizing the time from 0 to 0.15 μs in 299 steps, the strain rate at each time step was

obtained. Fig. 6-1b shows the resulting diagonal strain components as a function of time. The resulting sequence of strain rates was applied directly as the boundary conditions for the EVPFFT simulation. The Voce hardening parameters were calibrated so as to reproduce the stress-strain response predicted by the FE model for polycrystalline copper. The result of this fit is shown in Fig. 6-1c for the deviatoric and mean components of the stress. The root mean square error between the FE and EVPFFT models for the von Mises stress-strain response is 1.31 % with the Voce hardening parameters being τ_0 = 4.688, τ_1 = 0.6984, θ_0 = 34.1 and θ_1 = 34.

Overall, this method of approximation assumes that the loading conditions taken from the macro-scale model at the location of peak stress occurs homogeneously throughout the entire EVPFFT simulation volume. The copper sample that was recorded had a thickness of 0.725 mm as described in Section 6.1. Of that sample, 0.256 mm of it is utilized for the EVPFFT simulation, with the middle of it representing the peak stress location in the macro-scale model. Comparing such a length to the peak width in Fig. 6-1(a), the variance in stress across that length is small and thus an approximation of homogeneous boundary conditions is acceptable for simulation that moment of the tensile peak. There are also other aspects of shock loading that cannot currently be simulated in EVPFFT. The compressive wave that precedes the tensile pulse cannot be simulated without a kinematic hardening model, which allows for proper hardening behavior in any kind of cyclical or sequential loading. What are lost from this part of the shock response are possible heterogeneous stress or defect concentrations that occur ahead of the tensile pulse. Nevertheless the compressive wave should not nucleate damage and is considered to be unimportant here. Another aspect of heterogeneity that is not accounted for is the

elastic compressibility of the material, which is not necessarily linear and could change the density of the material heterogeneously and thus affect the equation of state as well. However, in this experiment the loading results in smaller strain rates that diminish the effects of this phenomenon. The EVPFFT simulation also does not yet take into account effects from micro-inertia, though it may not play a large role in the micromechanical response of this sample before void nucleation. The strain rates present during the tensile pulse in this experiment are not known to generate large effects from micro-inertia and thus they likely will not be significantly present during void nucleation. Also, most experimental evidence shows that micro-inertia plays its most significant role in the growth or collapse of voids after they have formed and thus might not be greatly involved in the nucleation stage[111, 112].

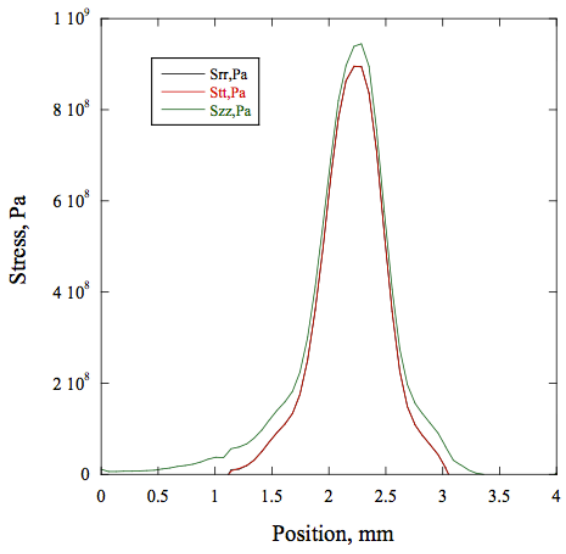

(a)

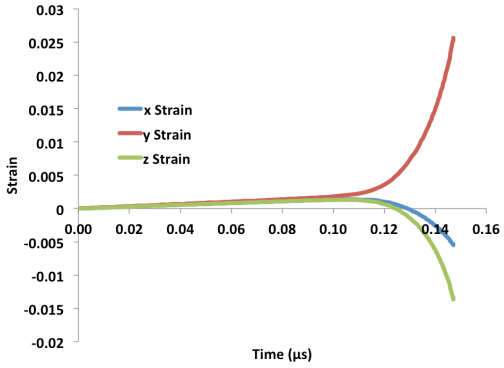

(b)

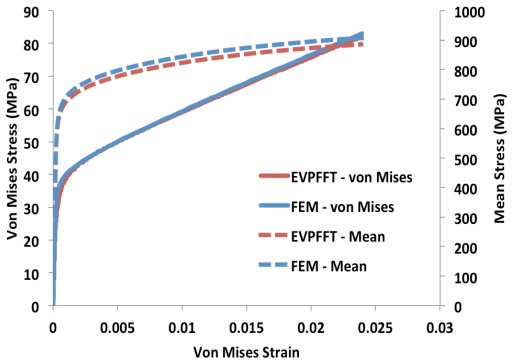

(c)

Figure 6-1. The (a) stress distribution at time of nucleation in the macro-scale model, (b) strain history recorded from the FE simulation and applied to the EVPFFT simulation and the (c) strain-strain plots for the crystal plasticity FE simulation and the EVPFFT simulation applied the hardening parameters to fit.

6.3: Simulation Set-up

The approximation of shock loading conditions described previously is applied to the voxelized microstructure image of the undeformed sample. For this, a unit cell must be properly constructed to perform the simulation. The rectangular grid of the nf-HEDM image has voxel dimensions of 768 x 768 x 64 where the inter-voxel spacing is 2 μm in the x- and y-directions and 4 μm in the z-direction. The resulting image is shown in Fig. 6-2(a). The next step is to construct a prismatic unit cell by embedding the nf-HEDM microstructure into a periodic polycrystalline unit cell. The purpose of this is two-fold: a) to represent the presence of the momentum trap rings used in the experiment, which were also polycrystalline copper with the same grain size, and b) provide the geometry and periodicity required by the EVPFFT model to operate upon. The polycrystalline microstructure surrounding the measured Cu sample was numerically generated using the Dream.3D[76] software package, and consists of randomly oriented FCC grains with an average grain size equivalent to that of the nf-HEDM microstructure. The combined microstructure image is shown in Fig. 6-2(b).

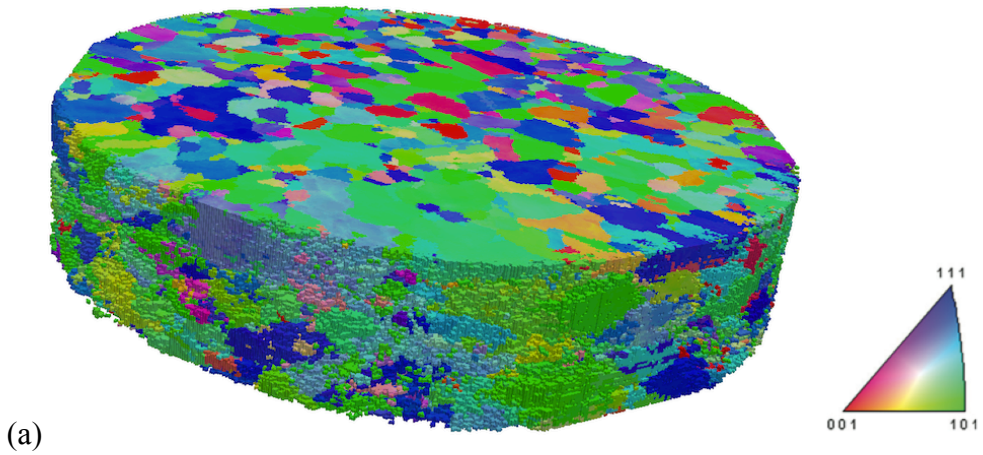

(a)

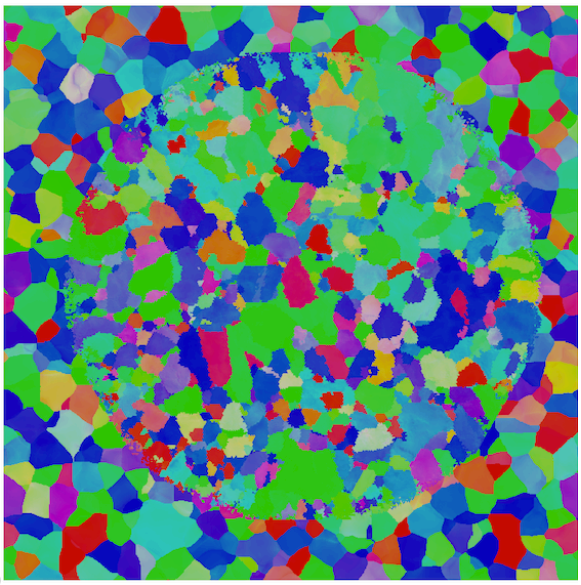

(b)

Figure 6-2. Orientation map of undeformed copper polycrystalline sample (a) measured via nf-HEDM that was (b) embedded in random copper polycrystal.

After applying the boundary conditions described in Section 6.2, the EVPFFT model gives the values of: Cauchy stress tensor, strain tensor, plastic strain rate tensor, updated orientation, Taylor factor and accumulated plastic energy density fields, for each voxel in the microstructure image. From the stress and strain tensors, their von Mises equivalents are obtained. Furthermore, with the mean stress also extracted from the stress tensor, the stress triaxiality (mean stress/von Mises stress) can be readily calculated. The Taylor

factor is a scalar parameter that describes the ability of a given grain with a specific crystallographic orientation to accommodate the deformation to which it is subjected. Here the Taylor factor is calculated locally as follows[10]:

$$M(x) = \frac{\sum_{s=1}^{N^s} |\dot{\gamma}^s(x)|}{\dot{\varepsilon}_{vm}(x)} \tag{6.1}$$

where $\dot{\gamma}^s(x)$ is the local shear rate on slip system *s*, N^s is the total number of slip systems and $\dot{\varepsilon}_{vm}(x)$ is the local von Mises equivalent strain rate. In what follows, the analysis is performed on the Taylor factor field calculated at the final step of the simulation. The accumulated plastic work density represents the time integration of the rate of plastic work. This rate is calculated at each step of the EVPFFT simulation and is given by the following equation:

$$\dot{W}^p(x) = \boldsymbol{\sigma}(x) : \dot{\boldsymbol{\varepsilon}}^p(x) \tag{6.2}$$

Using the grain boundary normal calculation technique described previously, along with the stress fields generated by the model, the grain boundary surface traction as well as its components are calculated according to Equation 5.3. Similar tractions can be calculated for the triple junctions, but this requires an additional step. The triple junction vector technique generates vectors that are tangent to the feature of interest rather than perpendicular, which is needed to describe a surface traction. Since a triple junction is a one-dimensional feature, there is not a unique perpendicular direction to it. Therefore, we choose to use the perpendicular vector that results in the largest normal component of traction as the one that represents the surface traction for the triple junctions:

$$\vec{T}_i^n(x) = \max_{0 \le \theta \le 360} \{\sigma_{ij}(x)(R_{jk}(\theta)\hat{t}_k(x))\} \tag{6.3}$$

where $\hat{t}_k$ is one of the two unused principal axes (calculated from the eigenvectors of the second order moment matrix) that is perpendicular to the triple junction line vector, and R^{θ}_{jk} applies a rotation, θ, around the triple junction line vector.

6.4: Registration

Mapping the locations of the voids onto the undeformed sample image requires the tomographic image of the voids. However, although the resolution of the tomographic image in the *x*- and *y*- directions is the same as the nf-HEDM image, the *z*-resolution of the tomography image is 1.5 μm rather than 4 μm. The alignment established by Menasche *et al*.[55] between the tomography of the deformed sample and the nf-HEDM of the undeformed sample allows voxels in both images to be measured by a unified set of coordinates established from the sample geometry. In order to register the void voxels measured by the tomography to the nf-HEDM image, we identify the nf-HEDM voxels that overlap the same physical space as the void voxels of the tomography. However, the difference in z-resolution between the images means that some voids will not be distinguishable from each other when they are registered to the nf-HEDM image, thus causing discrepancies in the void counts from Menasche *et al*.[55]. After the voids are rendered in the undeformed sample image (see Fig. 6-3), 447 voids are identified in the microstructure, with 308 of them being located on grain boundaries. Of those 308 grain boundary voids, 156 are located on grain boundary planes, 99 are located on triple junctions and 53 are located on higher order intersection points.

Type of Interface	Menasche *et al.*	This work
Total Voids	485	447
All Interface Voids	332 (68.5 %)	308 (68.9 %)
Grain Boundary Plane	196 (40.4 %)	156 (34.9 %)
Triple Junction	126 (26.0 %)	99 (22.2 %)
Higher-Order Interface	10 (2.1 %)	53 (11.9 %)

Table 6-1: Distribution of voids at grain boundary features from Menasche *et al.*[55] and from this work.

As shown in Table 6-1, while the overall ratio of grain boundary voids to total voids is the same as in Menasche *et al.*[55], the breakdown of grain boundary voids is different. This is most extreme for the higher order intersection points and is due to the difference in z-resolution between the tomography and nf-HEDM image. The grain boundary classification of the voids is determined by counting the number of unique grains that are found in the set of voxels representing each void as well as the nearest neighbors of those void voxels. These additional voxels are considered to ensure that an accurate description of the region is accounted for. For example, there are cases where a void occurred on a grain boundary but grew preferentially into one grain versus the other; such a void may only be directly represented by voxels belonging to a single grain.

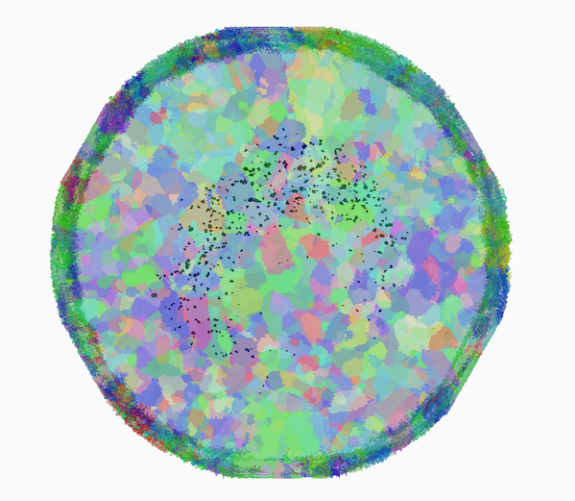

Figure 6-3. The voxels representing voids formed in shock loading, in black, are displayed within the transparent orientation map of the nf-HEDM of the undeformed microstructure, viewed along the shock direction. Note that the voids form an annulus with varying density of voids around the ring.

To determine the influence of the different micromechanical fields described above on void initiation, discrete probability distributions of these fields are plotted for both all grain boundary voxels and for the grain boundary voxels associated with voids. The set of voxels representing the grain boundaries of the overall microstructure are limited to those within a certain sub-volume of the image both to represent the spallation region from the experiment and because of potential localization issues discussed in Menasche *et al.*[55]. This sub-volume is the set of voxels within layers 212 to 583 along the *x*-axis and 191 to 572 along the *y*-axis and is displayed in Fig. 6-4. The full length of the *z*-axis is included in this sub-volume. These dimensions correspond to the farthest extent at which the voids exist within the microstructure. Outside this region no voids were detected in the tomography. The set of voxels included in the analysis on grain boundary developing voids is limited to voxels that are identified as being grain boundary voxels. Within that set, a voxel is considered a part of the void analysis if it is labeled as a void voxel from the tomography information or is a neighbor to such a voxel.

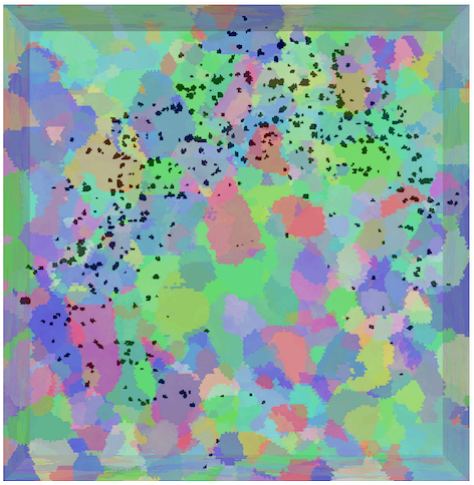

Figure 6-4. The sub-volume, which is a part of Fig. 6-3, that is used in the analysis of the void locations shown in black.

6.5: Comparison Between Distributions: Hellinger Distance

In order to compare distributions of micromechanical fields for the full set of grain boundary voxels ("full" distributions) versus the corresponding distributions restricted to those voxels that developed porosity after the shock ("restricted" distributions) we quantify the difference between distributions using the Hellinger distance[113], which is calculated as:

$$d_H(U,V) = \frac{1}{\sqrt{2}}\sqrt{\sum_{i=1}^{k}(\sqrt{u_i}-\sqrt{v_i})^2} \tag{6.4}$$

where U and V are discrete probability distributions, u_i and v_i are the probability values for the i^{th} bin of U and V respectively and k is the total number of bins in the probability distribution. The reciprocal square root of two in the pre-factor ensures that the Hellinger distance has a range of zero to one, which sets apart from similar measures of probability distribution distances such as the Bhattacharyya distance or the Kullback-Leibler divergence that do not have an upper limit for how different two distributions can be.

Over this range, a value of zero indicates that the two distributions are identical while a value of one indicates that there is zero overlap between the two distributions.

Next we evaluate correlations of porosity with micro-mechanical response. The simplest micromechanical fields relevant to this comparison are mean stress, von Mises stress, von Mises strain and stress triaxiality, which are directly calculated from the stress and strain tensors predicted by the EVPFFT model at every point in the material. The number of discrete bins used to generate the probability distributions is the largest number of bins that can be used while maintaining a psuedo-continuous trend from one bin to the next for the grain boundary void distributions, due to their smaller number of data points.

6.6: Results

The comparisons of the distributions of these fields are shown in Fig. 6-5. The violin plots display a smoothed representation, reflected with respect to the horizontal axis, of the discrete probability distribution with a boxplot displayed within. The edges of the grey boxplot correspond to the first and third quartiles, the black line shows the 1.5 interquartile range limits; the combination of solid circle and vertical line represents the median while the crossed circle represents the mean. The Hellinger distances for these fields are 0.082 for the hydrostatic stress, 0.068 for the von Mises stress, 0.075 for the von Mises strain, and 0.062 for the stress triaxiality. Consistent with these low values, there is no significant difference in the medians or spreads between the distributions; the most notable difference is how the upper tails of the stress triaxiality distributions differ. Note that as described in Section 2.4, the triaxiality for this approximation of shock loading is quite large as compared to a typical tensile test.

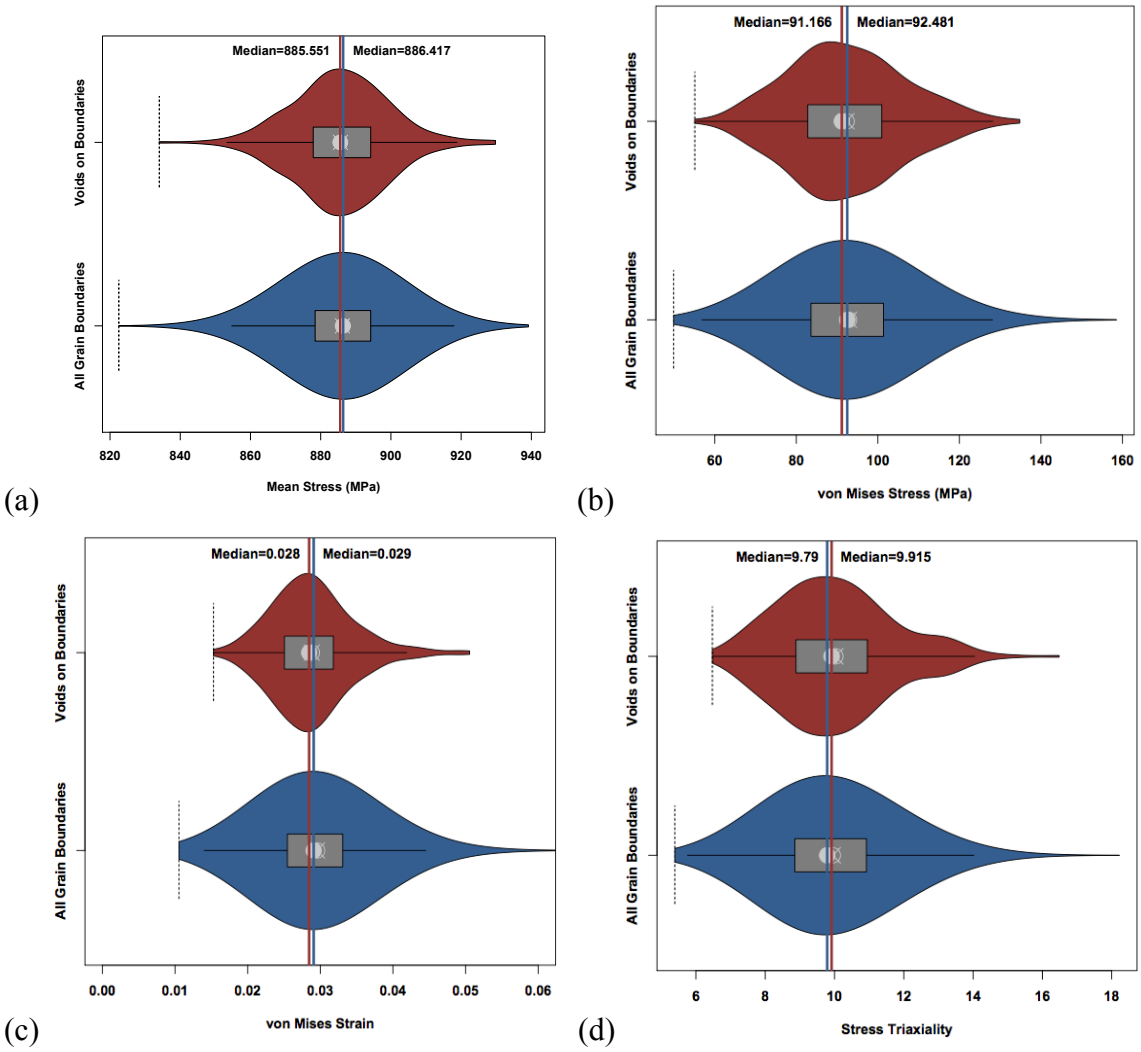

Figure 6-5. Violin plots of the distributions of (a) mean stress, (b) von Mises stress, (c) von Mises strain and (d) stress triaxiality for both the overall set of grain boundaries and for the grain boundaries at the void locations.

The next field distributions considered are those associated grain boundary features, namely the normal component of the surface tractions and grain boundary inclination angles. For the surface traction distributions, values from both the grain boundary planes and the triple junction lines are represented together in Fig. 6-6, where the Hellinger distance is 0.066, which is negligible.

The grain boundary inclination angles are relative to the shock direction and have been separated between those for grain boundary planes and those for triple junctions as

shown in Fig. 6-7 and have Hellinger distances of 0.036 and 0.024 respectively, also negligibly different. Violin plots were not used because of the difficulty in rendering distributions that have finite set limits. None of these factors show much difference in the distributions for grain boundaries vicinal to pores versus those for all boundaries; likewise, the Hellinger distances are also small.

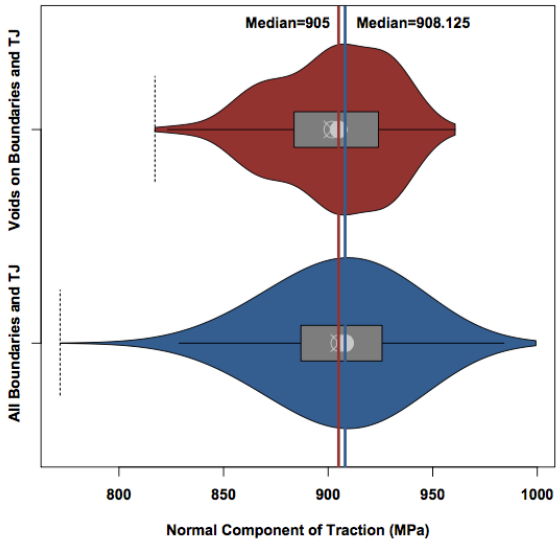

Figure 6-6. Violin plots comparing surface normal tractions for all grain boundaries and for the grain boundaries where voids are located.

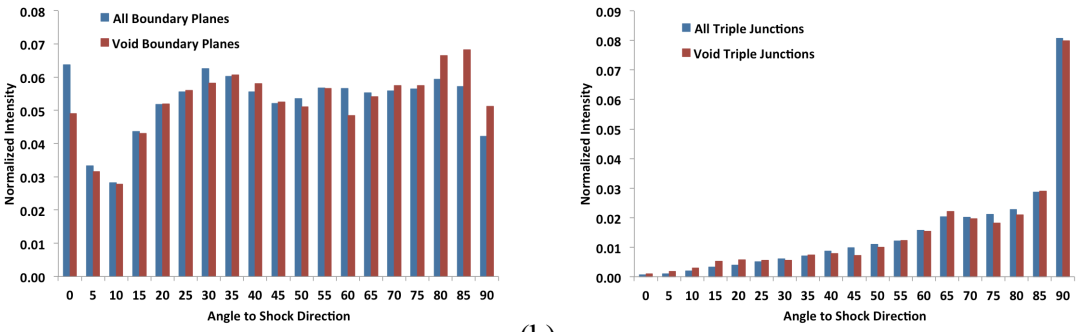

(a) (b)

Figure 6-7. Comparison between all grain boundaries and grain boundaries developing porosity for: (a) the grain boundary plane normal inclination to shock direction and for (b) the triple junction tangent vector inclination to shock direction.

Next, the local Taylor factor and plastic work are used to describe the contrast in plastic response of the grains on both sides of a boundary by finding the greatest absolute difference in the local values on both sides. The resulting distribution comparisons are shown in Fig. 6-8. The distributions of the Taylor factor difference have a Hellinger distance of 0.276 while the distributions of the plastic work difference have a Hellinger distance of 0.326. These values are well above zero and are noticeably larger than for any of the other distributions compared previously. There is also a noticeable difference between the medians for both micromechanical indicators with the entirety of the grain boundaries producing voids distributions being shifted to higher values compared to the full distributions. Differences in von Mises equivalent stress and strain were also observed and showed similar but weaker trends to the differences in Taylor factor and plastic work. Given the obvious connections between all these factors, only the differences in Taylor factor and plastic work are presented to avoid redundancy.

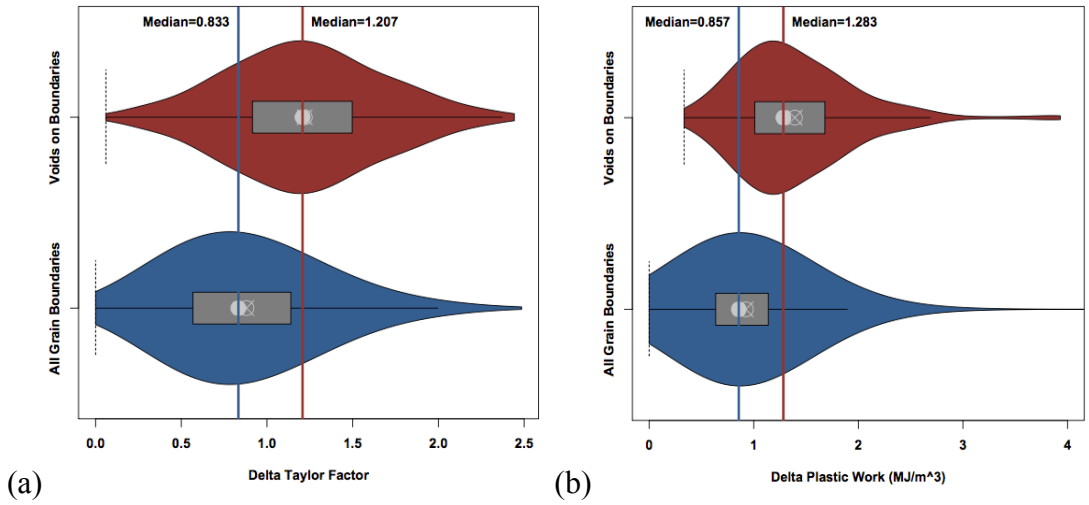

Figure 6-8. Violin plots of the distributions of (a) difference in Taylor factor and (b) difference in plastic work across a grain boundary for both the overall set of grain boundaries and for the grain boundaries at the void locations.

Further granularity can be obtained by sub-dividing the distributions considered above based on the character of the grain boundaries involved. As described previously, there is particular interest in Σ3 grain boundaries in copper polycrystals, thus the distributions shown previously are separated into distributions for Σ3 boundaries and for all other boundaries. For this analysis, the boundaries that are counted as Σ3 are those that are within 5° of rotation of the specific Σ3 misorientation of a 60° around a <111> crystal axis. The data are separated into distributions for the two different grain boundary types, which are then further separated into plots for void boundaries and for all boundaries, with the difference in Taylor factor shown in Fig. 6-9 and the difference in plastic work in Fig. 6-10.

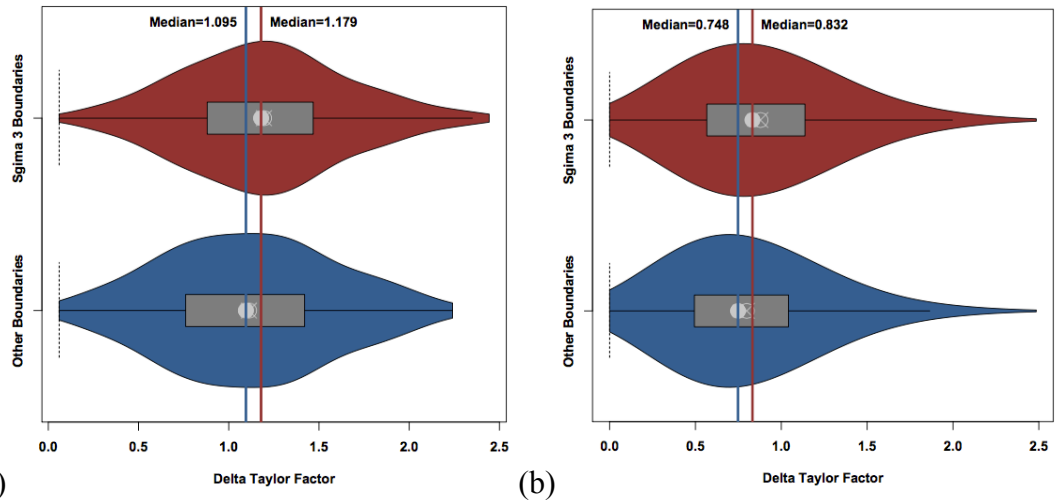

Figure 6-9. Violin plots for difference in Taylor factor partitioned by grain boundary type into sets for Σ3 boundaries and all other boundaries and separately displayed for (a) the voids on grain boundaries and for (b) the set of all grain boundaries.

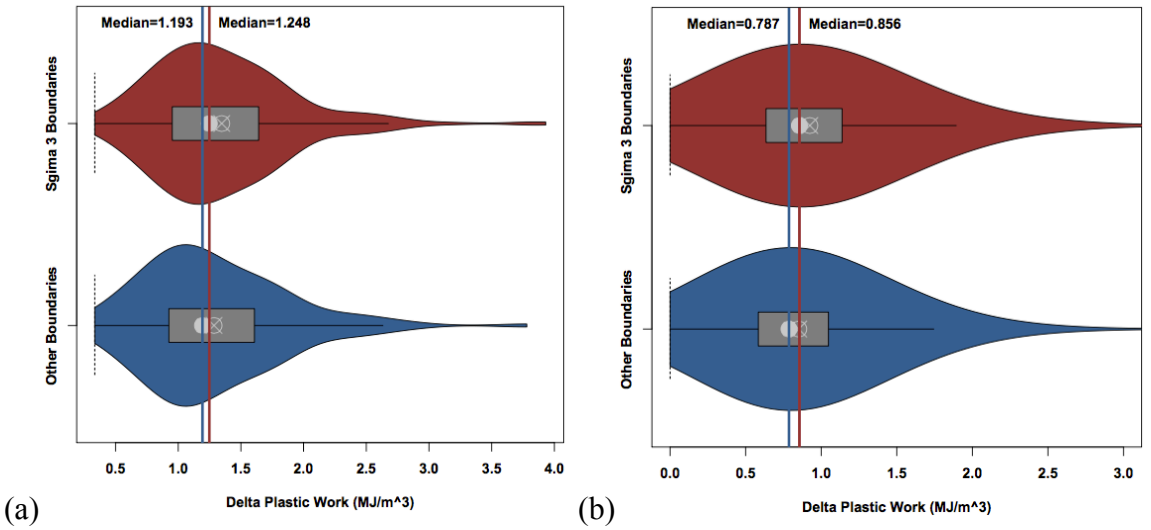

Figure 6-10. Violin plots for difference in plastic work partitioned by grain boundary type into sets for Σ3 boundaries and all other boundaries and separately displayed for (a) the grain boundaries developing porosity and for (b) all grain boundaries.

For the difference in Taylor factor, the Hellinger distance between Σ3 boundaries and all other boundaries is 0.182 for the grain boundary void voxels and 0.136 for all grain boundary voxels. For the difference in plastic work, the Hellinger distance between Σ3 boundaries and all other boundaries is 0.151 for the restricted distribution and 0.12 for the full distribution. For both distributions the Σ3 boundaries are shifted towards slightly larger values, which can be interpreted as an indication of this special boundary type being associated with greater plasticity differences for voiding. Another way of analyzing the significance of grain boundary type is to calculate Hellinger distances between the full and restricted distributions for the two grain boundary groups, rather than between the grain boundary groups within the full and restricted distributions separately, as shown previously. The resulting Hellinger distances, along with those found before the separation by grain boundary character, are shown in Table 6-2. Both forms of comparison show that Σ3 boundaries with voids have slightly greater differences than the other boundaries.

Voids vs. Overall	Combined	Σ3 Boundaries	Other Boundaries
Taylor Factor Difference	0.276	0.287	0.262
Plastic Work Difference	0.323	0.334	0.313

Table 6-2: Hellinger Distances between Void and Overall Distributions by GB Character

6.4: Discussion

While the predicted stress and strain distributions shown in Fig. 6-5 have no correlations with the subsequent occurrence of void nucleation at grain boundaries, Fig. 6-8 indicates that the more elaborate measures of the mechanical response at the boundaries do. In effect, two-point correlation measures (differences in Taylor factor and plastic work), point to significant microstructural effects whereas one-point ones do not. There is also no correlation between grain boundary inclination to the shock direction and void nucleation as shown in Fig. 6-7, a result that is in contradiction to what has been found in other experiments mentioned previously and requires a change to the previous considerations given to the normal component of traction. However, the particular size and scale of the sample and experiment might explain the different observations. Given that stress triaxiality already has been connected to damage processes in previous studies, in particular by McClintock[114] and by Rice and Tracey[115], it is surprising that no correlation exists in this data set, Fig. 6-5(d). However, it cannot be determined if this is due to void nucleation or void growth, and it is the former that stress triaxiality is most closely associated with, e.g., in the necks of tensile samples. Note that stress triaxiality has been a useful quantity within macro-scale analyses of porosity evolution but it is not clear how physically meaningful stress triaxiality is at the length scales of the single crystal. In other words, the results presented here show that, while high triaxiality may

assist void formation, especially where fracture of second phase particles initiates voiding, e.g. Maire *et al*.[116], local variations at the microstructure scale do not explain specific occurrences of voids.

The most interesting results presented above are those corresponding to differences in Taylor factor and plastic work across the boundaries. The differences between the full and restricted distributions is greater than for any other micromechanical fields, and not just a difference in shape but also a large difference in medians as well. What this implies is that damage tends to occur preferentially on grain boundaries that are interfaces between crystals that have a greater contrast in plastic response. As the material deforms, these highly contrasted grain pairs begin to experience greater differences in local stress and strain that eventually leads to incompatibility that promotes damage. Previous experimental works[25, 26, 35-39] have found potential relationships between differences in Taylor factor and damage by measuring orientations, but differences in plastic work were not explored in this context, because micromechanical simulations are required to obtain this information. Taylor factor is a variable that can change with strain as the crystals rotate and harden with deformation, while plastic work is an accumulated value; despite this difference, the distributions of these magnitudes are comparable in this case, because relatively small plastic strains were involved.

While there is a clear difference between grain boundaries that developed voids and those that do not, the separation is not absolute; there are boundaries in other parts of the microstructure with similar contrast in plastic properties where no damage was found. One possible explanation is that the presence of damage depends on other factors in addition to plasticity contrast, such as the stress factors analyzed previously (i.e. von

Mises stress and surface traction) or grain boundary character. These potential additional influences might only become revealed with in situ measurements that describe the order in which the voids nucleated. Another aspect to consider is that the EVPFFT model, like many crystal plasticity models, does not incorporate the influence of the grain boundary structure on the mechanical response. Roters *et al.*[117] showed that the effects of not considering such influences can be large by comparing models with various levels of grain boundary mechanics to bicrystal experiments. One example of such an influence is slip transmission; works by Bieler *et al*. [7, 38] discuss many of the influences of slip transmission on micromechanics.

In general, the Σ3 boundaries on which voids occurred are shifted towards slightly higher differences in Taylor factor and plastic work when compared to both the rest of the grain boundaries as well as the Σ3 boundaries that did not develop damage. Such shifts hint at the elevated resistance to damage of Σ3 boundaries, which is also shown in other studies. However, the shifts seen in the present analysis are quite small and further statistical analysis is needed to confirm if it is significant. These results do, however, agree with what was observed by Menasche *et al*.[55] on this same data set, who found that there is no significant difference in the occurrence of damage on Σ3 boundaries versus other boundary types, a trend that was also observed when considered here on the nf-HEDM image. However, the influence of grain boundary structure on the polycrystalline mechanical response is not yet sufficiently understood and therefore not yet implemented in EVPFFT, which precluded evaluation of its effect on the micromechanical field distributions in this instance.

Chapter 7: Conclusions & Future Work

7.1: Conclusions

To investigate mechanical parameters that may be associated with void nucleation we initially investigated correlations between grain boundary surface traction hot spots and other micromechanical values and microstructure features with the hypothesis that damage is connected to extreme values of surface tractions. To do this, an elasto-viscoplastic Fast Fourier Transform-based simulation was used to determine the local micromechanical fields within a copper polycrystal. A technique for quantifying surface normals from discrete images was developed so that the surface tractions could be calculated. Multiple microstructures have uniaxial tension, uniaxial compression and pure shear simulated on them and the resulting data is combined with extreme value theory to identify which parts of the microstructure may be described as surface traction hot spots. We observed that the normal component traction hot spots showed some correlation with hydrostatic stress while shear component traction hot spots did not, which indicated a greater importance for the normal component since hydrostatic stress is often associated with void nucleation. Both forms of surface traction hot spots also showed particular correlations with grain boundary inclination to the principal loading directions. The normal component hot spots occurred at boundaries that were perpendicular/parallel to the principal loading directions while the shear component hot spots occurred at boundaries that inclined 45° to the principal loading directions. When observing trends in void occurrence from experimental measurements in literature, the preferred grain boundary inclination is perpendicular to the tensile principal axis, indicating that the normal component of traction has the greater potential to be associated with void

nucleation. However, in these experimental observations there were differences in the trends for grain boundary inclination that show the normal component of traction on its own may not be sufficient to predict void nucleation and that grain boundary properties may also play a role.

We then made use of newly available experimental data on shock loaded polycrystalline copper to perform a more direct analysis on determining the factors important to void nucleation. By utilizing near-field high-energy diffraction microscopy as well as X-ray tomography, we were able to access a three-dimensional microstructure image while knowing where within the microstructure voids will eventually form due to shock loading. To perform a simulation in comparison to the experimental data, we developed a method of approximating the shock loading conditions using the quasi-static EVPFFT model. To determine any connection between the simulation results and the presence of voids, the distributions for any given factor are generated for the parts of grain boundaries that develop voids and for the rest of the grain boundaries. These distributions are then compared and quantified against each other. The result was that basic micromechanical factors as well as the surface traction and grain boundary inclination angles did not correlate with the occurrence of voids. Instead, it was two-point correlations across the grain boundary, namely difference in Taylor factor and difference in plastic work that correlated with damage. The grain boundaries that produced voids had higher values of these parameters than the rest of the microstructure. Past work[25, 26, 35-39] has also identified influences due to difference in plastic response at the grain boundary but neither fully quantified such factors nor performed the analysis on as large a data set as this work. The conclusion is therefor that the original hypothesis on the role

of surface tractions in void nucleation is incorrect. However, these analyses also demonstrated that factors relating to the difference in mechanical behavior across the grain boundary are important.

7.2: Future Work

Clearly the current data set could be subjected to a more rigorous statistical analysis. The current analysis could, e.g., be quantified further by applying a principal component analysis to it. Furthermore, to reinforce the significance of the findings, random synthetic void sets could be generated and analyzed to ensure that the results associated with the real voids are unique; in particular, this would be important for determining the significance for the observations made for the Σ3 boundaries. Beyond the currently existing data, the first consideration must be the inclusion and development of more grain boundary mechanics in the micromechanical simulation. In particular, the mechanics of slip transmission across the grain boundary appear to be important for improving the accuracy of the mechanical fields in the vicinity of grain boundaries. There are several different hypotheses about how slip interacts with grain boundaries that could be tested. One possible method of implementing these grain boundary mechanics would be by adding slip transmissibility information to strain-gradient plasticity models that are being incorporated to the FFT-based formalism. The technique to characterize grain boundaries and triple junctions has many possible uses in material science, particularly in research pertaining to grain boundary energy and grain growth. Utilizing these techniques to calculate the dihedral angles between grain boundaries around a triple junction would be a relatively simple endeavor and would be useful for the aforementioned research areas.

From that point there are two paths that may be explored in continuing this work. One path is to continue to utilize the data generated by the polycrystalline copper shock loading experiment. To do so, the ability of the micromechanical model to approximate the shock loading conditions must be improved. To start, the macro-scale model utilized previously should be run with conditions that more closely mirror those of the experiment. The EVPFFT model could also undergo a number of changes to improve its ability to approximate shock loading. The simplest and yet most critical is to incorporate a kinematic hardening mode into the model so that the compressive and tensile effects of the shock loading can both be applied to the copper microstructure. By including the compressive part of the shock loading, the influences of crystal hardening and reorientation caused by the compressive wave can be accounted for. Another feature that can be included is the mechanics of micro-inertia, under dynamic loading, which when applied changes the stress equilibrium equation mentioned in Chapter 3 to depend on the mass acceleration within the material and thus effects the mathematics of the model itself. The possibility of spatially complex loading conditions, such as those found in shock loading and seen in Fig. 6-1a, must also be explored though there is not yet any precedent of it being applied to a model like the EVPFFT. Beyond just the data from this experiment, further shock loading experiments on these small, HEDM-compatible samples is necessary so that the difference in grain boundary inclination trends observed between this experiment and standard shock loading experiments may be explored.

The other path is to instead perform another experiment with a loading condition that is closer to the EVPFFT model's current capabilities. The Advanced Photon Source, where the nf-HEDM measurements are performed, is capable of performing quasi-static

loading experiments within the beam-line apparatus[50, 118]. Thus a quasi-static experiment may be performed with the same goal of identifying voids in a deformed nf-HEDM image and tracing them back to the original sample measurement. Even beyond that, because the experiment can be performed in-situ multiple images may be recorded during the course of the deformation process. Instead of only comparing an initial image to a final, deformed and damaged image, the voids can be tracked as they appear. Such in situ data would allow for a much more detailed analysis of the void nucleation events, which could possibly identify the role surface tractions might play in nucleation. Another possibility is that, rather than determining where in the microstructure voids nucleate (in the sense of site-saturated nucleation) as this work investigated, it may be more interesting to determine the order in which they nucleate (in the sense of continuous nucleation).

Once both these paths have been pursued, one can then use the information gained from the in-situ measurements of damage nucleation to try and predict the damage nucleation events under shock loading conditions. Whether these predictions prove accurate or not will be greatly informative about the similarities and differences between the mechanisms of void nucleation under quasi-static and dynamic loading. Increased experimental ability to measure dynamic loading events, achieved via faster rates of imagining in new beam lines, will also greatly improve the ability to characterize damage nucleation. Another possible direction is to explore the roles surface tractions may play in other areas of interest, such as fatigue damage or crack nucleation/growth.

References:

[1] D. R. Curran, L. Seaman, and D. A. Shockey, "Dynamic failure of solids," *Physics Reports,* vol. 147, pp. 253-388, 1987.

[2] W. M. Garrison Jr and N. R. Moody, "Ductile fracture," *Journal of Physics and Chemistry of Solids,* vol. 48, pp. 1035-1074, 1987.

[3] R. A. Lebensohn, A. K. Kanjarla, and P. Eisenlohr, "An elasto-viscoplastic formulation based on fast Fourier transforms for the prediction of micromechanical fields in polycrystalline materials," *International Journal of Plasticity,* vol. 32-33, pp. 59-69, 2012.

[4] P. Shanthraj and M. A. Zikry, "Dislocation density evolution and interactions in crystalline materials," *Acta Materialia,* vol. 59, pp. 7695-7702, 2011.

[5] W. M. Ashmawi and M. A. Zikry, "Grain boundary effects and void porosity evolution," *Mechanics of Materials,* vol. 35, pp. 537-52, 2003.

[6] C. A. Bronkhorst, B. L. Hansen, E. K. Cerreta, and J. F. Bingert, "Modeling the microstructural evolution of metallic polycrystalline materials under localization conditions," *Journal of the Mechanics and Physics of Solids,* vol. 55, pp. 2351-2383, 2007.

[7] T. R. Bieler, P. Eisenlohr, F. Roters, D. Kumar, D. E. Mason, M. A. Crimp*, et al.*, "The role of heterogeneous deformation on damage nucleation at grain boundaries in single phase metals," *International Journal of Plasticity,* vol. 25, pp. 1655-1683, 2009.

[8] B. Liu, D. Raabe, F. Roters, P. Eisenlohr, and R. A. Lebensohn, "Comparison of finite element and fast Fourier transform crystal plasticity solvers for texture prediction," *Modelling and Simulation in Materials Science and Engineering,* vol. 18, p. 085005, 2010.

[9] E. J. Lieberman, R. A. Lebensohn, D. B. Menasche, C. A. Bronkhorst, and A. D. Rollett, "Microstructural effects on damage evolution in shocked copper polycrystals," *Acta Materialia,* vol. 116, pp. 270-280, 9/1/ 2016.

[10] C. N. Reid, *Deformation geometry for materials scientists*, [1st ed.] ed. Pergamon Press: Oxford, 1973.

[11] S. R. Kalidindi, A. Bhattacharyya, and R. D. Doherty, "Detailed analyses of grain–scale plastic deformation in columnar polycrystalline aluminium using orientation image mapping and crystal plasticity models," *Proceedings of the Royal Society of London. Series A: Mathematical, Physical and Engineering Sciences,* vol. 460, pp. 1935-1956, 2004.

[12] N. Allain-Bonasso, F. Wagner, S. Berbenni, and D. P. Field, "A study of the heterogeneity of plastic deformation in IF steel by EBSD," *Materials Science and Engineering: A,* vol. 548, pp. 56-63, 2012.

[13] E. J. Lieberman, A. D. Rollett, R. A. Lebensohn, and E. M. Kober, "Calculation of grain boundary normals directly from 3D microstructure images," *Modelling and Simulation in Materials Science and Engineering,* vol. 23, p. 035005, 2015.

[14] N. A. Fleck, J. W. Hutchinson, and V. Tvergaard, "Softening by void nucleation and growth in tension and shear," *Journal of the Mechanics and Physics of Solids,* vol. 37, pp. 515-540, 1989.

[15] G. M. Kim, G. H. Michler, M. Gahleitner, and J. Fiebig, "Relationship between morphology and micromechanical toughening mechanisms in modified polypropylenes," *Journal of Applied Polymer Science,* vol. 60, pp. 1391-1403, 1996.
[16] J. W. Hancock and A. C. Mackenzie, "On the mechanisms of ductile failure in high-strength steels subjected to multi-axial stress-states," *Journal of the Mechanics and Physics of Solids,* vol. 24, pp. 147-160, 1976.
[17] J. Gurland, "Observations on the fracture of cementite particles in a spheroidized 1.05% c steel deformed at room temperature," *Acta Metallurgica,* vol. 20, pp. 735-741, 1972.
[18] J. P. Escobedo, D. Dennis-Koller, E. Cerreta, and C. A. Bronkhorst, "Effects of grain boundary structure and distribution on the spall response of copper," *AIP Conference Proceedings,* vol. 1426, pp. 1321-1324, 2012.
[19] R. Raj and M. F. Ashby, "Intergranular fracture at elevated temperature," *Acta Metallurgica,* vol. 23, pp. 653-666, 1975.
[20] A. C. F. Cocks and M. F. Ashby, "On creep fracture by void growth," *Progress in Materials Science,* vol. 27, pp. 189-244, 1982.
[21] R. Raj and M. F. Ashby, "On grain boundary sliding and diffusional creep," *Metallurgical Transactions,* vol. 2, pp. 1113-1127, 1971/04/01 1971.
[22] J. Intrater and E. S. Machlin, "Grain-boundary sliding in copper bicrystals," *Institute of Metals -- Journal,* vol. 88, pp. 305-310, 1960.
[23] J. Belak, "On the nucleation and growth of voids at high strain-rates," *Journal of Computer-Aided Materials Design,* vol. 5, pp. 193-206, 1998/05/01 1998.
[24] R. E. Rudd and J. F. Belak, "Void nucleation and associated plasticity in dynamic fracture of polycrystalline copper: an atomistic simulation," *Computational Materials Science,* vol. 24, pp. 148-153, 2002.
[25] J. P. Escobedo, E. K. Cerreta, D. Dennis-Koller, C. P. Trujillo, and C. A. Bronkhorst, "Influence of boundary structure and near neighbor crystallographic orientation on the dynamic damage evolution during shock loading," *Philosophical Magazine,* vol. 93, pp. 833-846, 2013/03/01 2012.
[26] A. G. Perez-Bergquist, J. P. Escobedo, C. P. Trujillo, E. K. Cerreta, G. T. Gray, III, C. Brandl*, et al.*, "The role of the structure of grain boundary interfaces during shock loading," in *Shock Compression of Condensed Matter - 2011: Conference of the American Physical Society Topical Group on Shock Compression of Condensed Matter, 26 June-1 July 2011*, USA, 2012, pp. 1359-62.
[27] S. Christy, H. R. Pak, and M. A. Meyers, "Effects of Metallurgical Parameters on Dynamic Fracture by Spalling of Copper," in *Metallurgical Applications of Shock-Wave and High-Strain-Rate Phenomena*, ed: New York and Basel, 1986.
[28] J. P. Escobedo, D. Dennis-Koller, E. K. Cerreta, B. M. Patterson, C. A. Bronkhorst, B. L. Hansen*, et al.*, "Effects of grain size and boundary structure on the dynamic tensile response of copper," *Journal of Applied Physics,* vol. 110, p. 033513 (13 pp.), 08/01 2011.
[29] Z. Chen and C. Butcher, "Micromechanics modelling of ductile fracture," *Solid Mechanics and its Applications,* vol. 195, pp. 1-336, 2013.
[30] F. M. Beremin, "Cavity formation from inclusions in ductile fracture of A508 steel," *Metallurgical Transactions A,* vol. 12, pp. 723-731, 1981/05/01 1981.

[31] D. Hull and D. E. Rimmer, "The growth of grain-boundary voids under stress," *Philosophical Magazine,* vol. 4, pp. 673-687, 1959/06/01 1959.
[32] D. Field and B. Adams, "Heterogeneity of intergranular damage," *Metallurgical Transactions A,* vol. 23, pp. 2515-2526, 1992/09/01 1992.
[33] O. Diard, S. Leclercq, G. Rousselier, and G. Cailletaud, "Distribution of normal stress at grain boundaries in multicrystals: application to an intergranular damage modeling," *Computational Materials Science,* vol. 25, pp. 73-84, 9// 2002.
[34] S. J. Fensin, J. P. Escobedo-Diaz, C. Brandl, E. K. Cerreta, G. T. Gray Iii, T. C. Germann*, et al.*, "Effect of loading direction on grain boundary failure under shock loading," *Acta Materialia,* vol. 64, pp. 113-122, 2014.
[35] Y. Yang, P. Zhi-qiang, C. Xing-zhi, G. Zhao-liang, T. Tie-gang, H. Hai-bo*, et al.*, "Spall behaviors of high purity copper under sweeping detonation," *Materials Science and Engineering: A,* vol. 651, pp. 636-645, 1/10/ 2016.
[36] S. I. Wright and D. P. Field, "Recent studies of local texture and its influence on failure," *Materials Science and Engineering: A,* vol. 257, pp. 165-170, 11/30/ 1998.
[37] T. Bieler, R. L. Goetz, and S. L. Semiatin, "Anisotropic plasticity and cavity growth during upset forging of Ti–6Al–4V," *Materials Science and Engineering: A,* vol. 405, pp. 201-213, 9/25/ 2005.
[38] T. R. Bieler, P. Eisenlohr, C. Zhang, H. J. Phukan, and M. A. Crimp, "Grain boundaries and interfaces in slip transfer," *Current Opinion in Solid State and Materials Science,* vol. 18, pp. 212-226, 8// 2014.
[39] P. D. Nicolaou and S. L. Semiatin, "An analysis of cavity growth during open-die hot forging of Ti-6Al-4V," *Metallurgical and Materials Transactions A,* vol. 36, pp. 1567-1574, 2005/06/01 2005.
[40] S. J. Fensin, E. K. Cerreta, G. T. G. Iii, and S. M. Valone, "Why are some Interfaces in Materials Stronger than others?," *Sci. Rep.,* vol. 4, 2014.
[41] S. J. Fensin, S. M. Valone, E. K. Cerreta, and G. T. Gray, "Influence of grain boundary properties on spall strength: Grain boundary energy and excess volume," *Journal of Applied Physics,* vol. 112, p. 083529 (5 pp.), 2012.
[42] R. C. Boettner, A. J. McEvily, and Y. C. Liu, "On the formation of fatigue cracks at twin boundaries," *Philosophical Magazine,* vol. 10, pp. 95-106, 1964/07/01 1964.
[43] A. F. Knorr, M. Marx, and F. Schaefer, "Crack initiation at twin boundaries due to slip system mismatch," *Scripta Materialia,* vol. 94, pp. 48-51, 1/1/ 2015.
[44] C. A. Stein, A. Cerrone, T. Ozturk, S. Lee, P. Kenesei, H. Tucker*, et al.*, "Fatigue crack initiation, slip localization and twin boundaries in a nickel-based superalloy," *Current Opinion in Solid State and Materials Science,* vol. 18, pp. 244-252, 8// 2014.
[45] U. F. Kocks, C. N. Tomé, and H.-R. Wenk, *Texture and Anisotropy*: Cambridge University Press, 2000.
[46] B. L. Adams, S. I. Wright, and K. Kunze, "Orientation imaging: The emergence of a new microscopy," *Metallurgical Transactions A,* vol. 24, pp. 819-831, 1993.
[47] A. J. Schwartz, M. Kumar, and B. L. Adams, *Electron Backscatter Diffraction in Materials Science*, 2 ed. Dordrecht: Springer, 2010.

[48] R. M. Suter, D. Hennessy, C. Xiao, and U. Lienert, "Forward modeling method for microstructure reconstruction using x-ray diffraction microscopy: Single-crystal verification," *Review of Scientific Instruments,* vol. 77, pp. -, 2006.
[49] S. F. Li and R. M. Suter, "Adaptive reconstruction method for three-dimensional orientation imaging," *Journal of Applied Crystallography,* vol. 46, pp. 512-24, 2013.
[50] R. Pokharel, J. Lind, S. F. Li, P. Kenesei, R. A. Lebensohn, R. M. Suter*, et al.*, "In-situ observation of bulk 3D grain evolution during plastic deformation in polycrystalline Cu," *International Journal of Plasticity,* vol. 67, pp. 217-234, 2015.
[51] J. Lind, A. D. Rollett, R. Pokharel, C. Hefferan, S. F. Li, U. Lienert*, et al.*, "Image processing in experiments on, and simulations of plastic deformation of polycrystals," in *2014 IEEE International Conference on Image Processing (ICIP)*, 2014, pp. 4877-4881.
[52] B. Lin, Y. Jin, C. M. Hefferan, S. F. Li, J. Lind, R. M. Suter*, et al.*, "Observation of annealing twin nucleation at triple lines in nickel during grain growth," *Acta Materialia,* vol. 99, pp. 63-68, 10/15/ 2015.
[53] C. Hefferan, "Measurement of Annealing Phenomena in High Purity Metals with Near-field High Energy X-ray Diffraction Microscopy," Doctor of Philosophy Dissertation, Physics, Carnegie Mellon University, 2012.
[54] S. F. Li, J. K. Mason, J. Lind, and M. Kumar, "Quadruple nodes and grain boundary connectivity in three dimensions," *Acta Materialia,* vol. 64, pp. 220-230, 2// 2014.
[55] D. B. Menasche, J. Lind, S. F. Li, P. Kenesei, J. F. Bingert, U. Lienert*, et al.*, "Shock induced damage in copper: A before and after, three-dimensional study," *Journal of Applied Physics,* vol. 119, p. 154902, 2016.
[56] M. A. Meyers, *Dynamic behavior of materials*: John Wiley & Sons, 1994.
[57] L. S. T. Antoun, D. Curran, G. Kanel, S. Razorenov, A. Utkin, *Spall Fracture*. New York: Springer, 2002.
[58] J. R. Asay and M. Shahinpoor, *High-Pressure Shock Compression of Solids*. New York: Springer, 1993.
[59] A. Prakash and R. A. Lebensohn, "Simulation of micromechanical behavior of polycrystals: Finite elements versus fast Fourier transforms," *Modelling and Simulation in Materials Science and Engineering,* vol. 17, 2009.
[60] H. Moulinec and P. Suquet, "A numerical method for computing the overall response of nonlinear composites with complex microstructure," *Computer Methods in Applied Mechanics and Engineering,* vol. 157, pp. 69-94, 1998.
[61] T. Mura, *Micromechanics of Defects in Solids* vol. 3: Springer, 1987.
[62] J. C. Michel, H. Moulinec, and P. Suquet, "A computational method based on augmented Lagrangians and fast Fourier transforms for composites with high contrast," *Computer Modeling in Engineering & Sciences,* vol. 1, pp. 79-88, 2000.
[63] R. A. Lebensohn, "N-site modeling of a 3D viscoplastic polycrystal using Fast Fourier Transform," *Acta Materialia,* vol. 49, pp. 2723-2737, 2001.
[64] R. A. Lebensohn, "Full-Field vs. Homogenization Methods to Predict Microstructure–Property Relations for Polycrystalline Materials," in

Computational Methods for Microstructure-Property Relationships, ed: Springer US, 2011, pp. 393-441.

[65] C. Tome, G. R. Canova, U. F. Kocks, N. Christodoulou, and J. J. Jonas, "The relation between macroscopic and microscopic strain hardening in F.C.C. polycrystals," *Acta Metallurgica,* vol. 32, pp. 1637-1653, 1984/10/01 1984.

[66] R. A. Lebensohn, J. P. Escobedo, E. K. Cerreta, D. Dennis-Koller, C. A. Bronkhorst, and J. F. Bingert, "Modeling void growth in polycrystalline materials," *Acta Materialia,* vol. 61, pp. 6918-6932, 2013.

[67] N. Lahellec, J. C. Michel, H. Moulinec, and P. Suquet, "Analysis of Inhomogeneous Materials at Large Strains using Fast Fourier Transforms," in *IUTAM Symposium on Computational Mechanics of Solid Materials at Large Strains: Proceedings of the IUTAM Symposium held in Stuttgart, Germany, 20–24 August 2001*, C. Miehe, Ed., ed Dordrecht: Springer Netherlands, 2003, pp. 247-258.

[68] D. M. Saylor, B. S. El Dasher, A. D. Rollett, and G. S. Rohrer, "Distribution of grain boundaries in aluminum as a function of five macroscopic parameters," *Acta Materialia,* vol. 52, pp. 3649-3655, 2004.

[69] D. M. Saylor, B. S. El-Dasher, B. L. Adams, and G. S. Rohrer, "Measuring the five-parameter grain-boundary distribution from observations of planar sections," *Metallurgical and Materials Transactions A (Physical Metallurgy and Materials Science),* vol. 35A, pp. 1981-9, 2004.

[70] T. K. Dey and S. Goswami, "Provable surface reconstruction from noisy samples," presented at the Proceedings of the twentieth annual symposium on Computational geometry, Brooklyn, New York, USA, 2004.

[71] H. Hoppe, T. DeRose, T. Duchamp, J. McDonald, and W. Stuetzle, "Surface reconstruction from unorganized points," *Computer Graphics (ACM),* vol. 26, pp. 71-78, 1992.

[72] N. J. Mitra, A. N. Nguyen, and L. Guibas, "Estimating Surface Normals in Noisy Point Cloud Data," *International Journal of Computational Geometry & Applications,* vol. 14, pp. 261-276, 2004/10/01 2004.

[73] O. M. Ivasishin, S. V. Shevchenko, and S. L. Semiatin, "Implementation of exact grain-boundary geometry into a 3-D Monte-Carlo (Potts) model for microstructure evolution," *Acta Materialia,* vol. 57, pp. 2834-44, 2009.

[74] D. Moore and J. Warren, "Approximation of dense scattered data using algebraic surfaces," in *System Sciences, 1991. Proceedings of the Twenty-Fourth Annual Hawaii International Conference on*, 1991, pp. 681-690 vol.1.

[75] W. E. Lorensen and H. E. Cline, "Marching cubes: A high resolution 3D surface construction algorithm," *SIGGRAPH Comput. Graph.,* vol. 21, pp. 163-169, 1987.

[76] M. Groeber and M. Jackson, "DREAM.3D: A Digital Representation Environment for the Analysis of Microstructure in 3D," *Integrating Materials and Manufacturing Innovation,* vol. 3, p. 5, 2014.

[77] D. M. Saylor, A. Morawiec, and G. S. Rohrer, "Distribution of grain boundaries in magnesia as a function of five macroscopic parameters," *Acta Materialia,* vol. 51, pp. 3663-74, 2003.

[78] G. S. Rohrer, J. Li, S. Lee, A. D. Rollett, M. Groeber, and M. D. Uchic, "Deriving grain boundary character distributions and relative grain boundary energies from

three-dimensional EBSD data," *Materials Science and Technology,* vol. 26, pp. 661-669, 2010.
[79] J. Li, S. J. Dillon, and G. S. Rohrer, "Relative grain boundary area and energy distributions in nickel," *Acta Materialia,* vol. 57, pp. 4304-4311, 2009.
[80] M. Chandross and E. A. Holm, "Measuring Grain Junction Angles in Discretized Microstructures," *Metallurgical and Materials Transactions A,* vol. 41, pp. 3018-25, 2010.
[81] C. T. Chou and A. Gholinia, "New method to characterise grain boundary plane orientations based on EBSD orientation microscopy for serial sectioned surfaces," *Materials Science and Technology,* vol. 26, pp. 650-660, 2010/06/01 2010.
[82] C. M. Hefferan, S. F. Li, J. Lind, U. Lienert, A. D. Rollett, P. Wynblatt*, et al.*, "Statistics of high purity nickel microstructure from high energy X-ray diffraction microscopy," *Computers, Materials and Continua,* vol. 14, pp. 207-217, 2009.
[83] R. M. Suter, S. F. Li, C. Hefferan, and J. Lind, "Thermally induced coarsening in a nickel polycrystal observed in three dimensions," *In Preparation*.
[84] E. Kalogerakis, P. Simari, D. Nowrouzezahrai, and K. Singh, "Robust statistical estimation of curvature on discretized surfaces," *Symposium on Geometry Processing,* pp. 13-22, 2007.
[85] G. Garapić, U. H. Faul, and E. Brisson, "High-resolution imaging of the melt distribution in partially molten upper mantle rocks: evidence for wetted two-grain boundaries," *Geochemistry, Geophysics, Geosystems,* vol. 14, pp. 556-566, 2013.
[86] X. Feng, K. Xia, Y. Tong, and G.-W. Wei, "Geometric modeling of subcellular structures, organelles, and multiprotein complexes," *International Journal for Numerical Methods in Biomedical Engineering,* vol. 28, pp. 1198-1223, 2012.
[87] C.-H. Lo and H.-S. Don, "3-D moment forms: Their construction and application to object identification and positioning," *IEEE Transactions on Pattern Analysis and Machine Intelligence,* vol. 11, pp. 1053-1064, 1989.
[88] J. P. MacSleyne, J. P. Simmons, and M. De Graef, "On the use of moment invariants for the automated analysis of 3D particle shapes," *Modelling and Simulation in Materials Science and Engineering,* vol. 16, 2008.
[89] O. Monga and S. Benayoun, "Using partial derivatives of 3D images to extract typical surface features," *Computer Vision and Image Understanding,* vol. 61, pp. 171-189, 1995.
[90] T. Lindeberg, "Discrete derivative approximations with scale-space properties: a basis for low-level feature extraction," *Journal of Mathematical Imaging and Vision,* vol. 3, pp. 349-76, 1993.
[91] T. Lindeberg, "Edge Detection and Ridge Detection with Automatic Scale Selection," *International Journal of Computer Vision,* vol. 30, pp. 117-156, 1998/11/01 1998.
[92] T. Tasdizen, R. Whitaker, P. Burchard, and S. Osher, "Geometric surface processing via normal maps," *ACM Trans. Graph.,* vol. 22, pp. 1012-1033, 2003.
[93] Y. Wang, Y. Sheng, G. Lu, P. Tian, and K. Zhang, "Feature-constrained surface reconstruction approach for point cloud data acquired with 3D laser scanner," 2008, pp. 700021-700021-12.
[94] T. M. Apostol, *Calculus*, 2nd ed. vol. 2. Waltham, Mass: Xerox Publishing, 1969.

[95] P. G. Guest, *Numerical Methods of Curve Fitting*. New York, NY: Cambridge University Press, 1961.
[96] S. Leclaire, M. El-Hachem, J.-Y. Trépanier, and M. Reggio, "High Order Spatial Generalization of 2D and 3D Isotropic Discrete Gradient Operators with Fast Evaluation on GPUs," *Journal of Scientific Computing,* vol. 59, pp. 545-573, 2014/06/01 2014.
[97] E. Shima, K. Kitamura, and T. Haga, "Green–Gauss/Weighted-Least-Squares Hybrid Gradient Reconstruction for Arbitrary Polyhedra Unstructured Grids," *AIAA Journal,* vol. 51, pp. 2740-2747, 2013/11/01 2013.
[98] T. Lindeberg, "Generalized gaussian scale-space axiomatics comprising linear scale-space, affine scale-space and spatio-temporal scale-space," *Journal of Mathematical Imaging and Vision,* vol. 40, pp. 36-81, 2011.
[99] D. Saylor, J. Fridy, B. El-Dasher, K.-Y. Jung, and A. Rollett, "Statistically representative three-dimensional microstructures based on orthogonal observation sections," *Metallurgical and Materials Transactions A,* vol. 35, pp. 1969-1979, 2004/07/01 2004.
[100] A. Brahme, M. H. Alvi, D. Saylor, J. Fridy, and A. D. Rollett, "3D reconstruction of microstructure in a commercial purity aluminum," *Scripta Materialia,* vol. 55, pp. 75-80, 2006.
[101] U. Lienert, S. F. Li, C. M. Hefferan, J. Lind, R. M. Suter, J. V. Bernier*, et al.*, "High-energy diffraction microscopy at the advanced photon source," *JOM,* vol. 63, pp. 70-77, 2011/07/01 2011.
[102] S. F. Li, "Imaging of Orientation and Geometry in Microstructures: Development and Applications of High Energy X-ray Diffraction Microscopy," Doctor of Philosophy Dissertation, Physics, Carnegie Mellon University, 2011.
[103] P. Alliez, L. Rineau, S. Tayeb, J. Tournois, and M. Yvinec, "3D Mesh Generation," in *CGAL User and Reference Manual*, ed: CGAL Editorial Board, 2011.
[104] D. Boltcheva, M. Yvinec, and J. D. Boissonnat, "Mesh generation from 3D multi-material images," in *Medical Image Computing and Computer-Assisted Intervention - MICCAI 2009. 12th International Conference, 20-24 Sept. 2009*, Berlin, Germany, 2009, pp. 283-90.
[105] M. D. Lichter and S. Dubowsky, "Estimation of state, shape, and inertial parameters of space objects from sequences of range images," in *Intelligent Robots and Computer Vision XXI: Algorithms, Techniques, and Active Vision, 28 Oct. 2003*, USA, 2003, pp. 199-210.
[106] S. P. Donegan, J. C. Tucker, A. D. Rollett, K. Barmak, and M. Groeber, "Extreme value analysis of tail departure from log-normality in experimental and simulated grain size distributions," *Acta Materialia,* vol. 61, pp. 5595-5604, 2013.
[107] A. D. Rollett, R. A. Lebensohn, M. Groeber, Y. Choi, J. Li, and G. S. Rohrer, "Stress hot spots in viscoplastic deformation of polycrystals," *Modelling and Simulation in Materials Science and Engineering,* vol. 18, 2010.
[108] J. K. Mackenzie, "Second Paper on Statistics Associated with the Random Disorientation of Cubes," *Biometrika,* vol. 45, pp. 229-240, June 1, 1958 1958.
[109] J. Bingert, R. Suter, J. Lind, S. Li, R. Pokharel, and C. Trujillo, "High-Energy Diffraction Microscopy Characterization of Spall Damage," in *Dynamic Behavior*

of Materials, Volume 1, B. Song, D. Casem, and J. Kimberley, Eds., ed: Springer International Publishing, 2014, pp. 397-403.

[110] C. A. Bronkhorst, G. T. Gray, F. L. Addessio, V. Livescu, N. K. Bourne, S. A. MacDonald*, et al.*, "Response and Representation of Ductile Damage under Varying Shock Loading Conditions in Tantalum," *Journal of Applied Physics,* vol. 119, 2016.

[111] M. Ortiz and A. Molinari, "Effect of Strain Hardening and Rate Sensitivity on the Dynamic Growth of a Void in a Plastic Material," *Journal of Applied Mechanics,* vol. 59, pp. 48-53, 1992.

[112] W. Tong and G. Ravichandran, "Inertial Effects on Void Growth in Porous Viscoplastic Materials," *Journal of Applied Mechanics,* vol. 62, pp. 633-639, 1995.

[113] A. L. Gibbs and F. E. Su, "On Choosing and Bounding Probability Metrics," *International Statistical Review,* vol. 70, pp. 419-435, 2002.

[114] F. A. McClintock, "Ductile fracture instability in shear," in *ASME Meeting, Nov 30-Dec 5 1958*, New York, NY, United States, 1958, p. 7.

[115] J. R. Rice and D. M. Tracey, "On the ductile enlargement of voids in triaxial stress fields⋆," *Journal of the Mechanics and Physics of Solids,* vol. 17, pp. 201-217, 1969/06/01 1969.

[116] E. Maire, O. Bouaziz, M. Di Michiel, and C. Verdu, "Initiation and growth of damage in a dual-phase steel observed by X-ray microtomography," *Acta Materialia,* vol. 56, pp. 4954-4964, 10// 2008.

[117] F. Roters, P. Eisenlohr, T. R. Bieler, and D. Raabe, *Crystal Plasticity Finite Element Methods*: Wiley-VCH Verlag GmbH & Co. KGaA, 2010.

[118] J. C. Schuren, P. A. Shade, J. V. Bernier, S. F. Li, B. Blank, J. Lind*, et al.*, "New opportunities for quantitative tracking of polycrystal responses in three dimensions," *Current Opinion in Solid State and Materials Science,* vol. 19, pp. 235-244, 8// 2015.